Construction and First Tests of the ZEUS Prototype Calorimeter

Peter Neelin

Department of Physics

McGill University, Montréal, Québec

September, 1988

A thesis submitted to the Faculty of Graduate Studies and Research in partial fulfillment of the requirements for the degree of Master of Science in Physics.

Construction and First Tests of the ZEUS Prototype Calorimeter

Abstract

The design and construction of the prototype for the ZEUS forward calorimeter are described, along with the results of first tests carried out at CERN in November and December of 1987. The choice of a sampling structure with depleted uranium as absorber and plastic scintillator as read-out has led to a hadron energy resolution of $\sigma_E/E = 37\%/\sqrt{E}$ and an electromagnetic energy resolution of $\sigma_E/E = 20\%/\sqrt{E}$ in the energy range 1 to 10 GeV. The electron to hadron signal ratio (e/h) has been found to be very close to the ideal of 1.0 with $e/h = 1.0024$ at 10 GeV.

Résumé

La conception et construction du prototype pour le calorimètre avant du détecteur ZEUS sont décrites, avec les résultats de premiers tests éffectués au CERN en novembre et décembre, 1987. Le choix d'une structure d'échantillonnage fait d'uranium épuisé comme absorbeur et de scintillateur plastique comme matériel actif donne une résolution d'énergie hadronique de $\sigma_E/E = 37\%/\sqrt{E}$ et une résolution d'énergie électromagnétique de $\sigma_E/E = 20\%/\sqrt{E}$ pour des énergies entre 1 et 10 GeV. Le rapport de signal électronique à signal hadronique (e/h) a été trouvé très près de l'idéal de 1.0 avec $e/h = 1.0024$ à 10 GeV.

Acknowledgements

As for most endeavours in our modern society, this thesis is in reality the product of the efforts of many people. The large experimental groups of high-energy physics make this even more true, and I would like to thank for their help and patience both the members of the Canadian team with whom I spent many hours in the basement of the York University physics building, and our German, Dutch, Spanish and Japanese collaborators who shared with me shifts in the dim dustiness of the CERN PS experimental hall. I would particularly like to thank my supervisor David Hanna for his advice, patience and flexibility throughout our year and a half of collaboration.

A special thanks to the many members of the McGill physics community: to Robert Nowac for drawing figures for my thesis, to Paul Mercure for constant help with computer software and hardware (and for much patience), to Alain Legault for help installing the Apollo program at McGill, to fellow graduate students for many hours of interesting discussion and problem-sharing, and to the McGill professors for their willingness to listen and advise.

Both my work and the work of the canadian group with the ZEUS collaboration has been supported by NSERC (Natural Sciences and Engineering Research Council of Canada), and I would like to thank that organisation for its important role in promoting science in Canada.

I would especially like to thank my wife Kim for endless support and encouragement, despite months of absence, and my parents and family for giving me a desire to learn.

Table of Contents

Preface

The design, construction and testing of this prototype calorimeter has been a collaborative effort of many institutions from many countries around the world. My direct involvement began only in the construction at York University in August, September and October of 1987. The work there was carried out primarily by people from four canadian universities (York, Toronto, McGill and Manitoba), but also with help from Dutch and German members of the collaboration. The initial testing of the calorimeter took place in November and December, 1987, at CERN, Geneva. I assisted in that work throughout the month of November. The data analysis was done independently, using the basic software infrastructure available for the ZEUS experiment, with confirmation of my results coming from work done by other members of the collaboration. I have also done development work outside the scope of this thesis in the areas of calibration and of component testing.

The entire process of prototype development has contributed to original knowledge through dealing with structural design problems, developing precision construction techniques and, most importantly, providing a test of theoretical predictions for high-resolution hadron calorimetry. Although my thesis stops at this point, the work of the ZEUS calorimeter development and construction continues, with its eventual culmination in the exciting physics to be seen at HERA.

Chapter 1 – Introduction

1.1 The Experiment

The Deutsches Elektronen-Synchrotron (DESY) in Hamburg, Germany, is constructing an electron-proton collider called HERA to study the deep inelastic scattering of electrons off protons at energies much higher than can be achieved by traditional, fixed-target accelerators. The 30 GeV electron – 820 GeV proton interactions will allow investigation of proton, electron and quark structure as well as of the properties of electroweak currents and strong interactions. Additionally, they will provide a chance to search for new particles that might exist with masses in the energy range of the collider.

The ZEUS detector will allow researchers to glimpse the outcome of these interactions and infer a great deal about physics at this scale. The detector includes drift chambers for vertex and track detection, calorimeters for particle energy measurement, muon detectors plus a host of other devices for particle identification and measurement. As we shall see, the charged and neutral current electroweak interactions that will occur at HERA will require a high resolution hadron calorimeter which has only become possible in the past few years with depleted uranium(DU)/scintillator calorimeters. For some time now, the focus of the efforts of a large number of institutions across the world has been the construction of such a device for the ZEUS detector. This thesis describes the culmination of those efforts in a final prototype for the ZEUS calorimeter.

1.2 Why ep Physics?

1.2.1 *Electron-Proton Scattering*

In the late 1960's and early 1970's, electron-proton scattering (or, more generally, lepton-nucleon scattering) confirmed the compositeness of hadrons — the so-called parton model of the proton. At high enough energies, measurements of cross-section were not consistent with scattering from a point-proton, but rather with a sea of constituent point-like particles, partons, that were eventually identified with Murray Gell-Mann's "quarks", confirming their reality. Because these experiments used lepton beams incident on fixed nucleon targets, the centre-of-mass energies never exceeded about $\sqrt{s} = 2\sqrt{E_\mu m_p} \simeq 23$ GeV, and the square of the momentum transferred between lepton and proton, Q^2, ranged up to only $(20\ \mathrm{GeV})^2$.

With its (10–30) GeV electrons colliding with (300–820) GeV protons, HERA will yield centre-of-mass energies in the range $\sqrt{s} = 2\sqrt{E_e E_p} \simeq$(110–314) GeV, and Q^2 up to 10^5 GeV^2. Deep inelastic scattering at such high Q^2 will be essentially an electron-quark interaction. The lowest order diagrams for *ep* scattering are shown in figure 1.1. In general, one has the lepton and the quark jet emerging or opposite sides of the beam axis, with equal and opposite transverse momentum, and the proton jet continuing down the beam pipe. For the neutral current interaction (γ or Z^0 exchange), the emerging lepton is an electron, however for the charged current interaction ($W^\pm$ exchange), the emerging lepton is an undetectable neutrino, making jet energy and direction measurement very important.

Before looking at scattering cross-sections, it is useful to introduce a number of variables that frequently crop up in the discussion of electron-proton scattering:

Note: The material for this section has been taken from references [1] – [8].

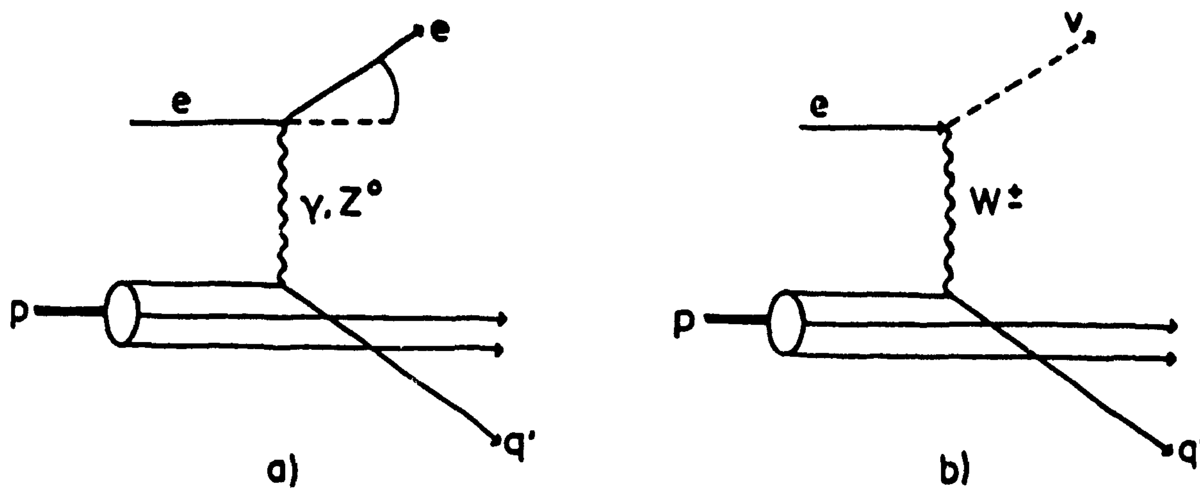

Figure 1.1 : Lowest order diagrams for (a) neutral current ep scattering, and (b) charged current ep scattering [7].

(Please note the following notation

E = energy	m = mass
p = momentum 4-vector	$\vec{p}$ = momentum 3-vector
subscript e = electron	subscript p = proton
superscript prime = outgoing particle)	

Total centre-of-mass energy squared (neglecting electron and proton masses).

$$s = (p_p + p_e)^2 = E_p^2 + E_e^2 + 2E_pE_e - |\vec{p}_p|^2 - |\vec{p}_e|^2 + 2|\vec{p}_p||\vec{p}_e|$$
$$= m_e^2 + m_p^2 + 2(E_pE_e + |\vec{p}_p||\vec{p}_e|)$$
$$\simeq 4E_eE_p$$

Square of 4-momentum transfer

$$q^2 = (p_e - p_e')^2 = -Q^2$$

Square of the total mass of the final hadronic system

$$W^2 = (q + p_p)^2$$

Energy transferred by the current in the proton rest system

$$\nu = \frac{q \cdot p_p}{m_p}$$

$$(\text{with } \nu_{max} \simeq \frac{2E_e E_p}{m_p}, \text{ neglecting } m_e,\, m_p)$$

Bjorken scaling variable (this is also a measure of the fraction of the proton's momentum carried by a quark)

$$x = \frac{Q^2}{2(q \cdot p_p)} = \frac{Q^2}{2m_p \nu}$$

and

$$y = \frac{(q \cdot p_p)}{(q \cdot p_e)} = \frac{\nu}{\nu_{max}}$$

Note also that

$$Q^2 \simeq sxy$$

Experimentally, Q^2, x and y can be determined either from energy and angle of the outgoing electron or from the energy and angle of the jet (necessary for charged current scattering).

We can now start looking at scattering cross-sections. To get an initial understanding of the usefulness of extending ep scattering studies to the very high Q^2 range, it is helpful to compare rates for γ exchange (electromagnetic) scattering and W exchange (weak) scattering. The cross-sections have approximately the following behaviour:

$$\frac{d^2\sigma(\gamma p)}{dxdy} \sim \alpha^2 s \left(\frac{1}{Q^2}\right)^2 F(x,y)$$
$$\frac{d^2\sigma(Wp)}{dxdy} \sim \alpha^2 s \left(\frac{1}{Q^2 + M_W^2}\right)^2 F(x,y)$$

where M_W = mass of the W particle = 82 GeV. For $Q^2 \rightarrow 0$, the rate for γp is roughly 10^8 times that of Wp, but for $Q^2 > 10^4$ GeV^2, the γp and Wp rates are of the same order, allowing effective studies of electroweak processes.

The differential cross-sections can be written in terms of the quark distribution functions and a variety of constants. For example, the neutral current cross-section is

$$\frac{d^2\sigma(\gamma+Z^0)}{dxdy} = \frac{4\pi\alpha^2}{sx^2y^2}\left[(1-y)F_2(x,Q^2) + y^2xF_1(x,Q^2)\right]$$

F_1 and F_2 are the so-called structure functions and can be expressed in terms of the quark distribution functions, leading to

$$\frac{d^2\sigma(\gamma+Z^0)}{dxdy} = \frac{\pi\alpha^2}{sx^2y^2}\sum_q \left\{xq(x)\left[A_q + (1-y)^2B_q\right] + x\bar{q}(x)\left[B_q + (1-y)^2A_q\right]\right\}$$

where $q(x)$ and $\bar{q}(x)$ are the quark and anti-quark distribution functions for different flavours, and A_q and B_q are constants determined by quark and lepton charge, lepton weak isospin and the weak mixing angle, θ_W. The final result takes into account the left or right-handedness of the electron in the scattering (see reference [7]).

For charged currents, the expression for the cross-section is similar,

$$\frac{d^2\sigma(e_L^- p \to \nu X)}{dxdy} = \frac{G_F^2 s}{\pi}\frac{1}{(1+Q^2/M_W^2)^2}$$
$$\left[(1-y)F_2(x,Q^2) + y^2xF_1(x,Q^2) + (y - y^2/2)xF_3(x,Q^2)\right]$$

with

$$F_2(x) = 2xF_1(x) = x\left[q(x) + \bar{q}(x)\right]$$
$$xF_3(x) = x\left[q(x) - \bar{q}(x)\right]$$

and

$$q(x) = u(x) + c(x) + \cdots$$
$$\bar{q}(x) = \bar{d}(x) + \bar{s}(x) + \cdots$$

Note that the cross-section for $e_R^- + p \to \nu + X$ is zero since the neutrino is left-handed (and similarly for $e_L^+ + p \to \bar{\nu} + X$, since the anti-neutrino is right-handed).

1.2.2 *The Interesting Physics*

Precision measurements of the structure functions at high Q^2 will provide a stringent test of both QCD (quantum chromodynamics) and electroweak theories, as well as allowing the probing of quarks and electrons for substructure down to a scale of 3×10^{-20} m.

QCD predicts that the structure functions will fall logarithmically for increasing Q^2 due to a scale breaking (an inherent energy scale in the function's behaviour) arising from gluon radiation by the scattered quark. That is

$$F(x) \rightarrow \frac{F(x)}{1 + c\ln(Q^2/\Lambda_{QCD}^2)}$$

where Λ_{QCD} is the QCD scale parameter. Until now, structure function data has been in the range 0–300 GeV^2. HERA will increase the upper limit to 40 000 GeV^2. An additional benefit is that mass corrections and higher twist contributions that provide the main uncertainty at low energies will disappear at the high Q^2 of HERA.

HERA will allow searches for new weak currents. We have seen that for the standard W (or Z) the amplitude goes as $1/(Q^2 + M_W^2)$. If there exist more massive W's or Z's, then a similar term will be added to the amplitude, with M_W replaced by the mass of the new particle. For roughly two years of data taking with HERA, one should be able to see the effects of such currents up to masses of $\approx$ 800 GeV.

It has been noted that only left-handed neutrinos and the corresponding left-handed current have been observed — no right-handed neutrinos. It is speculated that a right-handed, massive neutrino exists (coupling to a right-handed W). HERA has the facility for polarizing the electron beam, permitting a search for such a right-handed neutrino, down to a right-handed to left-handed cross-section ratio of $\sigma_R/\sigma_L \approx 0.03$.

If electrons and quarks are composites of even more elementary particles, then it is quite possible that at HERA the residual interactions of these particles will cause the cross-sections to deviate at high Q^2 from the standard model predictions. Asymmetries with respect to left and right-handedness allow one to use the polarized electron beam of HERA for an even greater sensitivity, up to an energy scale of $\Lambda \approx 7$ TeV (3×10^{-20} m).

As well as the above-mentioned studies of QCD and electroweak theories HERA will provide the means for producing both known particles (for further studies) and, if they exist, new particles.

Within the realm of standard physics is the photoproduction of heavy quarks (possibly even the top quark, if it is in the appropriate mass range). These events will be easily distinguished from others because the quarks will be emitted in the direction of the incoming proton and will decay into many particles isotropically distributed in the plane perpendicular to the beams.

Leptoquarks are particles that could mediate lepton-quark transitions and arise from superstring, grand-unified, technicolour and quark-lepton substructure theories. Electron-proton machines are ideally suited for searching for such particles and according to theoretical predictions HERA should be able to produce significant numbers of these particles.

Finally, HERA should be capable of producing new particles (or rather, sparticles) predicted by supersymmetric theories — in particular, sleptons and squarks should be produced in detectable numbers if $m_{\tilde{l}} + m_{\tilde{q}} \leq 150$ GeV.

Apart from these, other particles may be produced at HERA, though at a much lower rate, including vector bosons, Higgs particles and excited quarks and leptons.

1.2.3 *Detector Requirements*

To be able to make the measurements described, one must have an adequate detector. The physics and topology of the interactions lead to fairly stringent requirements for the ZEUS detector.

The imbalance in electron and proton energies leads to many of the outgoing particles having a large forward momentum, much like a fixed-target experiment, requiring very good forward detectors for high energy particles. At the same time, the detector must be hermetic (not allow particles to escape undetected through spaces) and completely surround the interaction — for example, an electron escaping from a neutral current interaction would lead to identifying the event as having an (undetectable) neutrino and hence being a charged current interaction.

The detectors must provide good electron and hadron energy measurement, good angular resolution and good lepton identification. These requirements place an emphasis on having good tracking detectors and especially good calorimeters over the full solid angle.

As outlined in the ZEUS letter of intent [8], the goals for the energy resolutions are defined by the current limits of technology. For the electromagnetic calorimeter a resolution of $\sigma(E)/E = 0.15/\sqrt{E}$ (E in GeV) will satisfy the physics requirements. The resolution sought for the hadron calorimeter is $\sigma(E)/E = 0.35/\sqrt{E}$. Until recently, the best resolution for a hadron calorimeter has been $0.6/\sqrt{E}$, but with the advent of depleted uranium/scintillator calorimeters, a resolution of $0.35/\sqrt{E}$ has been achieved. A study of the difference in quality of physics has demonstrated that a significant gain is made by having the better resolution. This, then, defines the principal goal of the prototype calorimeter work.

1.3 The ZEUS Detector

Before embarking on a detailed description of the ZEUS calorimeter, it is helpful to have a brief overview of the entire detector to understand how the calorimeter fits into the larger scheme of things. (For a more complete description of the detector, see references [9] and [10]).

The ZEUS detector is basically cylindrical in shape, with the layout as depicted in figures 1.2 and 1.3. Working from the electron-proton interaction point outwards, the essential components are the vertex detector (VXD), the central track detector (CTD), the transition radiation detector (TRD), the forward and rear track detectors (FTD, RTD), the electromagnetic and hadron calorimeters (EMC, HAC) (surrounding the magnet coil), a backing calorimeter (BAC), barrel and rear muon detectors (MU), and a forward muon spectrometer (FMU).

The central components (vertex and track detectors) are contained within a superconducting magnet that provides a magnetic field of 1.8 Tesla, allowing momentum measurement through the curvature of the tracks of charged particles. The central track detector is a drift chamber consisting of nine layers (called "super-layers") that each have eight sense wires. Four of those super-layers have so-called stereo wires: wires not quite parallel to the cylindrical axis of the detector, allowing position measurements in the axial direction that are of the same quality as measurements in the azimuthal direction (for wires parallel to the axis, the position component in this direction is usually found by comparing the charge collected at each end of the wire — this gives a much poorer measurement than in the azimuthal direction). The expected position resolution for this detector is 100 μm; the expected momentum resolution is $\sigma(p)/p = 0.002 \cdot p \oplus 0.003$ (p in GeV/c) where $\oplus$ means that the errors are added in quadrature. The forward and rear track detectors help in small-angle

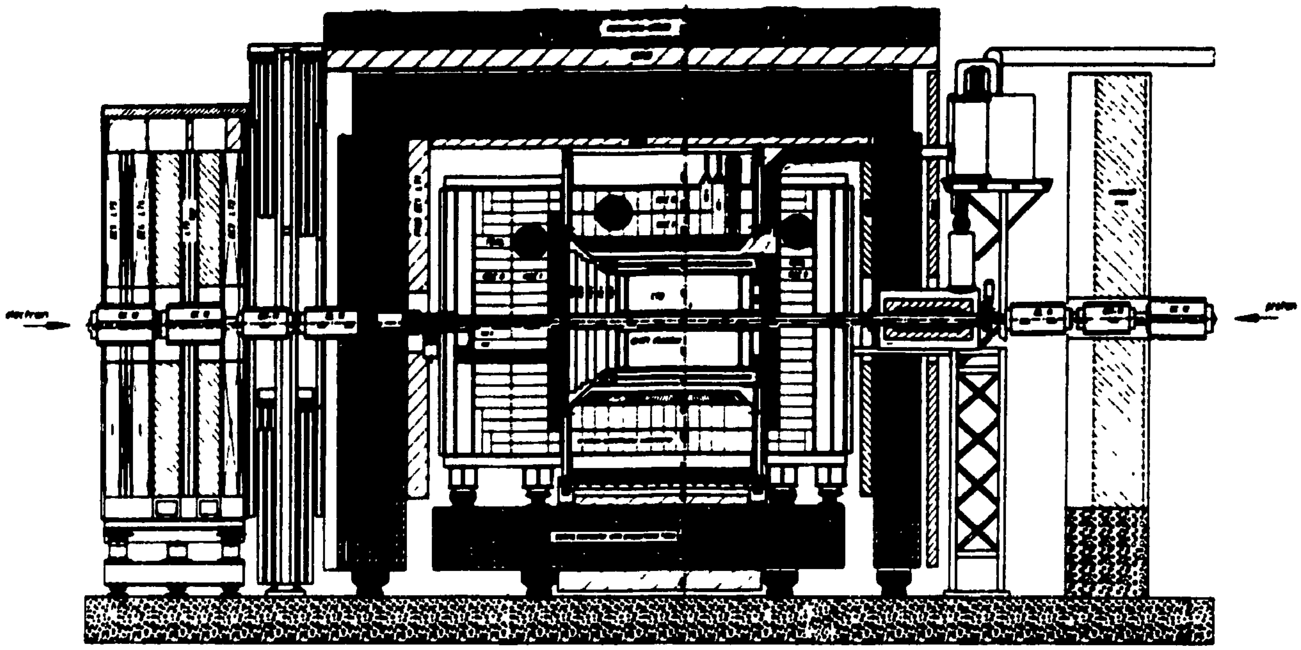

Figure 1.2 : Section of the ZEUS detector along the beam [10]. Electrons travel from left to right, and protons travel from right to left, so the forward calorimeter is to the left of the interaction point.

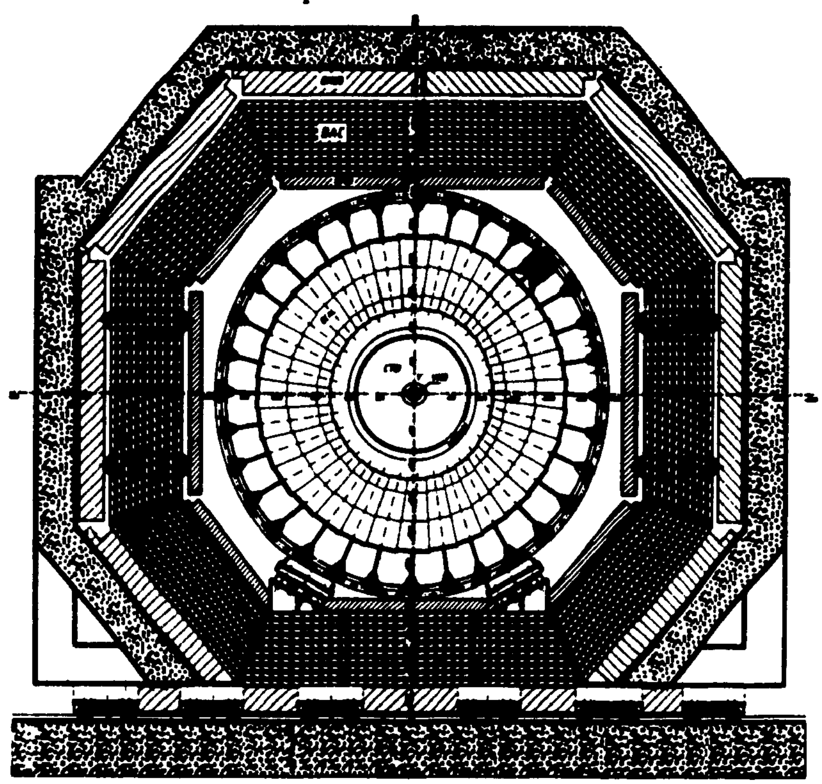

Figure 1.3 : Section of the ZEUS detector perpendicular to the beam [10].

particle tracking, giving a momentum resolution of $\sigma(p)/p = 0.01 \cdot p$ at a forward angle of 140 mrad.

The important process of electron identification can be achieved to a high accuracy using information from a variety of detectors. The principal data used is the dE/dx (energy loss per unit length) data from the tracking detectors and the data from the calorimeters (energy from electrons is deposited in a much smaller depth of calorimeter than energy from hadrons). A silicon pad detector will be inserted in the calorimeters at a few radiation lengths to measure shower size, giving an additional level of electron-hadron separation. For particles in the forward direction, the transition radiation detector allows an even better hadron rejection.

The calorimeter (which will be described in much greater detail in chapter 2), is of the sampling variety, with a stack of alternating layers of depleted uranium and plastic scintillator causing incident particles to produce showers of lower energy particles that emit light in the scintillator in amounts proportional to the energy of the original particle. This light is carried out of the stack by wavelength-shifter (WLS) bars and light-guides to be measured by photomultiplier tubes. The calorimeter is read out at three depths: the electromagnetic section (EMC) closest to the interaction region, and two hadronic sections (HAC1 and HAC2) behind the EMC. There are three parts to the calorimeter: the forward calorimeter (which is the deepest, at 7 absorption lengths), the barrel calorimeter (5 absorption lengths) and the rear calorimeter (4 absorption lengths). These three parts cover 99.8% of the solid angle in the forward hemisphere and 99.5% in the rear hemisphere, allowing very few particles to escape undetected (principally only those that travel down the beam pipe). To measure the energy of late showering particles there is a backing calorimeter, using the iron plates of the magnet yoke as absorber, and aluminum tubes operating in proportional mode as read-out. The expected resolution of this calorimeter is $\sigma(E)/E = 1.0/\sqrt(E)$ (E in GeV).

Forward-going muons are detected in a spectrometer that uses drift-chambers, limited streamer tube chambers and scintillator counters. Over the rest of the solid angle, limited streamer tube chambers are used.

In the proton beam direction, a leading proton spectrometer uses high resolution chambers near the beam to measure the momentum of very forward-produced protons.

In the electron beam direction, electron and photon detectors 30 to 100 m downstream from the interaction measure the luminosity and detect small Q^2 processes.

The detector is built in a modular fashion, with the structural components able to be retracted from the beam to allow easy access to the individual modules, facilitating maintenance.

1.4 The Current State of Calorimetry

In high energy physics, a calorimeter measures a particle's energy by totally absorbing it. The calorimeter is just a large block of material that induces an incident particle to "shower", that is, produce particles of successively lower energies that are eventually stopped in the block. In this way, all of the energy of the original particle is deposited in the detector and, if we have a useful calorimeter, some fraction of that energy can be detected either in the form of light (Cerenkov or scintillation light) or of charge (from ionization). For the calorimeter to be truly useful, the amount of detected energy should be proportional to the energy of the incident particle.

Calorimeters have only recently become an essential component of high energy experiments. Various forms of tracking detectors, including cloud chambers, bubble chambers, time-projection chambers and drift chambers, have traditionally been used in conjunction with a large magnet to measure particle momenta through the curvature of trajectories. However, there is a component of the relative error (σ_p/p) in this measurement that increases linearly with momentum — at high energies, the error can become very large. The shower or "cascade" in a calorimeter involves statistical fluctuations of the number, N, of secondary particles produced. Since N is proportional to the energy, E, of the incident particle, the relative error follows the usual rule: $\sigma/E \propto 1/\sqrt{N} \propto E^{-1/2}$, so that energy measurement improves with increasing energy.

There are a number of other advantages in the favour of calorimeters: Tracking devices are, in general, only sensitive to charged particles; calorimeters can measure the energy of charged and neutral particles alike. This is becoming increasingly important as the properties of "jets" replace those of individual particles as the essential measurements. (A jet is a narrow cone of particles produced from a quark or gluon due to the confinement of these strongly interacting particles — hence a "quark jet" or a "gluon jet"). If one were to ignore the energies of all neutral particles in the jet, the total energy measurement could seriously deviate from the true value.

Because showers develop exponentially, their depth of penetration increases only logarithmically. This means that as we develop increasingly powerful accelerators to probe matter at smaller and smaller scales, we need not build increasingly massive calorimeters to cope with the particle energies. To maintain a given momentum resolution, a magnetic spectrometer must scale as $\sqrt{p}$, all other things being equal.

Calorimeters respond in different ways to electrons, muons and hadrons, allowing an important degree of particle identification. Using a calorimeter with a magnetic spectrometer-type device, which gives particle charge, and with drift chambers or any other device that gives ionization loss per unit length, one can achieve a very good ability to distinguish between particles.

Finally, calorimeters respond, and recover, quickly, so that they can cope with very high particle rates. With higher energy colliders (particularly electron-proton and proton-proton) producing a very large fraction of uninteresting data, it is important for devices to have short "dead times", and to provide quick information on the quality of each event, allowing on-line discrimination between interactions (computers can only handle a certain data rate, so one saves only interesting events) — calorimeters can provide this information.

The showers produced by electrons and photons (electromagnetic showers) differ greatly from those produced by hadrons, both in physical interactions with the material, and in their overall behaviour, so they will be described in separate subsections. The development of electromagnetic showers (described in the first subsection) has been well understood for a number of years, however, only recently has a reasonable picture of hadron showers and the processes involved (described in the second subsection) been developed. The material on electromagnetic calorimetry is based on references [5] and [11] - [18]. The material on hadron calorimetry is taken from references [7] and [19] - [28].

1.4.1 *Electromagnetic Calorimetry*

Figures 1.4 and 1.5 show the contributions to the energy loss of electrons/positrons (figure 1.4) and photons (figure 1.5) for different interactions with matter. For electrons, the high energy range is dominated by bremsstrahlung: radiation by the electron of photons due to interactions with the nuclei in matter. At lower energies (less than $\sim$ 10 MeV for lead), collision-type processes dominate: Møller (electron-electron) scattering, Bhabha (electron-positron) scattering, ionization and positron

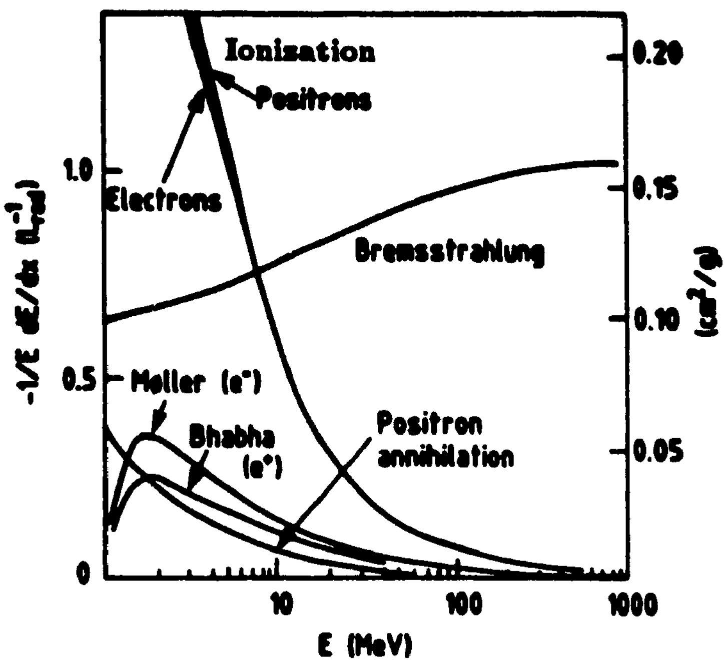

Figure 1.4 : Fractional energy loss per radiation length (left ordinate) and per g/cm^2 (right ordinate) in lead as a function of electron or positron energy. (Review of Particle Properties, April 1982 edition).

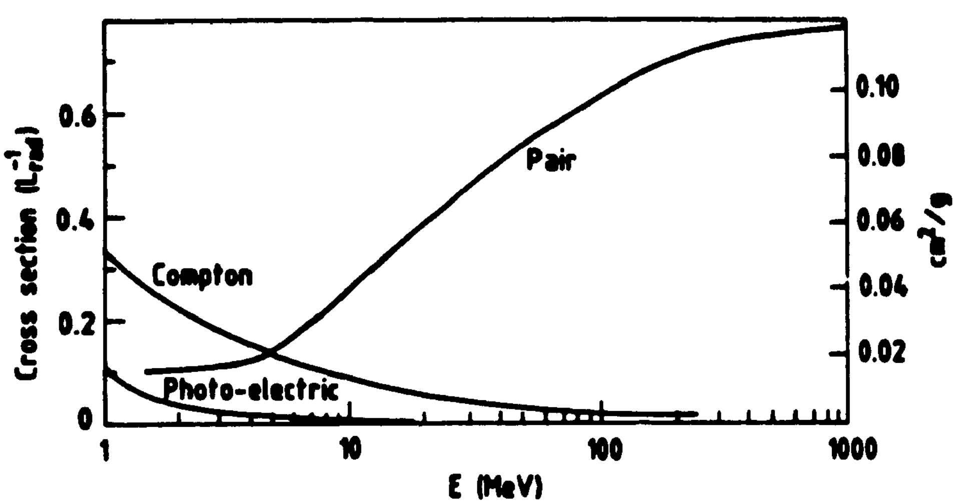

Figure 1.5 : Photon cross-section in lead as a function of photon energy. (Review of Particle Properties, April 1980 edition).

annihilation. For photons, the total cross-section at high energy is dominated by pair creation: the creation of an electron-positron pair from the photon due to the presence of a nucleus (this process has a diagram equivalent to that of bremsstrahlung and hence the cross-sections are very similar). Again, at energies less than ~ 10 MeV in lead, the Compton effect (electron-photon scattering) and, to a much lesser extent, the photo-electric effect (ionization of an atom by absorption of a photon) dominate the cross-section.

In the high-energy limit, the energy loss due to bremsstrahlung is given by [13]

$$\frac{dE_{brem}}{dx} \underset{E\to\infty}{\longrightarrow} \left[\frac{16}{3} N \frac{Z^2 e^2}{\hbar c}\left(\frac{z^2 e^2}{Mc^2}\right)^2 \ln\left(\frac{233M}{Z^{1/3}m}\right)\right] \gamma M c^2$$

where N is the number of fixed charges Ze (atomic nuclei) per unit volume, ze is the charge of the incident particle of mass M and m is the mass of the electron. We can rewrite this as

$$\frac{dE}{dx} = -\frac{E}{X_0}$$

or

$$E(x) = E_0 e^{-x/X_0}$$

where the radiation length

$$X_0 = \left[\frac{16}{3} N \frac{Z^2 e^2}{\hbar c}\left(\frac{z^2 e^2}{Mc^2}\right)^2 \ln\left(\frac{233M}{Z^{1/3}m}\right)\right]^{-1}$$

defines the unit of length, not only for the energy loss due to bremsstrahlung, but also for pair-production, and hence for the development of the electromagnetic shower.

It is worth noting at this point that X_0 goes as $\ln(M)/M^2$, which is essentially a M^{-2} dependence. This means that for muons, bremsstrahlung (and hence showering) does not occur in standard calorimeters — they would have to be (in the naïve picture) $\left(\frac{m_\mu}{m_e}\right)^2 \simeq (200)^2 = 40\,000$ times as thick for one to see the same showering as one sees for electrons (ignoring other processes such as ionization, which of course one cannot do in reality).

In the description of energy loss from low-energy electrons/positrons (through collisions with the medium), the concept of a critical energy is important. This critical energy ϵ_c is defined as the energy at which energy loss by radiation is equal to energy loss by ionization [12], that is

$$-\frac{dE}{dx}\bigg|_{rad}(\epsilon_c) = -\frac{dE}{dx}\bigg|_{ion}(\epsilon_c)$$

Alternatively, the critical energy is defined as the energy at which energy loss per radiation length is equal to the energy [18], ie.

$$-\frac{dE}{dx}(\epsilon_c) = \frac{\epsilon_c}{X_0}$$

Another process between electrons and matter that has not yet been mentioned is multiple coulomb scattering: the scattering of electrons from nuclei through simple coulomb fields. Coulomb scattering does not affect the energy loss from electrons, but alters their direction, and so has an effect on the transverse development of showers. But more of this later.

We now turn our attention to the shower produced from the incident particle. As has already been mentioned, the showering effect arises from the interaction of the incident (or primary) particle with the matter of the calorimeter, producing a number of secondary particles which also interact with the material to produce even more new particles. The process continues until the particles' energies are too low to produce more particles, and the shower stops. The total energy lost is the sum of the energies lost by all of the particles in the shower, so it becomes useful to think of a total track length: the sum of the distances travelled by all of the electrons and positrons. If we ignore lower energy effects, then the signal from muons traversing the detector should equal the signal produced in an electron shower, provided the total track lengths are the same. This allows one to use muons to calibrate and gain a better understanding of one's detector.

A variety of models have been developed to understand the behaviour of electromagnetic showers. The simplest of these, though unrealistic, helps one to grasp some basic ideas. In this model, one assumes that after travelling one radiation length, an electron of energy E_0 radiates a photon of energy $E_0/2$ and continues on itself with energy $E_0/2$. Similarly, a photon of energy E_0 pair-produces an electron and a positron, each of energy $E_0/2$, after travelling a distance of one radiation length. Thus we can ignore particle type distinctions and the probabilistic nature of the interactions. If we have an incident particle of energy E_0, then after one radiation length, we have two particles of energy $E_0/2$; after two radiation lengths, we have four particles of energy $E_0/4$, and so on. After t radiation lengths, there will be $N = 2^t$ particles, each with the same energy E_0/N. This process will stop when the particle energy reaches the critical energy ϵ_c and ionization loss dominates. The shower thus reaches a maximum at depth t_{max} and then stops, with the energy per particle at this point being

$$\frac{E_0}{2^{t_{max}}} = \epsilon_c$$

so that

$$t_{max} = \log_2\left(\frac{E_0}{\epsilon_c}\right) = \frac{\ln(E_0/\epsilon_c)}{\ln 2}$$

The number of particles at this point is

$$N_{max} = 2^{t_{max}} = \exp(t_{max} \ln 2) = \frac{E_0}{\epsilon_c}$$

with electrons, positrons and photons in nearly equal numbers. The total track length is approximately

$$S = \frac{2}{3}X_0 \sum_{\nu=1}^{t_{max}} 2^\nu + s_0 \frac{2}{3} N_{max} = \left(\frac{4}{3}X_0 + \frac{2}{3}s_0\right)\frac{E_0}{\epsilon_c}$$

where s_0 is the path length of particles below the critical energy, and the factor of 2/3 arises from not counting photons.

This model does not give the correct longitudinal shape of shower, but it does give some important general features which include a maximum that increases logarithmically with E_0, a number of shower particles at maximum that is proportional to E_0, and a total track length that is proportional to E_0.

Rossi [18] has worked out analytic descriptions for shower development using two sets of approximations. "Approximation A ... neglects collision processes and Compton effect and uses the asymptotic formulæ to describe radiation processes and pair production". Approximation B is essentially the same as approximation A except that "collision loss is described as a constant energy dissipation". These approximations yield results qualitatively similar to those already derived, but with corrections to the general behaviour. Note that both the first model and Rossi's models describe longitudinal development of the shower, but say nothing about its transverse characteristics (transverse being the direction perpendicular to the direction of motion of the incident particle).

The best models (but not always the most useful) for shower development come from Monte Carlo simulations: computer programs that attempt to accurately simulate all of the important processes in a probabilistic way. Longo and Sestili [16] simulated electromagnetic showering from photons in lead glass and found a conve-

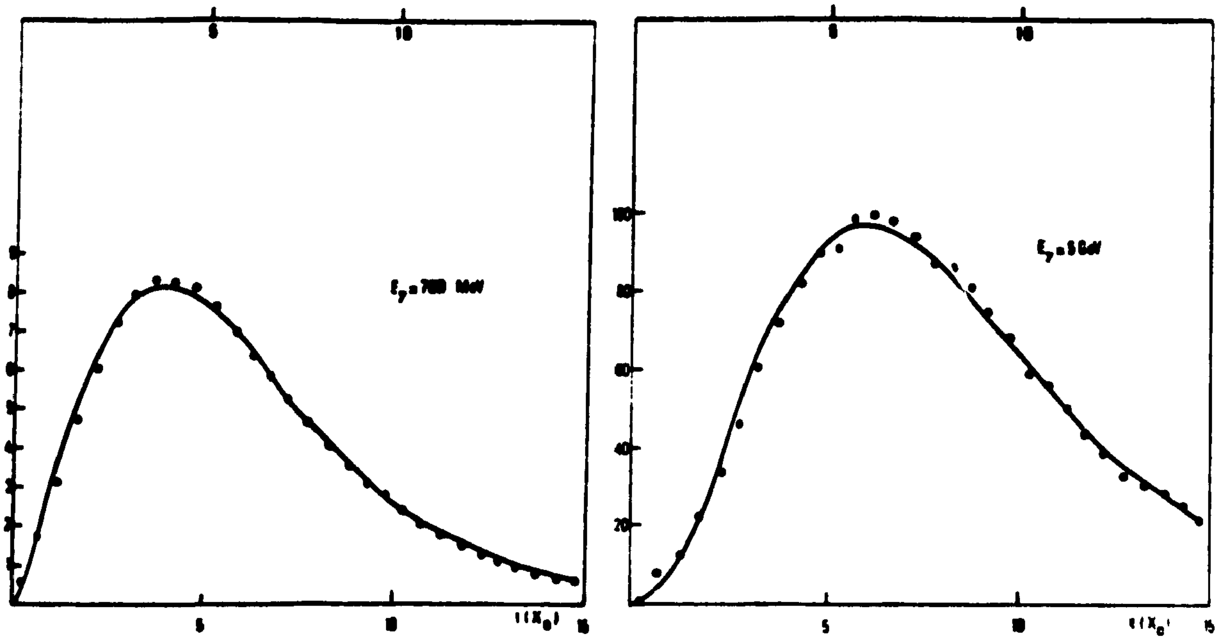

(a) (b)

Figure 1.6 : Longitudinal development of photon initiated showers, with average number of charged particles (above 0.5 MeV) plotted as a function of depth t. Plot (a) is for incident energy 0.7 GeV, plot (b) for energy 5 GeV. (From Longo and Sestili [16]).

nient analytic form:

$$\frac{dE}{dt} = E_0 \frac{\beta^{\alpha+1}}{\Gamma(\alpha+1)} t^{\alpha} e^{-\beta t}$$

where $t = x/X_0$, x = depth in calorimeter, and α and β are parameters with typical values

$$\alpha = 1.2840 + 0.7136 \ln E$$

$$\beta = 0.5607 + 0.0093 \ln E$$

(E measured in GeV). The shower maximum occurs at $t_{max} = \alpha/\beta$ and the centre of gravity of the longitudinal distribution occurs at $\bar{t}(E) = (\alpha+1)/\beta$. The longitudinal spread (the standard deviation) of the shower is given by $\tau(E) = \sqrt{\alpha+1}/\beta$. Figure 1.6 illustrates the longitudinal shower development for two energies, with both Monte Carlo results and the fitted function displayed for comparison.

The transverse spread of the shower arises primarily from the angle of bremsstrahlung emission and from multiple coulomb scattering. At lower energies, the latter process dominates. The general rule used is that for total energy measurement, the shower is contained within a cylinder of radius

$$R \approx 2\rho_M$$

where $\rho_M = X_0(21 \text{ MeV})/\epsilon_c$.

The resolution of electromagnetic calorimeters is limited by a number of factors. (Much of this also applies in general terms to hadron calorimeters). First of all, any practical device will only be sensitive to particles above a cut-off energy η, so, in effect, the visible track length is only a fraction of the total track length, changing our earlier formula to

$$S = F(z) X_0 \frac{E_0}{\epsilon_c}$$

where $F(z) = e^z(1 + z\ln(z/1.56))$ and $z = 4.58Z\eta/(A\epsilon_c)$ [14]. There is an intrinsic limitation to resolution arising from shower fluctuations. The maximum number of track segments is $N_{max} = E/\eta$ (where E is now the energy of the incident particle) and $\sigma(E)/E \geq \sigma(N_{max})/N_{max}$.

Because one cannot build infinitely deep calorimeters, there is a finite probability that a fraction of the energy will leak out the back (or sides) of the calorimeter. Fluctuations in shower development (particularly in the longitudinal direction) mean that this leakage can give a significant contribution to the energy resolution.

Other contributions that depend on the instrumentation can arise. For example, in detectors (such as the ZEUS detector) that use photomultiplier tubes to detect scintillation or Cerenkov light, fluctuations in the number of photo-electrons emitted in the phototubes can be quite significant.

Finally, very important contribution to resolution comes from so-called "sampling fluctuations". Originally, electromagnetic calorimeters were built from one type of material (homogeneous calorimeters), with the shower development and detection processes arising from the same material. Unfortunately, materials that are good for detecting energy deposition generally do not cause showers to develop quickly (often because of low density). The solution for this is to have alternating layers, one layer of a detecting material (called an active layer), one layer of dense material to cause shower development (called a passive layer), repeated the whole depth of the calorimeter. This type of calorimeter is said to be "sampling", since only a small fraction of the total energy is actually detected. These calorimeters can be very compact because the passive layer can be quite dense. As will be seen in the next subsection, hadron showers develop much more slowly than electromagnetic showers, so the ZEUS calorimeter, to contain both types of showers, needs to either be very big or make use of the compactness provided by DU (depleted uranium) as passive layer* (with density $\approx 20\ \mathrm{g/cm^3}$). Unfortunately, there is a component of resolution associated with the sampling method, again arising from fluctuations.

If ΔE is the energy lost in one sampling step (active plus passive layers), then the number of energy depositions is $N = E/\Delta E$. This number N is governed by the usual (Poisson) error, so that the contribution to energy resolution due to sampling fluctuations is

$$\sigma(E) = \sigma_N \Delta E = \sqrt{N} \Delta E$$

* There are other advantages in using a DU/scintillator sampling calorimeter for hadron calorimetry, but a discussion of this is deferred to the next subsection.

but $\sqrt{N} = \sqrt{E/\Delta E}$, so we have

$$\frac{\sigma(E)}{E} = \sqrt{\frac{E}{\Delta E}}\frac{\Delta E}{E} = \sqrt{\frac{\Delta E}{E}}$$

$$= 3.2\%\sqrt{\frac{\Delta E(\mathrm{MeV})}{E(\mathrm{GeV})}}$$

This, as are most simple calculations, is somewhat naïve and underestimates the error. Additional contributions come from various sources:

- tracks result from pair produced particles and so there are only $N/2$ independent track crossings for totally correlated production (giving a multiplicative factor somewhere between 1 and $\sqrt{2}$, depending on the correlation of pair production)
- multiple scattering increases the effective distance in the active plane by a factor $\sim 1/\cos(\pi\rho_M/X_0)$
- visible track length is reduced to $F(z)S$ for $\eta \neq 0$

This gives

$$\left[\frac{\sigma(E)}{E}\right]_{sampling} = 3.2\%\left\{\Delta E(\mathrm{MeV}) \Big/ \left[F(z)\cos\left(\frac{\pi\rho_M}{X_0}\right) E(\mathrm{GeV})\right]\right\}^{1/2}.$$

On top of this, the energy deposition in the active layers fluctuates according to the Landau distribution giving a further contribution. In a DU/scintillator calorimeter, the contribution of the sampling-type errors has been estimated at a best resolution of $\sim 12\%/\sqrt{E(\mathrm{GeV})}$ [11], which can be contrasted with a high quality homogeneous (NaI) calorimeter that gives a resolution of $\sim 0.3\%/\sqrt{E(\mathrm{GeV})}$.

1.4.2 *Hadron Calorimetry*

As has already been mentioned, we have only recently begun to understand the processes involved in hadron calorimetry. Unlike electromagnetic calorimetry, which has only two components in its showers — photons and electrons — produced in a few, well understood ways, hadron calorimetry involves many types of particles produced by a wide range of processes and which give rise to very different responses in the calorimeter. To understand the final signal measured by one's electronics, there must be a good understanding of all processes and a clear idea of how each one contributes to the measured signal. There is still some disagreement on this final issue, but the understanding is good enough to allow the construction of high-resolution hadron calorimeters.

A hadron shower follows very roughly the pattern of an electromagnetic shower: the hadron interacts with the nuclei in matter, producing more hadrons (and other particles) which in turn interact with other nuclei. The first step of the hadron-nucleus interaction is the so-called intranuclear cascade in which the hadron collides with a single nucleon in the nucleus, producing other hadrons (primarily protons, neutrons and pions) which usually escape the nucleus to interact with other nuclei, continuing the showering. The second step involves the de-excitation of the nucleus, in which it loses the energy gained from the collision by "evaporating" off neutrons, protons, deuterons and alpha particles (with the emission of photons) or by undergoing a fission into two smaller nuclei with the release of neutrons and photons. The third step of the showering process is the decay of hadrons that produces muons (that will themselves decay), electrons , neutrinos and photons (as well as more hadrons). A final element in the showering is the "delayed neutron-capture" process in which photons are produced as low-energy neutrons are captured by nuclei. As can be seen, a wide variety of very different particles are produced with a wide range of energies.

It should be noted that, unlike electromagnetic showers in which all of the energy is carried by detectable particles, much of the energy in a hadron shower is lost in overcoming the nuclear binding energy for the release of the outgoing hadrons, as well as in the production of undetectable neutrinos. In addition to the complication of lost energy, there is the problem that the fraction that is lost varies from shower to shower.

The detectable energy deposit comes from a number of different mechanisms : 1) Ionization losses by charged particles such as muons, pions, protons, etc. 2) Neutral pions, which can be created near the beginning of the shower with a very large fraction of the energy, decay to high-energy photons which shower electromagnetically. 3) De-excitation and fission of nuclei produce large numbers of low-energy photons which have an important contribution to the signal. 4) De-excitation and fission of nuclei also produce large numbers of low-energy neutrons which provide one of the principle mechanisms for tuning the signal, as we shall see.

Before looking at the detector response to the various particles, it is helpful to discuss briefly the usual reference particle, the "minimum-ionizing particle", or "mip". Charged particles traversing matter lose energy through ionization of the medium. The ionization energy loss per unit length is very high for low-energy particles, dropping to a minimum with increasing energy and then rising slightly as one gets to very high energy particles (see figure 1.7). The mip is a hypothetical particle that has an energy loss exactly equal to the minimum of the ionization loss curve. A muon or pion will lose energy in a way similar to a mip, however there are other processes that can occur and the muon (or pion) cannot remain at the correct energy for minimum loss (since it is constantly losing energy). As well, the actual energy loss is governed by statistical fluctuations and is not fixed as for the mip. However unrealistic, this ideal mip provides a useful reference for comparing the response to particles in the calorimeter.

In calorimetry, one frequently refers to, for example, the e/mip ratio, meaning the ratio of electromagnetic response to mip response. For hadron calorimetry, the e/h

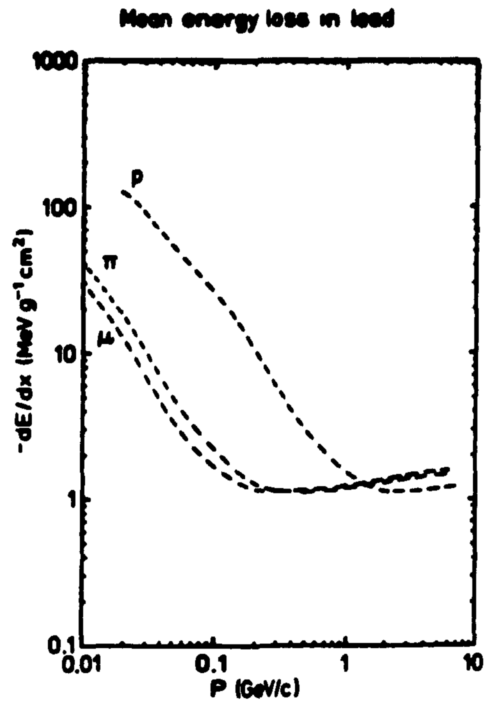

Figure 1.7 : Mean energy loss through ionization for muons, pions and protons in lead (Review of Particle Properties).

value is critically important. This is the ratio of electromagnetic shower response to hadron shower response. Because of the decay of π^0's to photons a significant fraction of hadron shower energy can go into an electromagnetic shower. If the response to electromagnetic showers and hadron showers is not equal, then measurement of incident energy will vary with the fraction of energy in the electromagnetic shower. Thus one seeks $e/h = 1$. Typically, the response to hadrons is less than that to electromagnetic showers, so we speak of "compensation" — boosting the hadron signal to reduce e/h to one. Because of the many different particles involved in a hadron shower, and the very different responses that they induce, the task of getting $e/h = 1$ and obtaining the best possible resolution is far from trivial.

We begin by going back for a second look at electromagnetic showers. It has long been known experimentally that electromagnetic showers give a signal in sampling calorimeters less than that due to an equivalent track length of minimum-ionizing particles, that is, $e/mip < 1$ (a typical value is $e/mip \approx 0.6$). This has traditionally been called the "transition effect", since it was thought to arise from the boundary between layers of different Z (atomic number). Brückman et al have proposed a new name — the "migration effect of γ-energy" — to more accurately represent the cause of this signal suppression. At the end of an electromagnetic shower, there is a very large number of low-energy photons — enough that their total energy is quite significant. The dominant process at these energies ($E_\gamma < 1$ MeV) is the photo-electric effect. The cross-section for this mechanism is proportional to Z^5, whereas the cross-section for ionization is proportional to Z. Because of the large difference in Z between active and passive layers, these photons will interact essentially only with the absorber atoms (passive layer). The photo-electron produced by the interaction can only travel of the order of tens or hundreds of microns (depending on its energy), so for it to contribute at all to the signal, the interaction must occur close to the boundary between passive and active layers. The value of e/mip can be tuned to some degree by varying the thickness of the passive layer, as well as the thickness of the active layer. The e/mip value can be reduced (for very high-Z absorbers) by inserting a low-Z foil between passive and active layers. This foil prevents photo-electrons from travelling from the passive layer (where they are produced) to the active layer (where they are detected).

The third type of particle mentioned is the low-energy photon, generally produced in nuclear de-excitation or fission. Although a significant fraction of the total energy is carried by these particles, they suffer from the same suppression as low-energy photons from electromagnetic showers. Before any theoretical understanding of hadron calorimetry came about, it was found experimentally that uranium/scintillator calorimeters gave the best resolution and came closest to achieving $e/h = 1$. This was thought to come from the addition of fission to the processes, however Leroy et al [24] have found that the number of fissions is less than was previously assumed, and the signal from the nuclear γ's is significantly reduced (with $\gamma/mip \approx 0.4$).

We now come to the crucial element of hadron showers for calorimeter response: the low-energy neutrons. These neutrons carry a very large fraction of the total energy, and yet are not directly detectable themselves (being neutral, they do not ionize the medium). The neutrons do interact with the nuclei, producing low-energy γ's, but these do not contribute very strongly to the signal, as we have seen. The saving factor is the use of hydrogen-containing material (such as plastic scintillator) in the active layers. When neutrons scatter from most nuclei, they do not lose much energy because the recoil nuclei are so much more massive than the neutron. However, hydrogen nuclei are just protons — approximately the same mass as neutrons. When neutrons scatter from protons, they lose much of their energy, and produce recoil protons that deposit almost all of their energy as *detectable* signal (since these protons are in the active layer). The low-energy neutrons travel through the passive layers almost without energy loss, but lose a very large fraction in the active layers. There is, however, partial suppression of this effect in scintillator because the ionization losses of the recoil protons are so high (see the low energy region of figure 1.7) that they saturate the scintillator according to Birk's law [7]. The end result, though, is that the e/h value can be tuned by varying the relative active/passive layer thicknesses. Increasing the thickness of the passive layer reduces e/mip since a smaller fraction of the energy is sampled, but leaves n/mip more or less unchanged since almost all of the recoil energy deposition is in the active layer.

There is an additional element of tuning that comes from the delayed neutron-capture. The low-energy photons emitted by this process appear over a long period, giving the signal a long tail. By varying the gate width over which one measures signal, one can include more or less of this signal, increasing or decreasing n/mip, with its consequent effect on e/h.

Wolf [7] illustrates the tuning of e/h through a nice, over-simplified calculation. The hadron energy is distributed through four mechanisms : 1) π^0 decay (energy E_1 yielding signal $G_e(E_1)$), 2) charged hadrons (energy E_2 yielding signal $G_x(E_2)$ through ionization losses), 3) low-energy neutrons (energy E_3 yielding signal $G_{rec}(E_3)$ through recoil protons), and 4) invisible energy in the form of binding energy (energy E_4 with no signal yield). The signal from nuclear γ's is neglected (and the energy included in E_4).

We assume that the pulse height is proportional to E, that is $G_i(E) = g_i E$ (where $i = e, x, rec$), and that the energy of the neutrons is proportional to the binding energy losses, or $E_3 = aE_4$. Finally, we assume that all of the energy goes into the four components : $E = E_1 + E_2 + E_3 + E_4$.

We then have

$$\begin{aligned} \frac{h}{e} = \frac{G_h(E)}{G_e(E)} &= \frac{g_e E_1 + g_x E_2 + g_{rec} E_3}{g_e E} \\ &= \frac{E - E_2 - \left(1 + \frac{1}{a}\right) E_3}{E} + \frac{g_x}{g_e}\frac{E_2}{E} + \frac{g_{rec}}{g_e}\frac{E_3}{E} \\ &= 1 - \left[1 - \frac{g_x}{g_e}\right]\frac{E_2}{E} - \left[\left(1 + \frac{1}{a}\right) - \frac{g_{rec}}{g_e}\right]\frac{E_3}{E} \end{aligned}$$

We now make an only approximately true assumption : that pulse heights from electrons and from hadron ionization losses are equal, so that $g_x = g_e$. This gives

$$\frac{h}{e} = 1 - \left[\left(1 + \frac{1}{a}\right) - \frac{g_{rec}}{g_e}\right]\frac{E_3}{E}$$

To get $e/h = 1$, we need

$$\frac{g_{rec}}{g_e} = 1 + \frac{1}{a}$$

Tuning of g_{rec}/g_e can be done by varying the ratio of widths of active and passive layers.

The resolution of a DU/scintillator calorimeter with $e/h = 1$ is given as the sum in quadrature of an intrinsic resolution and a sampling resolution :

$$\frac{\sigma(E)}{E} = \frac{22\%}{\sqrt{E}} \oplus \frac{0.09\sqrt{\Delta E(1 + 1/N_{pe})}}{\sqrt{E}}$$

where E is in GeV, ΔE (energy loss per layer) in MeV and N_{pe} is the number of photo-electrons seen by the phototube (this term arises from statistical fluctuations in the light measurement of the phototubes). For a typical calorimeter this leads to a resolution of $\sigma(E)/E = (33\%\text{–}35\%)/\sqrt{E}$.

Traditional, non-compensating calorimeters achieve best resolutions of approximately $60\%/\sqrt{E}$. As well, these calorimeters do not have resolutions that scale as $\sqrt{E}$ — for high energies, the resolutions do not continue to improve. Furthermore, these calorimeters are not very linear as a function of energy — a rather important aspect of calorimetry.

There have been attempts to improve the resolution of non-compensating calorimeters by estimating the fraction of energy deposited through π^0 decay (the electromagnetic fraction), and performing an off-line weighting. Despite the practical difficulty of reading out separately every layer of the calorimeter, the CDHS collaboration did this with some success (see figure 1.8), but their signal was still not linear with energy (see figure 1.9). The results from the HELIOS compensating DU/scintillator calorimeter are much better (see the same two figures). The resolution continues to improve with energy, down to 2.8% at 200 GeV (at this point the contribution of noise in the electronics becomes significant), and the signal is linear with energy.

The success of these ideas has been the construction of a compensating lead/scintillator calorimeter by the ZEUS group (test 36 [10]) with $e/h = 1.05 \pm 0.04$ for

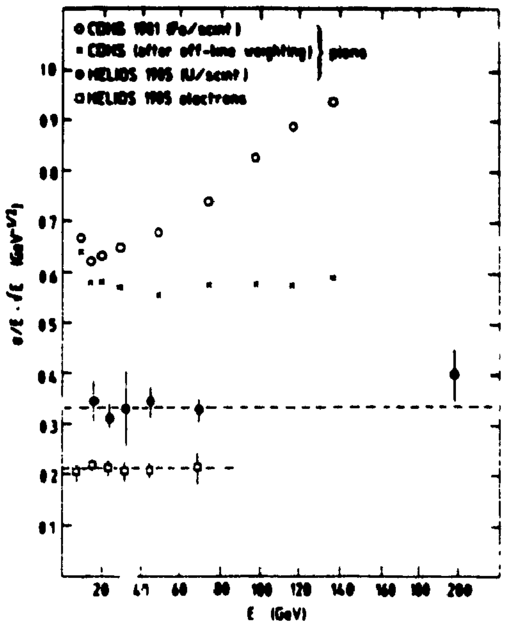

Figure 1.8 : The $\sigma/\sqrt{E}$ ratio as a function of energy for the CDHS iron/scintillator non-compensating calorimeter before (open circles) and after (crosses) an off-line weighting procedure, and for the HELIOS DU/scintillator compensating calorimeter (closed circles) [19].

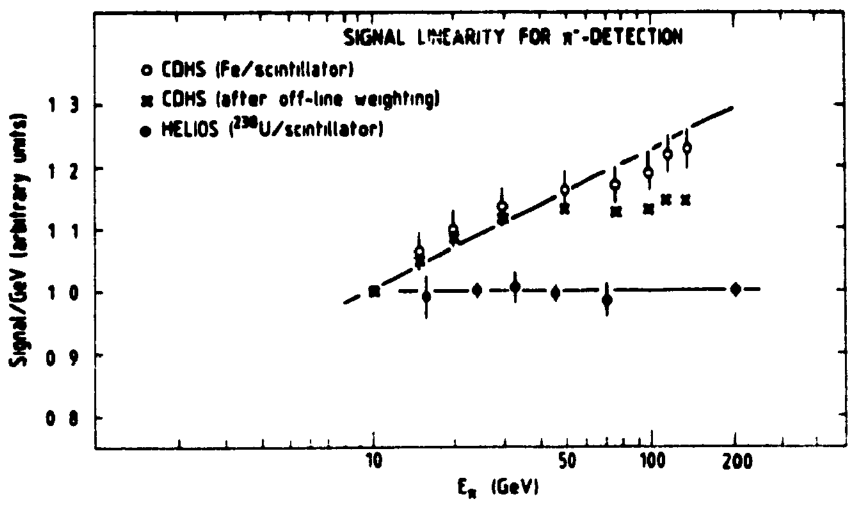

Figure 1.9 : The signal/energy ratio as a function of energy for the CDHS (open circles and crosses) and HELIOS (closed circles) calorimeters [19].

$E > 10$ GeV and $\sigma/E = (44.2 \pm 1.3)\%/\sqrt{E}$. Despite this success, there is still some contention that this picture is not entirely correct. Some of the difficulties arise from calorimeters with liquid argon as detector that should not benefit from compensation due to recoil protons. This in general has been the experience, but Fesefeldt [22] indicates that a DU/liquid argon calorimeter has been built that does have good resolution and $e/h \simeq 1$, and he attributes this to other processes. Despite any controversy that may exist, there remains the all-important fact for our purposes: it is possible to build high-resolution hadron calorimeters that meet the requirements for the ZEUS detector.

References

[1] Cashmore, R.J., *The Physics at ep Colliders*, 1986, Oxford preprint 75/86.

[2] *CHEER: Feasibility Study Report*, September 1980.

[3] Halzen, Francis and Alan D. Martin, *Quarks and Leptons: An Introductory Course in Modern Particle Physics*, Wiley (New York), 1984.

[4] Llewellyn Smith, C.H., *Physics at Future High Energy Colliders*, 1986, Oxford preprint 72/86.

[5] Perkins, Donald H., *Introduction to High Energy Physics*, Addison-Wesley (Reading, Massachusetts), 1982.

[6] Rückl, R., *Physics at HERA*, March 1987, DESY preprint 87–021.

[7] Wolf, G., *HERA: Physics, Machine and Experiments*, August 1986, DESY preprint 86–089.

[8] *ZEUS - A Detector for HERA*. Letter of Intent, June 1985.

[9] *The ZEUS Detector: Technical Proposal.* March, 1986.

[10] *The ZEUS Detector: Status Report 1987.* September, 1987.

[11] Fabjan, C.W., *Calorimetry in High-Energy Physics*, April 1985, CERN preprint EP/85-54.

[12] Hayakawa, S., *Cosmic Ray Physics: Nuclear and Astrophysical Aspects*, Wiley (New York), 1969.

[13] Jackson, J.D. *Classical Electrodynamics*, Wiley (New York), 1975.

[14] Kleinknecht, K., *Particle Detectors*, Physics Reports, Vol. 84 (1982), pages 85-161.

[15] Leroy, C., *Calorimetry in High Energy Physics*, Lecture notes, McGill University, 1987.

[16] Longo, E. and I. Sestili, *Monte Carlo Calculation of Photon-Initiated Electromagnetic Showers in Lead Glass*, Nuclear Instruments and Methods, Vol. 128 (1975), pages 283-307.

[17] Nelson, W.R., H. Hirayama and D.W.O. Rogers, *The EGS4 Code System*, December 1985, Slac publication SLAC–265.

[18] Rossi, Bruno, *High-Energy Particles*, Prentice-Hall (New York), 1952.

[19] Åkesson, T. et al, *Performance of the Uranium/Plastic Scintillator Calorimeter for the HELIOS Experiment at CERN*, Nuclear Instruments and Methods of Physics Research, Vol. A262 (1987), pages 243–263.

[20] Brückman, Hanno, Bernd Anders and Ulf Behrens, *Hadron Sampling Calorimetry, A Puzzle of Physics*, Nuclear Instruments and Methods in Physics Research, Vol. A263 (1988), pages 136–149.

[21] Brückman, Hanno et al, *On the Theoretical Understanding and Calculation of Sampling Calorimeters*, July 1987, DESY preprint 87–064.

[22] Fesefeldt, H., *The e/h Ratio and Energy Resolution of Hadron Calorimeters*, Nuclear Instruments and Methods of Physics Research, Vol. A263 (1988), pages 114–135.

[23] Klanner, Robert, *Test Program for the ZEUS Calorimeter*, June 1987, DESY preprint 87–058.

[24] Leroy, Claude, Yves Sirois and Richard Wigmans, *An Experimental Study of the Contribution of Nuclear Fission to the Signal of Uranium Hadron Calorimeters*, Nuclear Instruments and Methods of Physics Research, Vol. A252 (1986), pages 4–28.

[25] Tiecke, H., *Performance of a Hadron Test Calorimeter for the ZEUS Experiment*, Nuclear Instruments and Methods in Physics Research, Vol. A263 (1988), pages 94–101.

[26] Wigmans, Richard, *High Resolution Hadron Calorimetry*, Invited talk given at the International Conference on Advances in Experimental Methods for Colliding Beam Physics, SLAC, March 9–13, 1987.

[27] Wigmans, Richard, *On the Energy Resolution of Uranium and Other Hadron Calorimeters*, Nuclear Instruments and Methods in Physics Research, Vol. A259 (1987), pages 389–429.

[28] The ZEUS Collaboration, *Development of the ZEUS Detector*, December 1987, DESY preprint 87–165.

Chapter 2 – The Prototype Calorimeter

2.1 The History of ZEUS Prototype Calorimeters

The design of the final ZEUS prototype calorimeter was not reached before much development work had been done [1], [2]. Uranium/scintillator calorimeters have been developed by various groups, including two CERN experiments: HELIOS and WA78. The first ZEUS test calorimeter was an extension of the WA78 work: test WA78/HERA [3]. This has been followed by three more ZEUS tests: test 35, 60 (including three calorimeter set-ups — A, B and C) [4] and 36. These tests were concurrent with the development of hadron calorimetric theory, providing evidence to support (or refute) ideas, as well as being guided by the theory (principally the ideas of Wigmans [5] and Brückman et al [6]). The following sections outline the nature and results of the first three of these tests. The last one (test 36) involved the construction of a compensating lead/scintillator calorimeter that achieved a hadron energy resolution of $\sigma_h/E_h = (44.2 \pm 1.3)\%/\sqrt{E}$ and an $e/h = 1.05 \pm 0.04$ for $E > 10$ GeV, providing confirmation of some predictions of the theory.

2.1.1 *Test WA78/HERA*

This calorimeter consisted of two parts : an electromagnetic section with 1.5 mm DU (depleted uranium) plates and 4 mm plastic scintillator plates, followed by, in the longitudinal direction (direction of showering), a hadronic section with 10 mm DU and 5 mm plastic scintillator plates. The hadronic section was read out at 0.45λ segments (λ = absorption length which describes the showering depth) — contrast with the prototype which is read out by 3λ segments — and the calorimeter had a total depth of 5.2λ. An iron backing calorimeter was used to detect leakage through the DU/scintillator calorimeter.

The calorimeter was tested with beams of electrons, hadrons and muons in the energy range 5 to to 210 GeV. The principal result was an e/h ratio of 0.8, that is, over-compensation (arising from too much DU to scintillator). This helps demonstrate tuning of e/h by varying relative scintillator/DU thickness. As well, the signal integration time was varied, with a corresponding change in e/h arising from the slow neutron component in the showers. Finally, the fine, longitudinal segmentation of the calorimeter allowed measurements of the longitudinal energy deposition of hadron showers, which has been important in understanding leakage and in optimizing the depth of the final calorimeter.

2.1.2 *Test 35*

This test reduced the amount of DU to bring e/h closer to one. The DU thickness was 3 mm and the scintillator thickness was 2.5 mm. Three modules from HELIOS were re-stacked to have a tower configuration similar to that of the final ZEUS forward calorimeter. Towers were 20 cm $\times$ 20 cm in the transverse dimensions, read out by WLS (wavelength shifter) bars with no longitudinal segmentation over the 4.2λ depth. To achieve a uniform readout along the calorimeter depth, the WLS was backed by aluminum foil of varying reflectance (done by blackening the foil appropriately) to compensate for absorption of light in the WLS (that is, low reflectance near the readout end of the WLS, and high reflectance at the other end). This technique is now used for the prototype.

Data for this set-up was taken at a lower energy range : 3 – 9 GeV. An e/h ratio of 1.08 was attained giving an energy resolution for hadrons of $33.7\%/\sqrt{E}$. Deviations from Monte Carlo predictions were consistent with energy loss through leakage and with inhomogeneities in the readout. As well, e/h tuning was again done by varying the signal integration time. Finally, the signal resolution was found to scale with $1/\sqrt{E}$, and the alinearity in mean pulse height was less than 1.5% for hadrons.

2.1.3 *Test 60*

This test consisted of three different set-ups, the first two (A and B) being uranium/scintillator calorimeters, and the third (test T60C), a lead/scintillator calorimeter. Each calorimeter consisted of a number of 60 cm $\times$ 60 cm (transverse dimensions) modules, one behind the other, giving longitudinal segmentation. In one transverse dimension, the scintillator was divided into 5 cm strips so that some information on the transverse development of showers was available (allowing estimation of the side leakage).

The modules for test T60A consisted of plates of 5 mm thick scintillator and 3.2 mm thick DU plates, giving a module depth of 1.1λ. Four of these modules were used with a total depth of 4.4λ. T60B modules were constructed using the same DU plates as T60A, but with scintillator plates that were only 3mm thick. More layers were used in the T60B modules, with a module depth of 1.5λ. Again, four modules were used, but with a total depth of 6.0λ, and one of the T60A modules was used as a backing calorimeter to measure longitudinal leakage.

Test T60A was done using electrons and hadrons in the energy range 3 – 8.75 GeV, whereas test T60B was done with energies 10 – 100 GeV. There were three stages to test T60B, the first as already described, the second with a graded grey filter introduced between the scintillator and the WLS (the light was attenuated in the WLS, as mentioned for test 35, and this filter helped compensate for this fact), and the third part involved the wrapping of the DU plates with 0.2 mm stainless

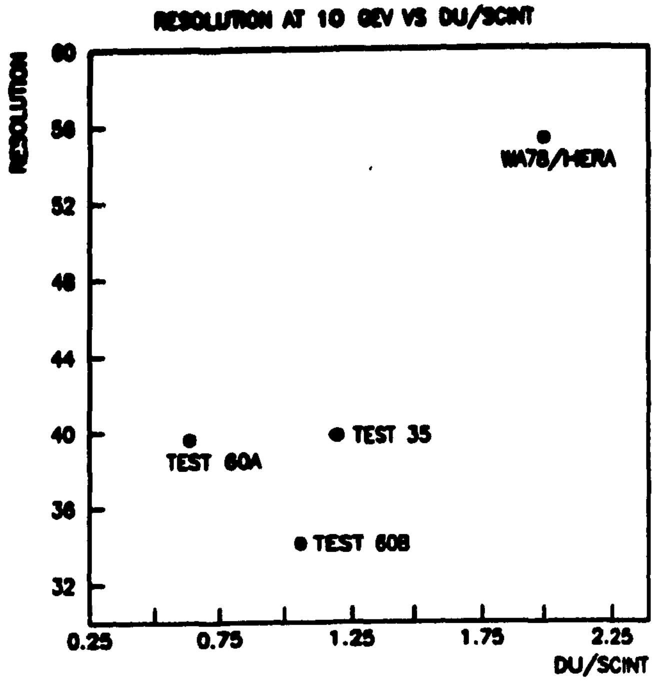

Figure 2.1 : Resolutions ($\sigma/\sqrt{E}$) at ~10 GeV for the various test calorimeters as a function of the ratio of DU to scintillator thickness.

steel (this wrapping, or cladding, provides important structural advantages, improves safety — an important consideration for the final calorimeter — and helps reduce the effect of the natural uranium radioactivity).

Test T60A had the worst resolution and e/h ratio (the scintillator was too thick), giving $\sigma/E \sim 39\%/\sqrt{E}$ and $e/h \sim 1.07$. The three T60B tests have their best results in the third part, with a resolution of $34.1\%/\sqrt{E} \oplus 1.3\%$ ($\oplus$ means add in quadrature) and an $e/h \sim 1.02$.

The tests all give information on how one can tune e/h and demonstrate that the desired resolution is attainable (see figure 2.1). They also provide important information on the influence of various parameters on performance, including leakage, readout inhomogeneities, signal integration time, stainless steel cladding of the DU plates, etc. This leads us to the final design for the calorimeter and the construction of a prototype.

2.2 The Mechanical Design and Stacking

The forward calorimeter of the ZEUS detector is approximately circular in the transverse dimensions (perpendicular to the beam direction), with a radius of 230 cm. This shape is created from rectangular objects by subdividing the calorimeter into vertical strips, or "modules", 20 cm wide, with heights that vary from 460 cm at the middle to 230 cm at the outside (see figure 2.2). These modules are then divided into 20 cm × 20 cm towers, read out at three depths. In this longitudinal direction (the direction of incoming particles), we have first the EMC (electromagnetic calorimeter) with four adjacent 5 cm × 20 cm towers, or "strips" for every 20 cm × 20 cm tower to give a better position resolution (each with a depth of 25 DU/scintillator layers = 0.960λ = $25.9X_0$ — every layer is approximately one radiation length thick). This is followed by two successive hadron calorimeter sections, HAC1 and HAC2 (each with 80 DU/scintillator layers = 3.09λ). The total depth is 185 DU/scintillator layers = 7.14λ. The final segmentation as seen from the interaction point is given in figure 2.3. A cut-away view of one module is shown in figure 2.4.

As a consequence of the tests and calculations done, a DU plate thickness of 3.3 mm with scintillator plates of 2.6 mm was chosen. The DU plates are clad with 0.2 mm thick stainless steel (for EMC), or 0.4 mm thick stainless steel (for HAC towers). These plates are held apart by small tungsten carbide spacers, with size chosen to optimize the balance of mechanical support (calling for large spacers) and physics requirements (calling for small spacers to minimize the dead space caused by their presence). These spacers are placed every 20 cm, at the separation between towers (see figure 2.5). The stack of DU/scintillator is held to a supporting spine (which contains the phototubes and their shielding) by stainless steel straps tensioned over

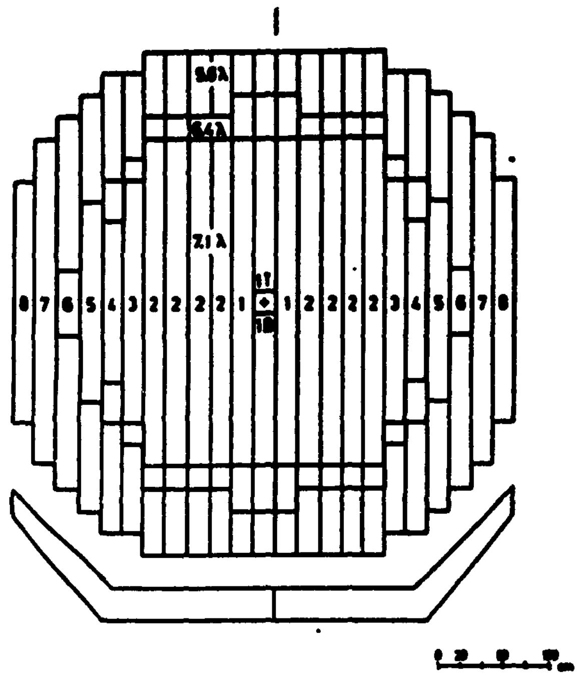

Figure 2.2 : Front view of forward calorimeter showing module segmentation and contours of constant depth in λ [1].

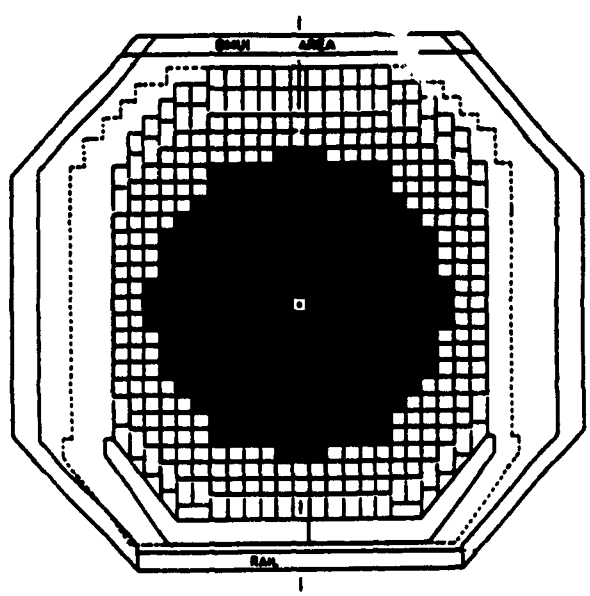

Figure 2.3 : Front view of forward calorimeter as seen from the interaction point showing tower segmentation [1].

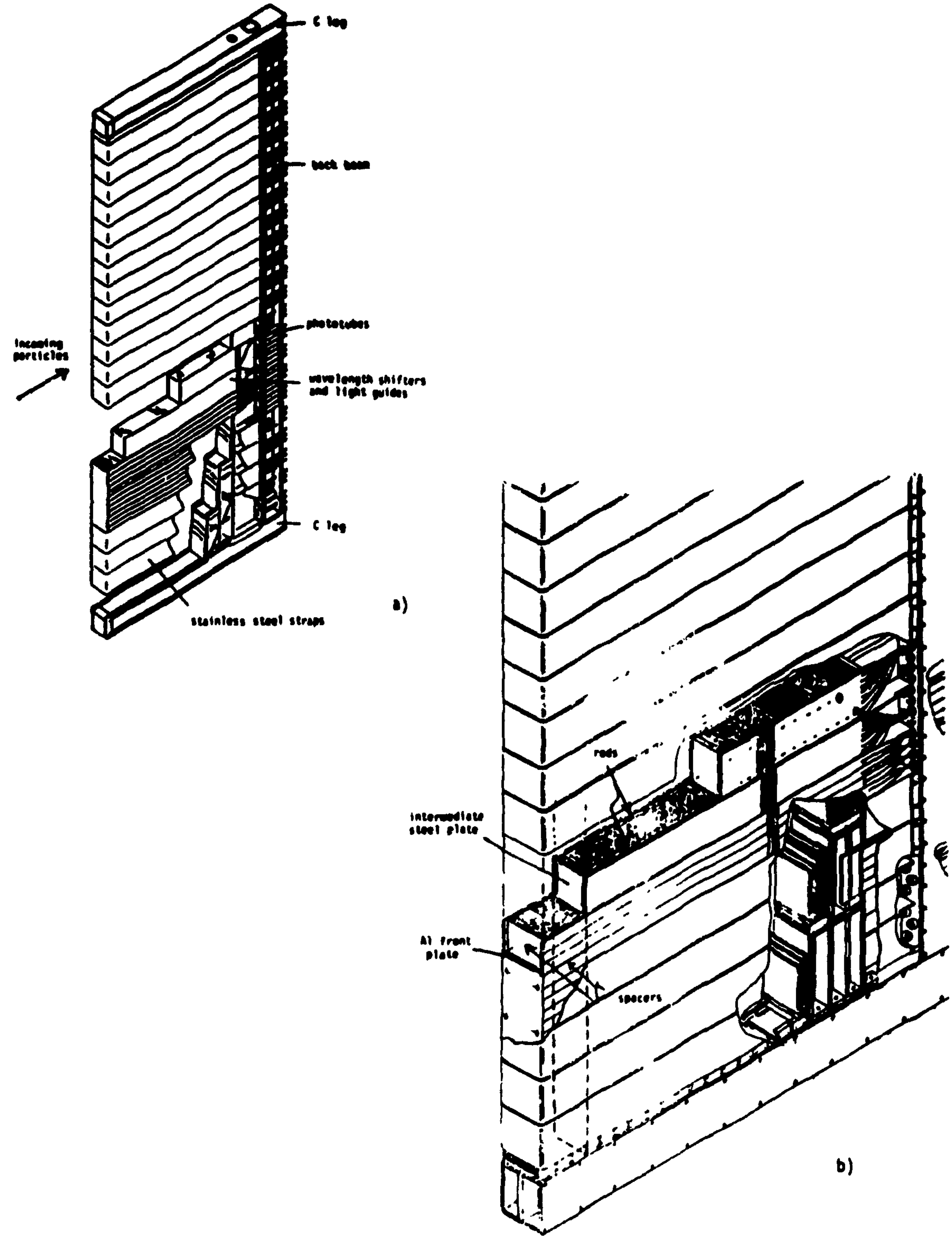

Figure 2.4 : (a) Isometric view of largest forward calorimeter module, and (b) an expanded view [1].

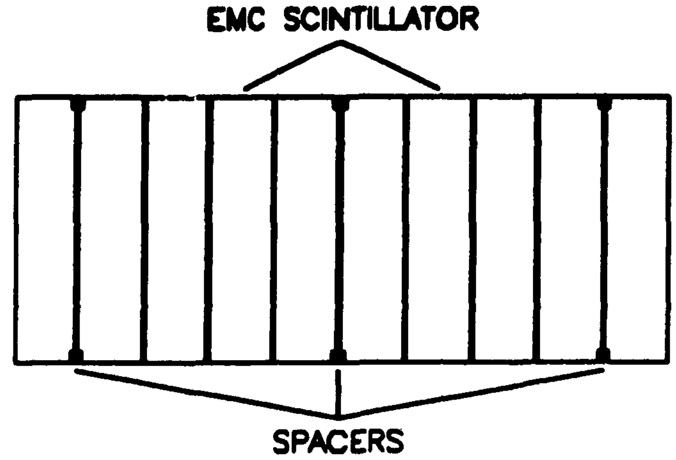

Figure 2.5 : Diagram of the positioning of EMC scintillator and of the tungsten carbide spacers in a layer.

an aluminum front plate. The top and bottom of each module is supported by a steel box beam, called a "C-arm" or "C-leg", fastened to the DU plates and to the backspine. This strap design was chosen over a tension rod design (with rods running through the plates holding the stack together) because the rods give more dead space than spacers, and they would require the drilling of holes in the uranium plates (this difficult and not entirely safe operation would also mean that the cladding would not constitute a hermetic seal, one of its most desirable features).

The prototype calorimeter consists of four modules, each of which has only four towers, thus forming an 80 cm $\times$ 80 cm square. Apart from this, it has essentially the same design as the final calorimeter, and so assembly techniques can be tested in the prototype construction. The assembly is non-trivial since design tolerances are fairly tight, yet DU plate thickness varies significantly from plate to plate (plus or minus about 0.2 mm). This requires careful selection of plates, a precision stacking machine with the capability of measuring small variations in stack height, and the ability to compensate for these variations by using spacers of different thicknesses to prevent systematic errors from building up.

The four prototype modules were stacked at York University in Toronto, Canada, in the fall of 1987. The stacking was done so that horizontal DU/scintillator plates were placed one on top of the other — that is, the calorimeter was upended, as though incident particles arrive from above. The backspine was bolted to a "pallet" which moved up and down on four ball-screws and two Thompson bearings, while DU/scintillator plate assemblies (complete with spacers) were lowered onto it by means of a delivery mechanism guided by Thompson bearings. Digital encoders on each ball-screw gave precise position measurements for the stack, and combined with measurements from compressing hydraulic cylinders at the top of the stack, allowed accurate calculation of stack height at each spacer column, and thus enabled corrections through the appropriate choice of spacer thickness. A photograph of a nearly completed module is given in figure 2.6.

Once the stacking was complete, the module was compressed while C-arms were attached, the optical system (WLS assemblies) was installed, and the straps were put in place, keeping everything firmly fixed to the backspine. This design allows a single strap to be removed for local repairs or adjustments to the module without the need for complex or heavy machinery.

2.3 The Optical Readout

We now turn to the problem of the optical readout system, and how the light created in the scintillator is carried out of the calorimeter stack to the photomultiplier tubes. The specifications of the detector demand very uniform light output and very little attenuation of the light, requiring a very high quality optical system.

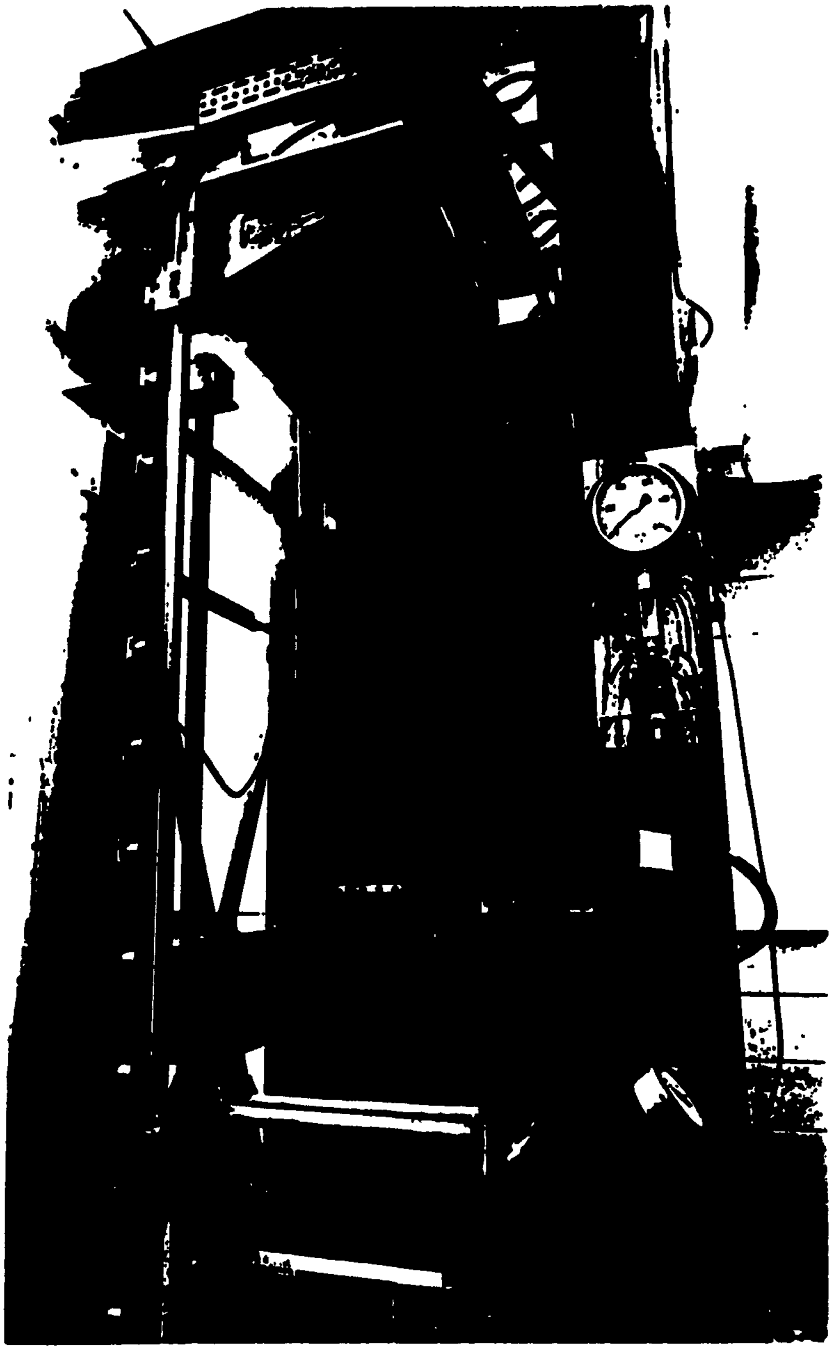

Figure 2.6 : Photo of the stacking machine, assembling the first forward calorimeter prototype [1].

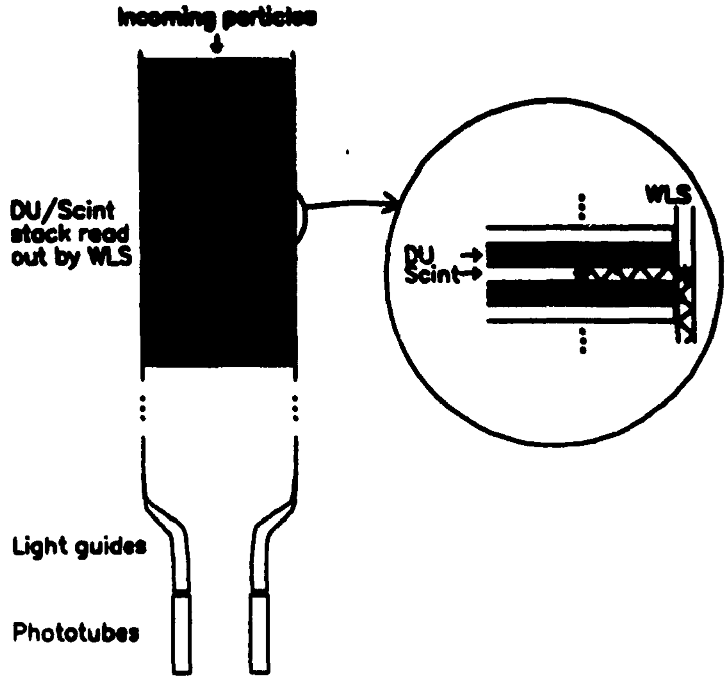

Figure 2.7 : An illustration of the optical readout system. The expanded view illustrates how some of the light created in the scintillator propagates by total internal reflection to the edge of the module where it excites the dye in the WLS. Some of this light is carried to the back of the calorimeter and is directed onto the face of a phototube by a light guide.

The optical readout is illustrated in figure 2.7. The light from the scintillator plates is carried by total internal reflection to the two sides of the modules where it is absorbed in bars of WLS (wavelength shifter) that run the length of the calorimeter (in the direction of incoming particles). Light is re-emitted at a longer wavelength (primarily green light), some of which is carried to the back of the calorimeter by total internal reflection and directed onto the face of a phototube by a light-guide. Figure 2.8 gives the absorption and emission spectra for Y-7, the active dye in the WLS, along with the emission spectrum for the scintillator SCSN-38, and the spectral sensitivity of a tri-alkali phototube cathode. The use of the WLS bars means that the light is re-directed perpendicular to its original path without loss of space, but at the cost of some efficiency.

Each HAC section or EMC strip is read out by two WLS bars, one on each side

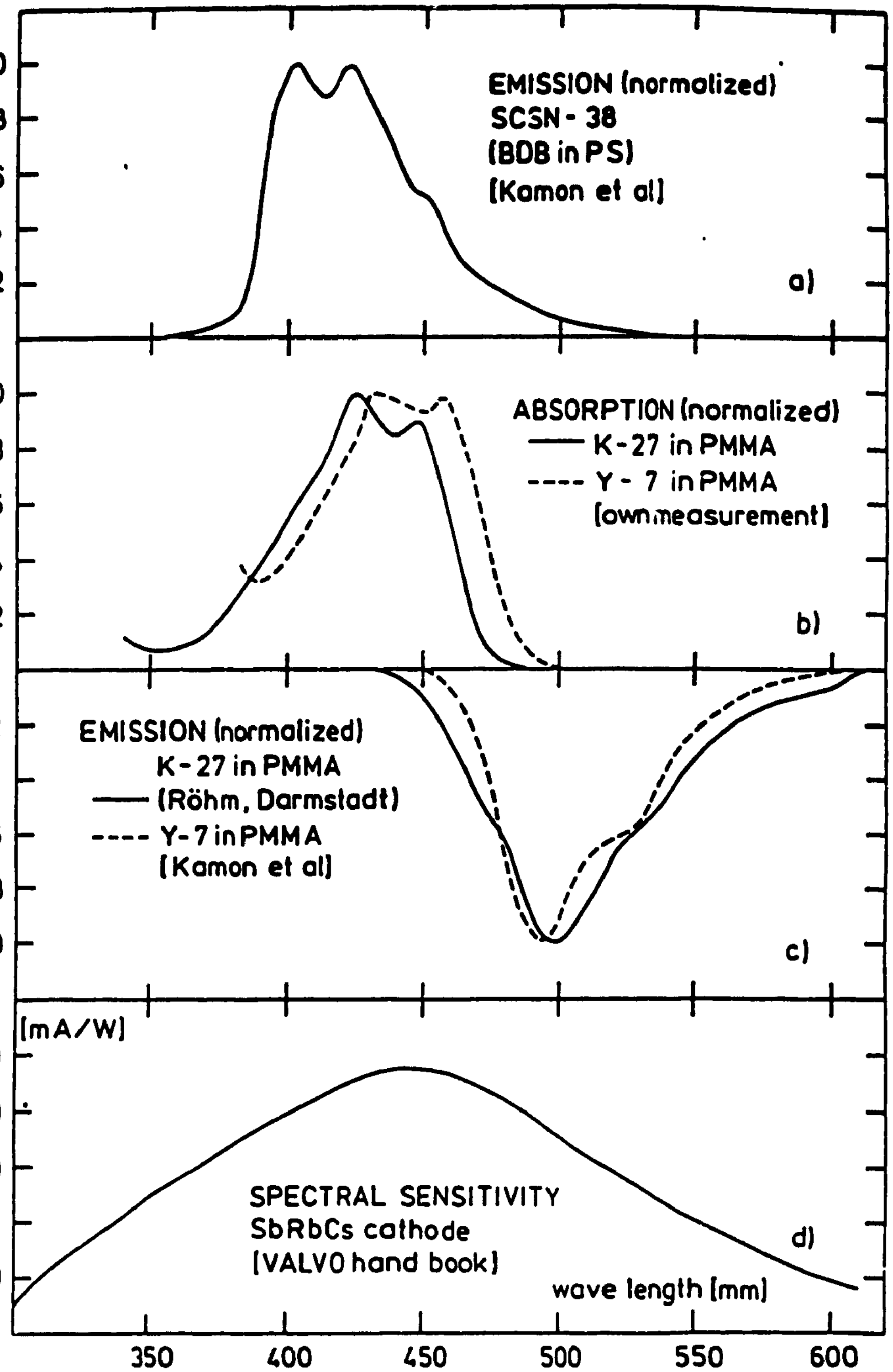

Figure 2.8 : The emission spectrum for SCSN-38, the absorption and emission spectra for Y-7 in PMMA, and the spectral sensitivity of a tri-alkali photocathode [7].

of the module. This gives a total of twelve phototubes per tower (four EMC strips and two HAC sections). The EMC WLS bars are 5 cm wide, and the HAC WLS bars are 20 cm wide, each exposed only to the scintillator plates of its own section.

A problem of uniformity arises from the fact that both the scintillator and the WLS attenuate the light that passes through them (the mean attenuation length is of the order of 50 to 100 cm). This means that the response to the same amount of light created at different positions will be different. For example, light created in the scintillator near the edge of the module will be less attenuated than light created farther from the edge. Likewise, light created near the back of the calorimeter will be less attenuated in the WLS than light created at the front of the calorimeter (which must travel the whole length of the calorimeter).

As has already been mentioned, it is possible to overcome this problem by the use of a reflector on the back of the WLS, and by an ultra-violet reflecting paper wrapped around the scintillator plates. The reflectance from this backing increases the total signal so one can make the response uniform by blacking out the reflector in those regions where the normal signal is high — the result should be that low signals are boosted by the reflector, but high signals are not boosted because the reflector has been blackened. An example of the reflector pattern is given in figure 2.9. The influence of this reflector pattern can be tuned by varying the doping of the WLS. If there is higher doping, all of the light is absorbed on the first time through; if there is low doping, then a significant amount of light will pass through the WLS to be reflected. Additional compensation can be achieved in the WLS (which is read out at only one end) by adding a reflector to the end away from the readout.

One problem that has plagued devices that use plastic scintillator for detection is that the plastic tends to yellow with age, especially when exposed to radiation.

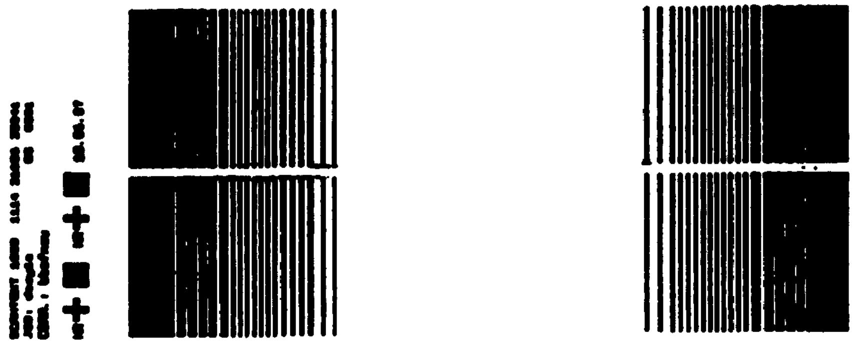

Figure 2.9 : Correction pattern printed on scintillator wrapping to achieve uniformity. Note that the pattern is duplicated, above and below, giving the reflector for both sides of the scintillator [1].

This is a concern for ZEUS since the detector is exposed to much radiation: the beam passes through the core of the calorimeter and can emit very large amounts of radiation, and the uranium within the calorimeter emits its own natural radiation. The problem of massive beam radiation has been partly avoided by building the calorimeter in two halves which can be retracted from the beam line while beam development or injection is taking place (it is during these times that most radiation damage is caused). Members of the ZEUS group have found no significant difference in aging between scintillator plates exposed and not exposed to DU radiation.

The last stage of the optical readout is the photomultiplier tube. This consists of a photo-cathode that emits electrons (called "photo-electrons") when struck by photons, converting a light signal to an electric signal, then a series of dynodes of increasing voltage ending at an anode where an amplified signal is measured. At each stage, the electrons are accelerated by the electric field until they strike the dynode, releasing even more electrons which are accelerated in the next stage. The multiplicative effect gives many more electrons at the anode than originally left the photo-cathode. Although phototubes are very sensitive to even an extremely minute amount of light, their output is also very sensitive to changes in voltage, external electric or magnetic field, temperature and a number of other factors.

A variety of different phototubes have been investigated, testing important properties such as current amplification (total gain over all of the stages) as a function of high voltage, dark current (current measured with no light input) at a given current amplification, linearity of response and dependence of gain on level of background light. Two types of Philips phototubes were selected for the prototype — the XP2081 for the HAC towers, and the XP2972 for the EMC towers. Both types of phototube have circular photocathodes — the XP2081 with radius 32 mm, and the XP2972 with radius 23 mm.

The sensitivity of phototubes to magnetic fields has led to one further design element. Because the calorimeter will be inside the ZEUS magnet, serious deterioration of phototube response can occur. To protect against this, magnetic shielding for each phototube must be provided. Calculations and measurements of magnetic field, phototube sensitivity and shielding metals have been done, and the current design of the shielding has been incorporated into the prototype, even though it is not needed for the principal tests (these tests are not done in a magnetic field).

2.4 Calibration Systems

An essential component in the construction of high-resolution devices is good calibration. Basically, calibration is determining how to relate the individual measurements from one's electronics to each other first of all, and secondly to some absolute scale that has more general meaning. In the ZEUS calorimeter, these individual measurements are charge measurements in an arbitrary scale from all of the phototubes. Depending on the voltages applied to the photomultiplier tubes, they will give different output for the same amount of light, so one of the tasks of calibration is to equalize this output. This can be done both at the hardware level, in the amount of charge emitted by the photomultiplier, to facilitate online use of data (either for triggers or for immediate results), and at the software level, in the numbers used for energy calculation. The second task is to relate the arbitrary scale used in the measurements to the energy of the incident particle (generally measured in GeV). To take advantage of the $35\%/\sqrt{E}$ resolution of the ZEUS calorimeter (which becomes 3.5% at 100 GeV), the individual channels must be calibrated to better than 2%.

Calibration is generally divided into two steps. The first step involves an immediate calibration, allowing energy measurement to the required accuracy. This is often done with particle beams — seeing how the device responds to electrons, hadrons and muons of known energies and correcting the output to give these energies. The second step is a long-term one: monitoring the calorimeter response after or between visits to the beam and correcting for any changes. It is helpful if one can pinpoint the particular component of one's device that has changed, and this requires a number of calibration systems that test different stages of the calorimeter. Because these systems have to be in place while the calorimeter is operating, they must be worked into the design, and so we discuss them here. Most work is ongoing and for purposes of calibration, the prototype calorimeter is not a true prototype, but rather a test bench.

The natural radio-activity of the uranium gives a uniform irradiation of all of the scintillator plates, leading to a continuous background "glow" from the calorimeter. If one integrates signal for long enough (for example, 10 μs, as compared to 100 ns for normal signals), one gets an average measurement for all of the plates of the tower being investigated. This provides a simple way to calibrate the whole calorimeter, from scintillator to electronics without requiring any special modifications to the calorimeter design. One special consideration is plate cladding: the thicker the stainless steel cladding, the smaller the UNO signal (uranium noise, as this type of signal is called). For the EMC strips, with narrower and fewer scintillator plates, this may be problem, reducing the UNO signal to a point where it is so much smaller than normal signals so as not to be useful. Other limitations to this calibration method, especially when used for equalizing channel outputs, include non-uniformities between towers. Variations in optical readout from tower to tower, as well as variations in scintillator and DU plate thickness can affect the relative response of the calorimeter to UNO and to particles. That is, calibrating with one may not give the same result as calibrating with the other. This requires that great care be taken in the construction of each module, with very small tolerances in the structure.

The UNO measurements look at the average behaviour of the whole calorimeter system, from scintillator plates to optical readout to phototubes. If changes do occur, or there are non-uniformities in the system, then it is important to understand where and why they occur. To determine this, one needs other calibration systems, which also provide an important redundancy. One such system uses high-intensity, radioactive γ-sources: cobalt-60 sources that emit photons of energies 1.1 MeV and 1.3 MeV. A source of intensity $\sim$ 40 MBq will give a signal that is about double that due to UNO. These sources can be run the length of the calorimeter through tubes along the WLS bars and irradiate only a very small region at a time (the range is of the order of 1 cm from the source), and so can give an indication of the response of the calorimeter at different depths. This allows one to check for non-uniformities in the WLS readout and look for decreasing attenuation length as the WLS ages. One

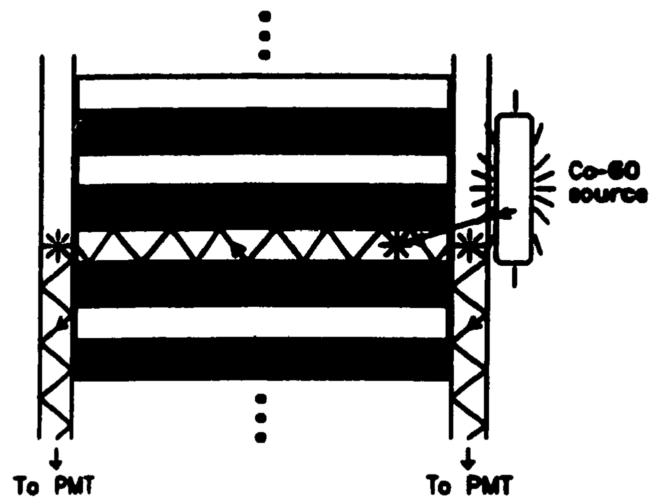

Figure 2.10 : Diagram illustrating attenuation length measurement using a ^{60}Co source. A radioactive particle from the source excites the scintillator, causing the emission of light. There are two paths for this light, one of which must go all the way through the scintillator. Note that this diagram is not to scale: the scintillator plates are in reality 20 cm wide and only a few millimetres thick.

can also look for changes in scintillator attenuation length (a concern due to the high radiation levels) plate by plate by measuring the signal on the side of the module away from the source. The light must travel all the way through the scintillator plate to be measured on the other side, so a decreasing attenuation length will give a smaller signal (see figure 2.10).

A variety of design problems arise from this system, dealing with source length and automation of the source delivery system. These have not been resolved for the prototype, and the source tubes extend straight out of the back of the calorimeter, requiring manual manipulation of sources. Some source testing has been done, but those results are beyond the scope of this thesis.

The final calibration system injects light pulses through the light-guides onto

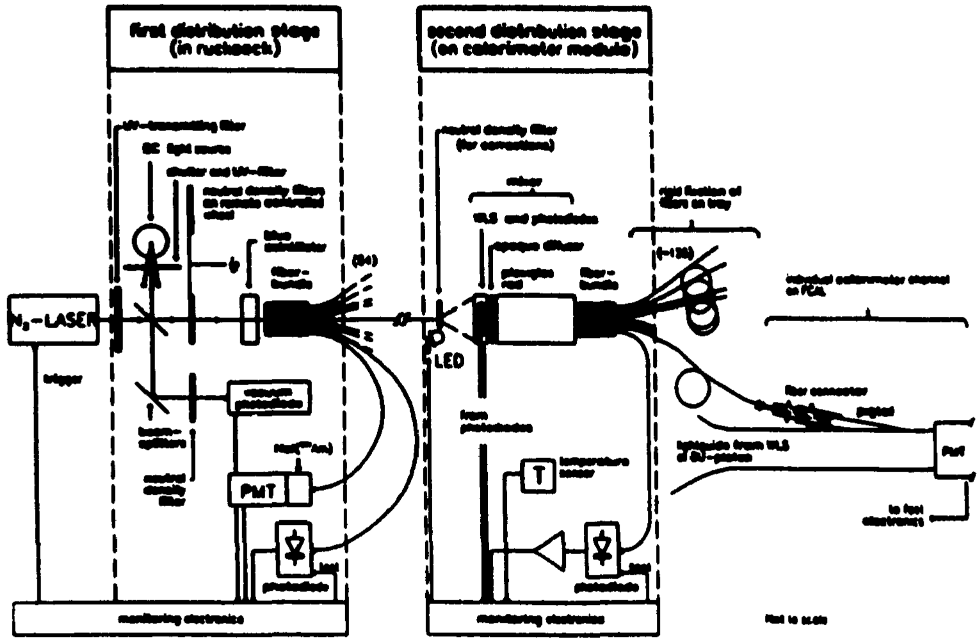

Figure 2.11 : Schematic of a light flasher calibration system [1].

the phototubes, allowing separate calibration and monitoring of the light detection system. A schematic of one such system is given in figure 2.11. Ultraviolet light from a nitrogen laser is shifted to blue light, either through a block of scintillator or a dye laser. This light is carried to all of the calorimeter modules by optical fibres which illuminate a flask of WLS followed by an optical diffuser that produces a diffused, green light of the same wavelength and time structure as that produced in the WLS bars by real showers. The green light is carried to each light-guide by more optical fibres. LED's (light-emitting diodes) on each module provide a second source of light. The light in the system is monitored, both at the first distribution stage by phototubes and photodiodes, and on each module (the second distribution stage) by photodiodes.

This system is quite versatile and allows for a number of tests. First of all, it allows monitoring of the gain of each phototube, checking for drifts in voltage. It also allows testing of tube parameters, including the linearity of tube output over the whole operating range (the laser output can be attenuated by neutral density filters), and the gain as a function of background illumination (a constant, or D.C., light level gives this background).

For best performance, all tubes should have approximately the same level of light. This puts stringent requirements on the optical system. At each distribution, the fibres should all receive a similar amount of light, so careful light diffusion and fibre-face polishing is important. As well, bends in the fibres cause light loss — all the fibres must have the same length and the same bends, and must be fixed to keep the light loss constant. A further difficulty is instabilities in the light source output. Not only does the laser have 5% fluctuations from pulse to pulse, but it tends to drift with time. Careful monitoring by phototubes and photodiodes is essential. To provide a reference signal, an americium source embedded in scintillator is fixed to the face of one of the phototubes, giving a well understood light output to which one can compare laser output.

It is hoped that between these systems, the calorimeter response can be monitored sufficiently well to maintain a calibration of better than 2% over the years of operation of the ZEUS detector, so that the expensive and time-consuming operation of re-calibrating modules in particle beams can be avoided as much as possible.

References

[1] *The ZEUS Detector: Status Report 1987.* September, 1987.

[2] Klanner, Robert, *Test Program for the ZEUS Calorimeter*, June 1987, DESY preprint 87–058.

[3] Catanesi, M.G., *Hadron, Electron and Muon Response of a Uranium-Scintillator Calorimeter*, April 1987, DESY preprint 87–027.

[4] Tiecke,H., *Performance of a Hadron Test Calorimeter for the ZEUS Experiment*, Nuclear Instruments and Methods in Physics Research, Vol. A263, pages 94–101.

[5] Wigmans, Richard, *On the Energy Resolution of Uranium and Other Hadron Calorimeters*, Nuclear Instruments and Methods in Physics Research, Vol. A259 (1987), pages 389–429.

[6] Brückman, Hanno, Bernd Anders and Ulf Behrens, *Hadron Sampling Calorimetry, A Puzzle of Physics*, Nuclear Instruments and Methods in Physics Research, Vol. A263 (1988), pages 136–149.

[7] *The ZEUS Detector: Technical Proposal.* March, 1986.

Chapter 3 – Beam Tests

3.1 General Set-up

In November and December of 1987, the first tests on the forward calorimeter prototype were done in the T7 particle beam at the CERN proton synchrotron (PS) in Geneva. The primary beam of 28 GeV/c protons collided with a target to provide a secondary beam of negatively charged particles that could be tuned to specific momenta in the range 1 to 10 GeV/c. These particles included hadrons (mostly pions plus a few exotic particles such as kaons), electrons and muons. Because the PS beam supplies particles for a variety of purposes, our experimental area received particles for only one second out of every thirty.

The prototype calorimeter was mounted on a solid metal framework, referred to as a "table", that allowed movement in the two transverse dimensions (vertical and horizontal). A precise electronic scale provided vertical position information and a rougher mechanical scale provided horizontal position (accurate to the nearest millimetre). Since the scale of the smallest features of the calorimeter are of the order of one centimetre, a millimetre accuracy is more than adequate.

Because of a tight construction and testing schedule, not all of the prototype modules were immediately available for testing. The first tests (in November, 1987) were done with only one module, allowing the important task of getting all systems into working order, and giving preliminary results for electrons (electron showers are fully contained by one module). A few weeks later (early December, 1987), module two, and then module three, was added to the first giving a complete calorimeter able to contain hadron showers as well as electron showers. The final module was not ready for those tests, but has since completed the quartet. The results given in chapter four come primarily from the tests in early December, 1987, with two or three modules in the beam.

The light-flasher calibration system was also partly installed, with a second-level distribution box mounted on each module. This allowed tests with both the LED source (flashing or at a constant light level) and the nitrogen laser.

The particle beam could be controlled by changing the currents in a number of bending magnets and the settings of a few collimation slits. This enabled one to select both particle momentum and beam size (as well as allowing special configurations to raise the relative fraction of muons in the beam by blocking other particles). Particle passage was detected by a trigger made up of scintillation counters and Cerenkov counters in front of and behind the calorimeter. This system is described in detail in the next section.

The signals from the calorimeter channels were delayed by sending them through long cables. A VME-based computer read them out through ADC's (Analog-to-Digital Converters) in CAMAC crates. A full description of the readout and electronics will come in section three of this chapter.

3.2 Beam Trigger and Particle Identification

A schematic diagram of the trigger counters is given in figure 3.1. The counters labelled "Bn" (where n is some digit) are scintillation counters: plates of plastic scintillator fixed to phototubes. These counters are used simply to mark the passage of a particle through the scintillator plate. Two of them placed in a line (for example, B1 and B2) will give simultaneous signals when a beam particle passes through them.

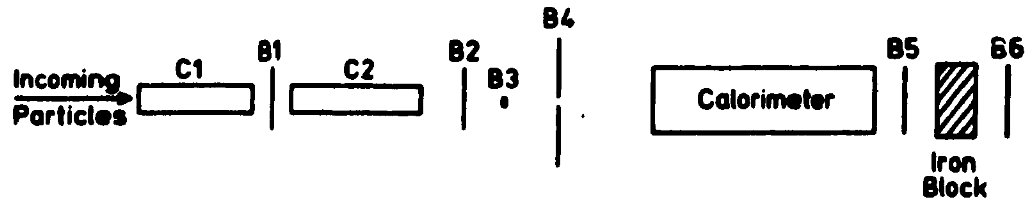

Figure 3.1 : A schematic diagram of the trigger counters. Counters labelled "B" are scintillation counters; those labelled "C" are Cerenkov counters. Counter B3 is a finger counter and B4 is a halo counter. See text for more details.

The counter B3 is a "finger counter": a very narrow counter (0.5 cm wide) that allows one to select only the particles at the centre of the beam, giving a better position resolution. Counter B4 is a "halo counter": a large plate with a hole in the middle. If there is a signal, then the particle has missed the hole or another particle accompanied the triggering particle. Used in conjunction with B1, B2 and B3, one looks for no signal in B4 to trigger a reading of the calorimeter output (that is, only when a single particle travelling in the correct direction, along a narrow path, enters the calorimeter).

The counter B5 allows identification of muons. Since it is behind the calorimeter, it will only fire (at the same time as B1 and B2) if the particle travels right through the calorimeter. In general, the only detectable particle to do this is the muon. A further counter, B6, is placed after a thick piece of iron, enabling one to look for muons above a certain energy (low energy muons would stop in the iron). This counter was not used in the muon runs taken on tape (all muons were initially 5 GeV, so low energy ones were not a problem).

The counters C1 and C2 are Cerenkov counters. The speed of light, v, in matter is generally less than c. When a charged particle passes through that matter with a velocity greater than v (but less than c), a light wave is emitted, analogous to the bow wave of a boat passing through water or the shock wave of a supersonic aircraft. This is called Cerenkov radiation. The angle, frequency and intensity of this radiation depend, for a given material, on the velocity of the particle (see, for example, Jackson [1], pp. 638–641). The Cerenkov counters exploit this phenomenon to distinguish between particles of different mass. The counters each consist of a long pressure tube filled with CO_2 gas and a phototube at the end. When a particle with velocity above the speed of light in the gas passes through the counter, a signal is measured. Since all particles have the same momentum p, the lighter ones will have a higher velocity, $\beta = pc/E = p/\sqrt{p^2 + m^2c^2}$. The pressure of the gas can be varied to change the speed of light in the medium, allowing one to differentiate between, for example, light electrons and much heavier pions at a given momentum. Additional information can be obtained from the pulse height, since this is a function of speed, and hence particle mass.

The trigger electronics is illustrated in a schematic diagram in figure 3.2. Signals from counters B1 and B2 are logically ANDed to define a beam particle. Note that signal B2 is split so that its size can be measured by an ADC. A scalar (a device that counts signals) keeps track of the number of beam particles. B1·B2 is ANDed with B3 and $\overline{\text{B4}}$ ($\overline{}$ means "NOT" — no signal in B4) to get only particles in a narrow path. The next level of the trigger is for particle identification. Because hadrons provide the main constituent in the beam, the hadron trigger is just a beam particle.

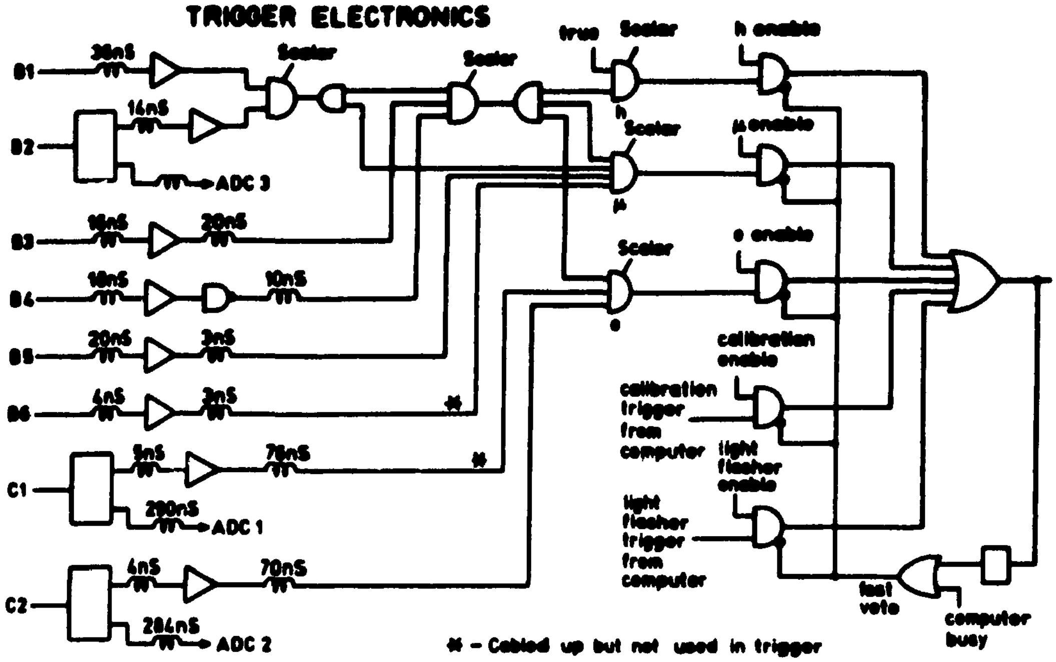

Figure 3.2 : Schematic diagram of the trigger electronics. Note that counters B6 and C1 are cabled up, but not used in the trigger.

Muons are identified by a signal from counter B5 (behind the calorimeter). Note that because there are so few muons in the beam, the constraint of counters $B3 \cdot \overline{B4}$ is removed, allowing all beam muons to be measured. Electrons are identified at the trigger level by a signal from Cerenkov counter C2. The signals from both C1 and C2 are measured by the ADC for later use in off-line analysis where more refined electron selection criteria may be employed.

Enable signals from the computer allow software selection of the type of particle to be measured. Additional triggers for the calibration systems are provided. When the computer is busy, or a trigger signal has just come through, the trigger output is inhibited by the "fast veto" to avoid overloading the readout electronics.

The output from the trigger is sent to the computer and to the readout electronics. This is the subject of the next section.

3.3 Calorimeter Readout and Electronics

The calorimeter phototube high-voltage was supplied individually for each channel by Lecroy HV4032A power supplies. Although each power supply had thirty-two channels, only twenty-four were used in each, requiring two power supplies per prototype module. These power supplies allowed remote setting of each voltage (by computer in our case) to the nearest volt with a channel-to-channel accuracy of roughly $\pm(0.1\% + 3\,\mathrm{V})$, or $\pm$ 5 V for 2000 V setting. The voltages used for the XP2081 (HAC) phototubes ranged from -1150 V to -1350 V; the voltages for the XP2972 (EMC) phototubes ranged from -1600 V to -2050 V.

As mentioned earlier, the signals from the phototubes were delayed by the use of long cables to allow the trigger electronics time to determine whether a reading should be taken. If the trigger decision was "yes", then signals were sent both to the computer and to a Lecroy 2323A programmable gate generator that enabled the ADC's just as the delayed pulses arrived from the calorimeter. The integration time for this charge measurement was determined by the gate generator, and could be programmed by the computer. The ADC's were of the Lecroy 2280 series, with four forty-eight-channel 2282B ADC's reading out all of the calorimeter. The computer that did this reading, and storage on tape, as well as on-line histogramming, was a VMEbus-based system with a Motorola 68000 microprocessor. This type of system will eventually be used for the ZEUS data acquisition, so its use in these tests is partly developmental.

The use of a programmable gate generator allowed the software to change the gate length (signal integration time) depending on the type of data it was taking, without requiring operator intervention. For example, UNO readings (with a 10 μs gate) could be interspersed with particle readings (with a 100 ns gate), using time to an advantage since particles only arrived for one second out of every thirty. As well, an output register connected to the computer gave control of the trigger over to software, with particle type selection done through the computer console, ensuring an accurate record of the type of measurement being done, and making the system "user-friendly" and less prone to errors caused by cable swapping or other hardware changes.

3.3.1 *Ground Considerations*

One problem in the electronics discovered during the one-module test, and corrected for the two- and three-module tests, was poor grounding. The signal cables were connected to the phototube bases through caps on the end of the calorimeter. The connectors were grounded to these caps and the caps were grounded to the module body by the clips holding them in place. The module was resting on the metal table that was grounded to the electrical system through its electric motors. The signal cables, however, led to a second ground — that of the electronics. If a potential difference between the two grounds arose, then a current would flow through the signal cables, changing ADC measurements. Because the relative level of the two grounds was unpredictable, the change in ADC measurements was as well. To correct this, 400 μm thick mylar sheets were inserted between modules and table, and subsequent modules had the connector grounds insulated from the module body.

3.4 Channel Equalization

As mentioned at the end of chapter two, a very useful, though not essential, aspect of calibration is the hardware equalization of channels. Having all channels giving the same output for the same input allows fast, on-line use of data without requiring any special software processing.

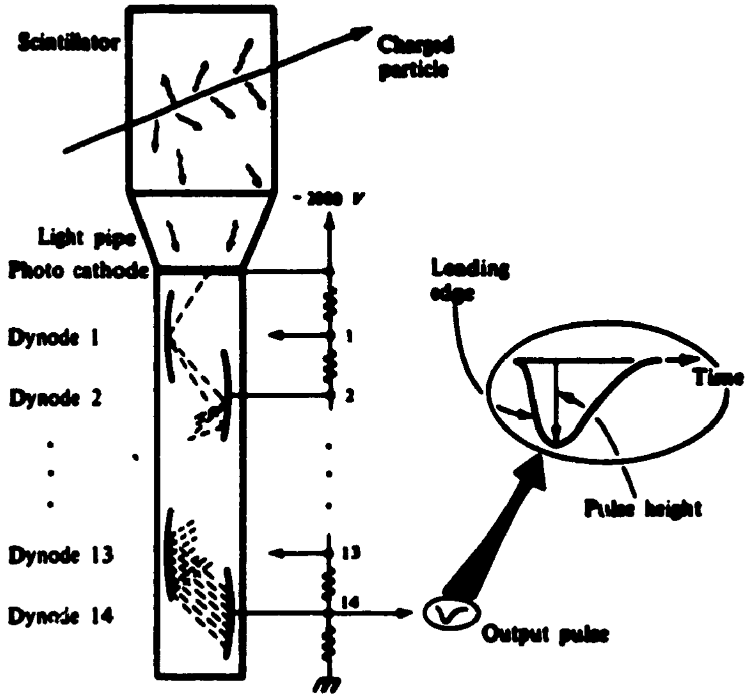

Figure 3.3 : Schematic diagram of a scintillation counter, including an illustration of the electron cascade from dynode to dynode in a phototube [2].

Before looking at techniques used for this, it is helpful to have some understanding of how a photomultiplier tube behaves, since this component is the principal unknown in calibration. As previously described, a phototube has a light-sensitive cathode (photo-cathode) which emits so-called "photo-electrons" when struck by light (see figure 3.3). This is followed by a series (ten in our case) of small metal plates, "dynodes", at increasing voltages which amplify the signal by accelerating the electrons of the previous stage, then emitting even more electrons when struck by the originals. At the end of the chain (the anode), an amplified, and measurable, signal is produced. (Note that in high-energy physics, the photo-cathode is usually held at a negative voltage and the anode is at ground voltage so that the anode can be directly coupled to the ADC. Use of an intermediate circuit — often just a simple blocking capacitor — which complicates matters and invariably introduces noise into the system is thereby avoided.)

To maintain the different voltages along the dynode series, a voltage divider chain of resistors is used, as illustrated in figure 3.4. Typically, the total resistance of the chain is of the order of 1 MΩ, so the resistors giving the voltage drop V_d in the figure are about 100 kΩ each. If a current I_c is emitted at the cathode, and if we assume that all stages give the same amplification g, then the output current will be $I_c g^{N+1}$, where $N+1$ is the number of dynodes plus the anode. In general, the gain at each stage will be proportional to the voltage across that stage raised to some power. This voltage is proportional to the total voltage V applied to the tube, so we can parameterise the total gain G as $G = \alpha V^{\beta}$. Figure 3.5 gives a plot of $\ln G$ as a function of $\ln V$ which is linear with slope β since $\ln G = \beta \ln V + \ln \alpha$. There is a great deal of variation in gain from tube to tube (not so much in the parameter β, but primarily in the parameter α), however, given a single point on the curve, one can calculate α and easily estimate a voltage to give the desired gain.

So we return to the problem of channel equalization. In most calorimeters, this task requires some external source of calibrated signal for each channel (calibrated meaning a known signal, at least relative to the other channels). In a uranium calorimeter, however, one has the background radiation giving a constant signal (the UNO signal). Furthermore, this signal will be essentially equal in all towers of the same design (that is, all EMC towers, and all HAC towers, but EMC and HAC signals will not be the same).

It is possible to measure this signal using the computer, which will calculate a mean for each channel, allowing one to estimate a new voltage for each channel that would give identical gain (assuming that one has already done a voltage scan for one tube to estimate the parameter β). Subsequent iterations of this procedure (at the new voltages) would continue to improve the estimates and then allow one to monitor

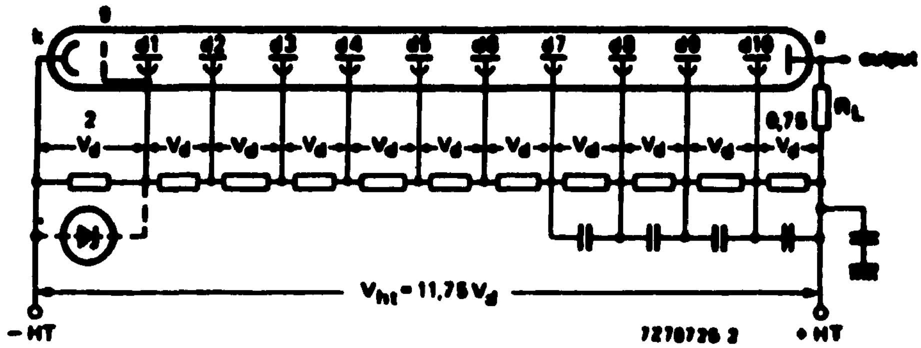

Figure 3.4 : Circuit diagram for a typical phototube base voltage divider (in particular, the XP2011, closely related to the XP2081). The cathode is denoted by k and the anode by a; $d1$–$d10$ are the dynodes. The anode is at ground voltage and the cathode is at a negative high voltage (between −1100 and −1400 V) [3].

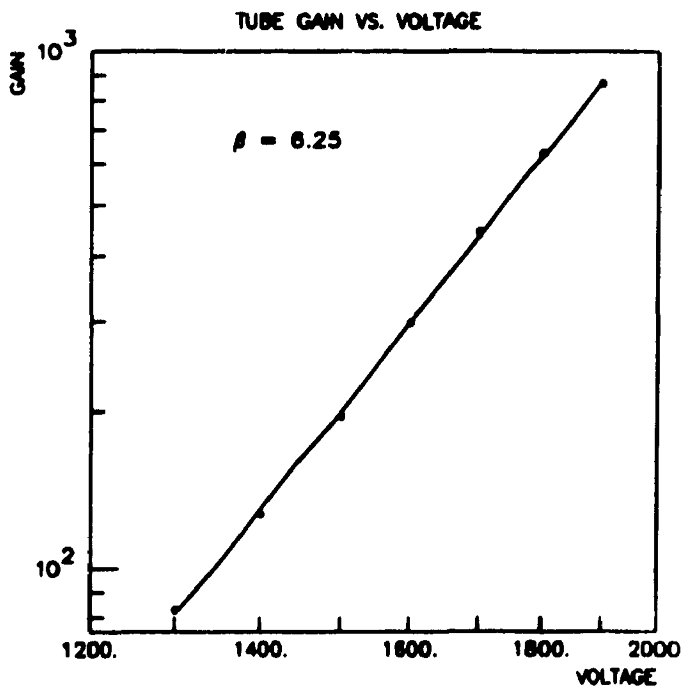

Figure 3.5 : Plot of typical phototube gain versus voltage (done as a log-log plot). The standard gain parameterisation is $G = \alpha V^{\beta}$. Note that the range of voltages used is −1300 V to −1900 V.

small changes in the tube gains.

Unfortunately, this method is very tedious to do by hand for a large number of channels. It can be done automatically by computer, but the software available at the test beam did not provide this option. An equivalent method was found that enabled one to integrate enough uranium noise to get an accurate measurement of gain and that gave an immediate response to voltage changes so that equalization could easily be done channel by channel. This method consisted simply of measuring the current flowing from the anode using a voltmeter rather than an ADC. The phototube base circuitry had a 10 kΩ resistor between the anode and ground (labelled R_L in figure 3.4). Measuring the voltage in mV on the signal cable (across this resistor) gives the current through the resistor in μA multiplied by ten. Currents of the order of micro-amps (depending on the desired gain) were used for the EMC's and of the order of tens of micro-amps for the HAC's. A factor of roughly five between EMC signal and HAC signal was estimated and later confirmed by experimental results.

Once all the tubes had their gains in the right region, it was a fairly simple matter to monitor the UNO signals with the computer system and make adjustments where appropriate.

3.5 The Tests

The calorimeter was subjected to a number of different tests including both tests of its performance (response to electrons and hadrons, resolution, etc.), and tests of different calibration systems (comparing muons, UNO, light-flasher and radio-active sources). Most of the testing (except for the energy scan) was done with 5 GeV particles.

The first step involved determining (accurately — for software purposes later on) relative calibration of all channels. This was done using UNO runs, electrons in the centre of each EMC strip and muons.

A battery of detailed electron scans followed, moving the calorimeter by small steps (as small as 0.5 cm) through the beam (selecting only electrons as previously described). A particular problem was the change in response of the calorimeter as one moved across the gap between modules. When an electron entered the WLS, it did not give the same light as it would have showering in the DU/scintillator. A further problem was response to showers centred on spacer columns — much energy was lost in the spacers with a corresponding reduction of light in the scintillator.

As modules were added, additional calibration runs with UNO, electrons and muons were done. Hadron runs were also done at the centre of each tower, though proper results were not obtained until three modules were in the beam (only with three modules were hadron showers completely contained). When all three modules were in place, detailed scans with hadrons looked for variations in response across the calorimeter face.

An energy scan with electrons, muons and hadrons was done to give behaviour as a function of energy, particularly e/h, σ/E and signal linearity. Because of the limitations of the beam, the highest particle momentum was 10 GeV/c; the rest of the scan included momenta 7, 5, 3, 2 and 1 GeV/c.

Finally, the effect of particles entering the calorimeter at an angle was investigated by rotating the modules by various amounts. The effect of this on non-uniformities in response was of particular interest (both spacer columns and WLS gaps between modules).

An on-going program of light-flasher testing was started, first using the LED's of the second distribution level as a source, and then using an external laser source. Work with the radio-active source calibration system was also done, but results from these calibration tests will not be discussed here.

References

[1] Jackson, J.D. *Classical Electrodynamics*, Wiley (New York), 1975.

[2] Frauenfelder, Hans and Ernest M. Henley, *Subatomic Physics*, Prentice-Hall, Inc. (Englewood Cliffs, N.J.), 1974.

[3] Philips Electronic Components and Materials, *Electron Tubes: Photomultiplier Tubes, Phototubes, Channel Electron Multipliers*, circa 1986.

Chapter 4 – Calorimeter Performance

4.1 Calibration

Before we can look at the results from the test beam and see how well the prototype calorimeter performs, we must be able to calibrate — relate each channel so that all give the same result for a given energy. The test-beam data provide a number of sources of constant energy appropriate for signal equalization of all channels. The three principal ones are uranium noise (UNO), muons and electrons incident in the centre of each EMC strip (other sources exist, such as constant energy hadrons, but the signal produced is too variable to provide a good calibration). Each has its advantages and disadvantages, and the idea is to combine them appropriately to get the best overall calibration possible.

The basic approach used is the same regardless of energy source, although there are significant differences in practical detail. For the set of calorimeter channels that one wishes to calibrate, one makes use of a constant energy source applied in a consistent fashion to all channels and the output signal is measured repeatedly. The mean value of these measurements for a given channel (preferably obtained by fitting a curve to the histogram) is used to compute a calibration constant that, when multiplied by the mean, gives the same result regardless of channel. The measured energy for any event i is given by

$$E_i = \sum_j a_j \left(PH_{ij} - b_j\right)$$

where b_j is the pedestal for channel j and a_j is the calibration constant. The main difficulty in determining these calibration constants lies in fitting a curve to each histogram.

4.1.1 *Uranium Noise (UNO)*

Uranium noise comes from the decay of uranium nuclei which release particles and photons carrying a varying amount of energy. A certain number of these particles will penetrate through the stainless steel cladding that surrounds each plate and deposit their energy in the scintillator giving rise to light which is detected by the phototubes. The measured signal's magnitude will be the result of a number of random processes including the probability of a nucleus decaying, the amount of energy carried by a particle, the probability of penetration through the cladding, the amount of light created by the particle, the fraction of light that reaches the phototubes, and the size of signal caused by the incident light. The fluctuations are dominated by the number of particles that get through the cladding in a 10 μs period (the length of integration time used, limited by the electronics available). Because fluctuations generally go as $1/\sqrt{N}$ (where N is the number of particles), and N is small for our setup, this factor is the most significant (especially in the EMC sections which are $\frac{1}{4}$ the area of the HAC's and have only 25 layers, compared to 80 in the HAC's). The resulting distribution is a skewed Gaussian — rising sharply on one side and then dropping off slowly on the other (see figure 4.1).

Fitting such distributions can generally be done fairly readily, especially given the software available to assist in the task. (Doing a χ^2-minimization fit is the most common approach). Unfortunately, such unusual distributions occasionally give rise to a failed fit, which can be irritating when applied to a large number of channels (each channel's fit must be inspected and re-worked if it fails). Because there is ample data available, an alternative method can be used.

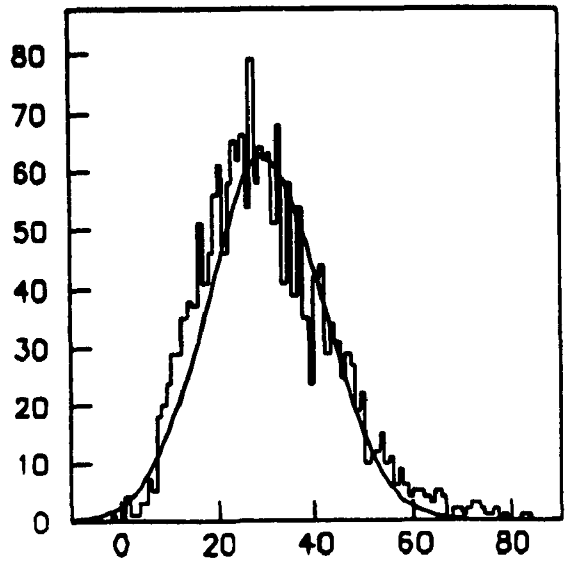

Figure 4.1 : Histogram of raw signal from uranium noise in one EMC channel. A Gaussian fit is superimposed to illustrate the asymmetry of the distribution.

Gaussian fitting routines (in particular, the subroutine HFITGA of the CERN HBOOK package) will fit any approximately Gaussian distribution quite well and with little fuss, so it is desirable to have such distributions. If one sums (or averages) enough random values from the same distribution, then the sum (or average) becomes approximately Gaussian (the central limit theorem [1] states that in the limit as the number of values goes to infinity, the sum is exactly Gaussian). In fact, a frequently used Gaussian random number generator takes the sum of only twelve numbers from a uniform distribution. Because the UNO distributions are not far from Gaussians already, it takes only from 3 to 5 numbers to get a Gaussian-looking average and a good fit (see figure 4.2).

It is important to be able to decide what a good fit is, and to determine that summing three or five numbers is sufficient. The quality of each fit is characterized by a χ^2 and a number of degrees of freedom ($\chi^2 = \sum_i \frac{(f(x_i)-y_i)^2}{\sigma_i^2}$, where $f(x_i)$ is the fitted

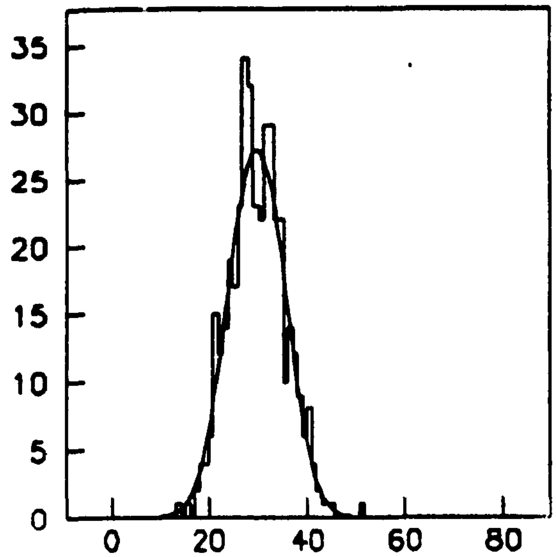

Figure 4.2 : Histogram of UNO signal in same EMC channel as figure 4.1, but averaging five events at a time.

function, y_i is the data value at x_i and σ_i is the error on y_i). If the fit is good, then the χ^2's resulting from a number of fits should be distributed according to a well-known χ^2 distribution. However it is difficult to tell by eye if the obtained distribution is reasonable or not. An excellent method for overcoming this is to determine for each χ^2 (and number of degrees of freedom) the fraction of the χ^2-distribution greater than the one obtained (a kind of probability) — this can be done using the CERN function PROB. For a good fit, the distribution should be uniform and so is easily verified by eye. This method is quite sensitive to poor fits, and so is a good test.

To arrive at the number of measurements to sum, one merely starts at single events, then increases the number until the probability-of-χ^2 distribution is approximately uniform (see figure 4.3). The final number of events summed was 5 events for the EMC channels and 3 events for the HAC channels.

No matter how good the fitting, the quality of results is always limited by the

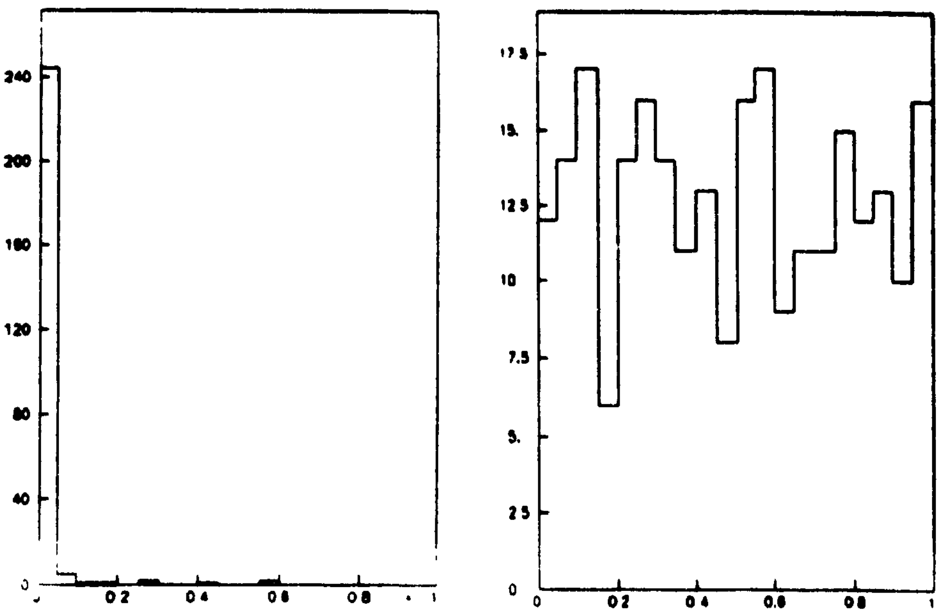

(a) (b)

Figure 4.3 : Distribution of "χ^2 probability" (fraction of χ^2-distribution greater than given χ^2) for a Gaussian fit to (a) raw UNO data in EMC's (see figure 4.1), and (b) averages of five events at a time (see figure 4.2). Notice that figure (a) comes from large χ^2's, but figure (b) comes from good fits.

original data available. Although the HAC sections give a good UNO signal, the EMC sections have a signal sufficiently small that fluctuations in the electronics hardware become quite significant. The pedestal (electronics output with no input) is of the order of 1000 ADC counts for a 10 μs integration time, whereas the UNO signal is only around 30 counts in the EMC sections (HAC's have a signal close to 200 counts). Even a small percentage variation in such a pedestal will strongly affect the EMC measurements (for example, a 0.2% variation in pedestal would give a 6% variation in the measurement).

4.1.2 *Muons*

We now look at the signal provided by 5 GeV beam muons traversing the calorimeter. These muons deposit a significant fraction of their energy in the calorimeter through ionization, but escape out the back with a few GeV of energy. Though we are not dealing with perfectly minimum-ionizing particles, the ionization losses over the energy range in question are still nearly constant (see figure 1.7 in chapter 1). This provides a very important means of relating the signals in the quite different EMC and HAC sections. The strength of signal depends only on the thickness of scintillator traversed for a given section, so it becomes a simple matter to compare EMC signal (from 25 scintillator plates) and HAC signal (from 80 plates).

There is an added level of complexity that comes from wanting a simple fit to these distributions. The ionization energy deposited fluctuates according to the Landau distribution (see histogram of the raw data in figure 4.4), however there is a long, high-energy tail that arises principally from bremsstrahlung [2] (giving a photon that showers electromagnetically). We can perform our trick of summing signals to achieve an approximately Gaussian shape, but these few, high-energy events tend to give a skewed shape even when ten events are used (see figure 4.5). A simple way around this is to throw out, for every set of ten events, the highest energy ones, giving a better Gaussian shape (see figure 4.6).

We can estimate the number of events that should be thrown out to eliminate bremsstrahlung-type signals. The ionization energy loss of a muon is given by [3]

$$\begin{aligned}\left(\frac{dE}{dx}\right)_{ion} &= 4\pi\frac{N_A Z}{A}r_e^2 m_e c^2\frac{1}{\beta^2}\left[\ln\left(\frac{2m_e c^2\gamma^2\beta^2}{I}\right)-\beta^2-\frac{\delta}{2}-\frac{C}{Z_{med}}\right]\{1+\nu\} \\ &\simeq 4\pi\frac{N_A Z}{A}r_e^2 m_e c^2\frac{1}{\beta^2}\left[\ln\left(\frac{2m_e c^2}{I}\right)-\beta^2+2\ln\left(\frac{p}{m_\mu c}\right)\right]\end{aligned}$$

where N_A = Avogadro's number,

Z = atomic number of the medium,

A = atomic weight,

r_e = classical electron radius,

m_e = electron mass,

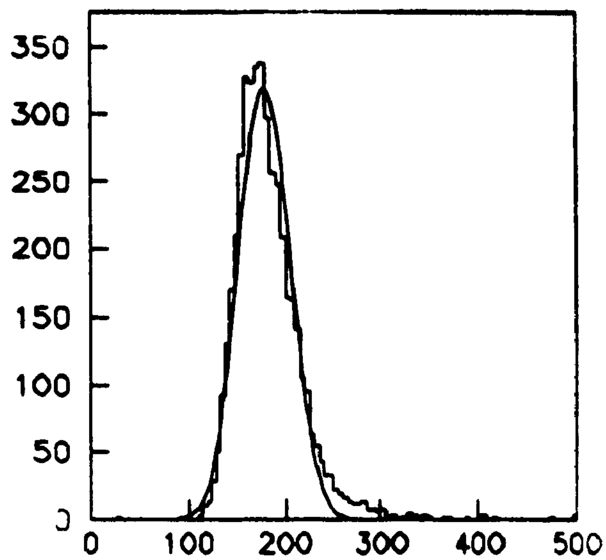

Figure 4.4 : Histogram of raw muon events for one HAC channel.

m_μ = muon mass,

β = velocity of muon,

p = momentum of muon,

I = parameter characterizing binding of electrons.

Other parameters give corrections that we will ignore.

The energy loss due to bremsstrahlung is given by [4]

$$\left(\frac{dE}{dx}\right)_{brem} = 4\frac{N_A Z^2}{A}\alpha\left(\frac{m_e}{m_\mu}\right)^2 r_e^2 E\left[\ln\left(\frac{2E}{m_\mu c^2}\frac{\hbar}{m_\mu cR}\right) - \frac{1}{3}\right]$$

where R is the nuclear radius.

If we assume that both ionization and bremsstrahlung energy losses are constant (since the muon energy does not change too dramatically through the calorimeter), then the energy loss from each through a length L of calorimeter is $(dE/dx)_{ion}\, L$ and $(dE/dx)_{brem}\, L$. However, bremsstrahlung occurs in only a small number of events, so $(dE/dx)_{brem}\, L$ is approximately equal to the probability of it occurring times the

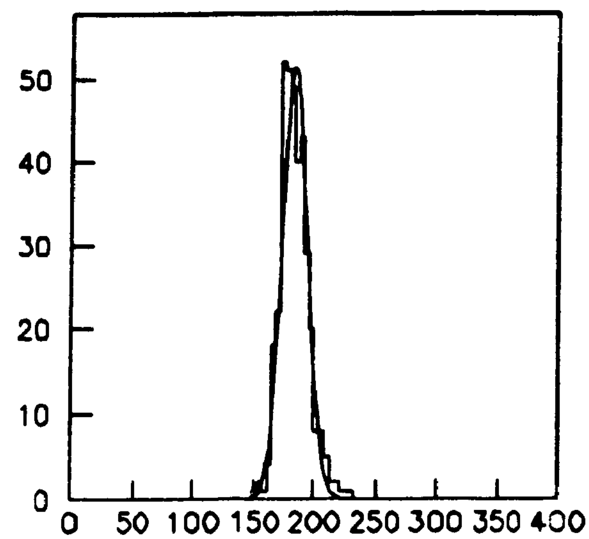

Figure 4.5 : Histogram of averages of ten muon events at a time for the same HAC channel as in figure 4.4.

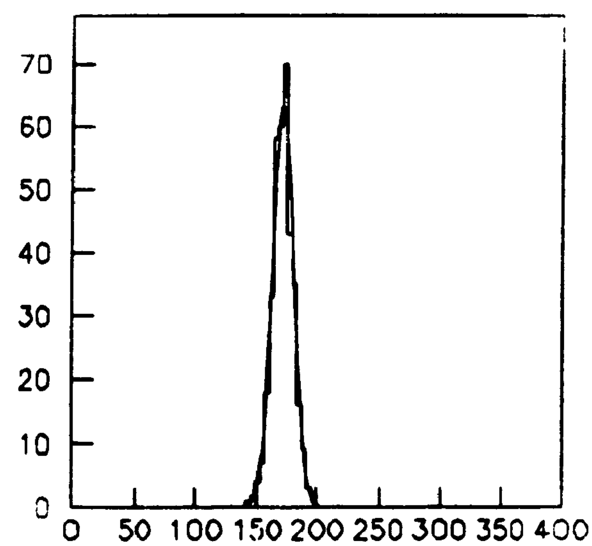

Figure 4.6 : Histogram of averages of lowest eight muon events from samples of ten for the same HAC channel as in figure 4.4. Throwing away the highest energy events eliminates events with bremsstrahlung contributions.

actual energy loss when it happens (assuming a fixed energy loss). We are only interested in energy losses that are of the order of the ionization loss, so we can approximate the probability P of such a bremsstrahlung-type event occurring as

$$
\begin{aligned}
P &= \frac{(dE/dx)_{brem}\, L}{(dE/dx)_{ion}\, L} = \frac{(dE/dx)_{brem}}{(dE/dx)_{ion}} \\
&\simeq \frac{Z}{\pi}\alpha\left(\frac{m_e}{m_\mu}\right)^2 \frac{E}{m_e c^2} \frac{\left[\ln\left(\frac{2E}{m_\mu c^2}\frac{\hbar}{m_\mu c R}\right) - \frac{1}{3}\right]}{\left[\ln\left(\frac{2m_e c^2}{I}\right) - \beta^2 + 2\ln\left(\frac{p}{m_\mu c}\right)\right]} \\
&= \frac{92}{\pi}\frac{1}{137}\left(\frac{0.511\ \text{MeV}}{106\ \text{MeV}}\right)^2 \frac{5000\ \text{MeV}}{0.511\ \text{MeV}} \frac{\left[\ln\left(\frac{2\cdot 5000\ \text{MeV}}{106\ \text{MeV}}\frac{197\ \text{MeV}\cdot\text{fm}}{106\ \text{MeV}\cdot 6\ \text{fm}}\right) - \frac{1}{3}\right]}{\left[\ln\left(\frac{2\cdot 511\times 10^3\ \text{eV}}{16(92)^{0.9}\ \text{eV}}\right) - 1^2 + 2\ln\left(\frac{5000\ \text{MeV}/c}{106\ \text{MeV}/c}\right)\right]} \\
&= 0.01079
\end{aligned}
$$

(assuming the medium to be pure uranium-238).

If we repeat this Bernoulli process — one that has only two possible outcomes — n times (that is, we take n events that either have or do not have bremsstrahlung), then the probability of r events with bremsstrahlung is given by the binomial distribution

$$
\frac{n!}{r!\,(n-r)!}P^r(1-P)^{n-r}
$$

(where P is the probability of bremsstrahlung for one event). If we have $n = 10$, then the probability of zero bremsstrahlung events is 0.8972, the probability of one such event is 0.0979, the probability of two is 0.0048, and the probability of three is 0.0001 (the probability of more becomes negligible). Thus we see that throwing away the two highest energy events of every ten will essentially eliminate the contribution from bremsstrahlung and give a good Gaussian fit (which is how figure 4.6 was obtained).

4.1.3 *Electrons*

An ideal type of calibration is with the particles for which the calibration is to be used. If we inject an unchanging beam of electrons into the centre of each EMC

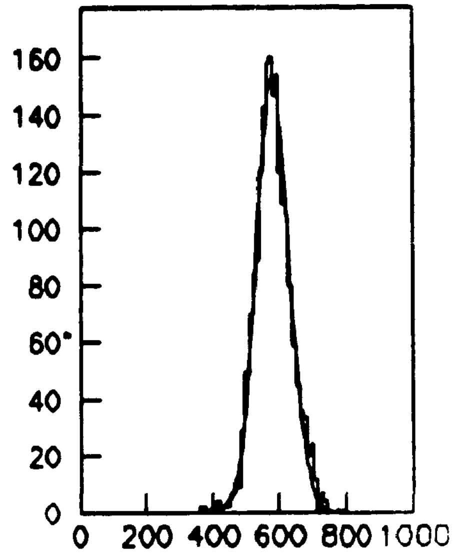

Figure 4.7 : Histogram and fit of a 5 GeV electron signal from an EMC channel.

strip, then our calibration should be perfectly suited to electrons at 5 GeV and, if we assume a well-built calorimeter, at all energies. Furthermore, the distribution of signals coming from one channel is well fit by a Gaussian curve, so we need not process the data any further (see figure 4.7).

Unfortunately a 5 GeV electron shower does not penetrate into the HAC sections and so is no help in calibrating these channels. One could use a hadron shower, but these are much larger than electron showers and the energy is spread over many channels giving fairly small signal in any one channel. Moreover, hadron showers involve very significant fluctuations so the distributions are more complicated than those for electron showers.

There are some drawbacks to the use of an electron beam. We want a constant source of energy, identical for all channels calibrated — if there is a significant length of time between the calibration runs for different channels (in our case, modules were installed and calibrated one at a time, over a period of days), then the beam has to be carefully set to give the same energy of electron. This should be well controlled by the beam-line magnets. As well, the beam positioning should be fairly well reproduced, since some of the shower can leak out of the strip in question and give a slightly varying result depending on the fraction of leakage. The Molière radius R_M for uranium is 1.02 cm [5], and a cylinder of radius $2R_M \simeq 2$ cm will contain an electromagnetic shower [6], so the 5 cm wide EMC strips will contain essentially all energy, and small variations in positioning should matter little.

4.1.4 *Putting Them All Together*

We now have three ways of obtaining calibration constants, and we must combine them in some way to obtain a final set of constants for all channels.

As has already been mentioned, the UNO signal for the EMC channels is quite small and varies significantly when compared to the electron signal ($\sim 4\%$). The UNO signal from HAC's is much better and so can be used for calibration. Thus, using electron runs for EMC's and UNO for HAC's we can calibrate these two different types of sections separately. To relate EMC signals to HAC signals, we still have the muon data. Although this data may fluctuate on a channel-by-channel basis, it should give good results when averaged over all EMC channels and over all HAC channels, allowing us to find a constant relating the two types of sections.

4.2 Event Analysis

Equipped with a set of calibration constants, it would seem that event analysis would be very simple: add up the calibrated signal in all channels to get the total energy for an event (a single particle). This is somewhat naïve however and ignores a number of important things. First of all, the light created in the scintillator is "seen" by two phototubes — one on either side of the tower. The original energy is not the sum of the two signals, but is some more complicated combination of the two that must account for the attenuation in the optics. In addition, the fact that the signal is measured on both sides of the tower after attenuation allows us to estimate the position of the original energy deposit by comparing the relative magnitudes of the two signals. As well as obtaining a horizontal position measurement, we can also obtain a vertical position measurement by exploiting the 5-cm segmentation of the EMC sections.

A final consideration when dealing with the analysis of each event is the noise contributed to the signal by both the uranium noise and the electronics. If we simply add up the signal in all channels, we add in a significant fluctuation arising mostly from the uranium noise — the error on each channel is relatively small, but when all channels are added together it becomes non-negligible. To avoid this, we consider only those channels that have a signal above the usual noise level. However, if this threshold is chosen to be too high, we ignore some of the real energy signal.

4.2.1 *Electron Analysis*

To get the proper signal for an electron shower, we must try to compensate for the attenuation of light in the optics (since this will depend in some way on the location of the shower). An approximation that works well is to assume that the shower is localized at one point, and we are directly reading out the signal on either side of the scintillator. The light reaching the edge of the scintillator will have magnitude PH_0e^{-d/L_0} where PH_0 is the original signal (or pulse height) before attenuation, d is the distance travelled by the light and L_0 is the attenuation length. If we take $2L$ to be the length of the scintillator and x to be the position of light creation measured from the centre of the scintillator, then the pulse height measured on each side of the scintillator (where x is positive on side 2) is given by

$$PH_1 = PH_0 e^{-(L+x)/L_0}$$

$$PH_2 = PH_0 e^{-(L-x)/L_0}$$

If we take the square root of the product of the signal on each side, we get

$$\begin{aligned}\sqrt{PH_1 \cdot PH_2} &= \sqrt{PH_0^2 \cdot e^{-(L+x+L-x)/L_0}} \\ &= PH_0 e^{-L/L_0} \\ \Rightarrow PH_0 &= \sqrt{PH_1 \cdot PH_2}\, e^{L/L_0}\end{aligned}$$

which gives the original pulse independently of the position x. Furthermore, we can get x by taking the natural logarithm of the ratio of the two signals

$$\begin{aligned}\ln\left(\frac{PH_1}{PH_2}\right) &= \frac{-2x}{L_0} \\ \Rightarrow x &= \frac{-L_0}{2} \ln\left(\frac{PH_1}{PH_2}\right)\end{aligned}$$

Both of these require a knowledge of the attenuation length of the scintillator. This can be calculated in a fairly straightforward way by using the previous formula. The test-beam data includes horizontal electron scans across the face of the calorimeter, so we can get a plot of $\ln(PH_1/PH_2)$ versus x. Figure 4.8 gives such a plot, and we see that the first five points, over a range of 7 cm (from the centre towards the edge of the module), are linear with position. Making this type of fit to a number of horizontal scans leads to an average attenuation length of (53.4 ± 1.0) cm. Further fits suggest that this linear fit is good out to 7.6 cm from the centre of each module. Recall that the scintillator tiles extend out to ~ 10 cm from the centre and so in this region within 3 Molière radii of the edge things start to break down.

The ratio of signals towards the edge of the module is increased by a jump in signal on one side. When an electromagnetic shower is close to the WLS, it deposits an exaggerated amount of energy in the WLS, giving an excessively large signal in

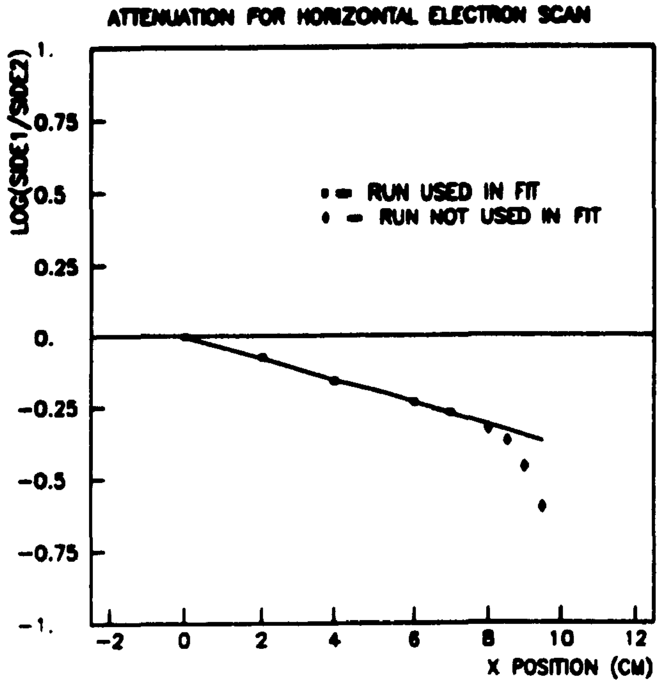

Figure 4.8 : A straight line fit to the first five points of a $\ln(PH_1/PH_2)$ versus x plot, where PH_1 and PH_2 are the pulse heights on either side of an EMC strip and x is the horizontal position of the beam (zero is chosen to be the centre of the strip).

the channel on that side of the module. We can correct for this added signal when determining position through the use of a quadratic correction added to the linear fit beyond 7.6 cm (with constraints requiring continuity in both the function and its first derivative) as illustrated in figure 4.9.

When calculating signal, however, we must remember that the signal on one side of the calorimeter is boosted. So we get the original pulse height by ignoring that side and using only the other signal with an explicit correction for attenuation (given the horizontal position of the shower). This method gives a good estimate of the shower in the scintillator but that is only part of the incident particle's energy: the rest goes down the crack. This loss can be calibrated out in the mean but leads to large fluctuations.

Often the signal from a shower will be split between two or more EMC strips

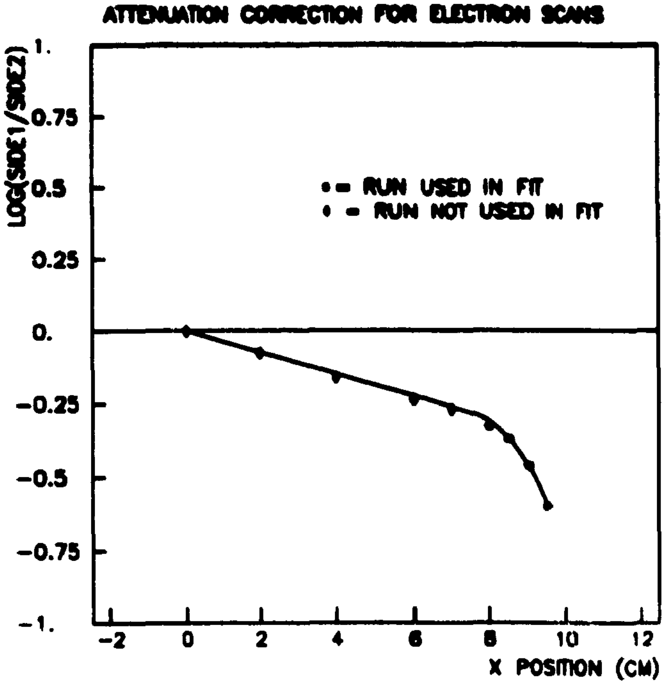

Figure 4.9 : Fit of straight line plus correction to same plot as in figure 4.8, but including the points beyond 7.6 cm.

(and possibly some HAC sections). To get the total energy, we simply add up all contributions. To get the position, we can take a weighted mean of the results from all sections, using the signal in a section as the weight. This can be done in both horizontal and vertical dimensions, although with the vertical dimension the position for a particular section cannot be estimated and so is taken to be the position of the centre.

The final aspect of electron event analysis is the choice of thresholds to eliminate unnecessary noise contributions. With a 100 ns gate, the noise in the EMC strips has an overall mean of 0.11 ADC counts and an overall standard deviation of 1.13 counts. In the HAC sections, it has a mean of 0.16 counts and a standard deviation of 1.75 counts. For electron showers, cuts of 5 counts (for EMC's) and 10 counts (for HAC's) were chosen. These correspond to energies of 35 MeV and 70 MeV.

4.2.2 *Hadron Analysis*

The analysis of hadron events is quite similar to that of electron events, but with a few simplifications. These simplifications arise from the fact that hadron showers develop much more slowly (that is, the energy deposit is spread over a greater depth of calorimeter) and are much wider in the transverse dimensions than electron showers. This means that the problem at WLS gaps between modules essentially disappears, since one no longer has most of the shower energy in the region of the WLS. Thus the energy calculation for a tower simply makes use of the square root of the product of the signals from the two sides. The horizontal position comes from the logarithm of the ratio of signals as before, assuming a strictly linear behaviour with position (no correction for the edges of the module). The vertical position measurement is exactly the same as before, with all sections contributing according to their signal.

The spreading out of the energy distribution means that we must be somewhat more careful about the choice of noise thresholds, since choosing high levels could cause us to ignore significant fractions of the energy. Given the noise levels in the different types of sections, thresholds of 3 ADC counts (for EMC's) and 5 ADC counts (for HAC's) were chosen (these correspond to 21 MeV and 35 MeV respectively). The fraction of noise events greater than threshold is 3.0% for EMC's and 2.1% for HAC's. The selection criteria for a section include a requirement that both sides of the section have signal greater than threshold. This means that if the two signals are completely uncorrelated, then the actual acceptance of noise events would be 0.090% for EMC's and 0.044% for HAC's. The real situation will have the two signals partly correlated, particularly so since the light comes from the same energy deposit in the scintillator, so we will get somewhere between 0.04% and 3.0% acceptance of noise events. These are small enough that noise will not contribute significantly to the signal.

4.3 Performance as a Function of Energy

It is now that we turn to the interesting results that answer that all-important question: "How well does the calorimeter measure energy?". Figure 4.10 shows histograms of the signal for six different energies between 1 and 10 GeV. Tables 4.1 and 4.2 give $(\sigma_E/E) \cdot \sqrt{E}$ for the six energies and the corresponding plots are found in figure 4.11. Straight lines are fit to these plots at $(\sigma_E/E) \cdot \sqrt{E} = 20.2\%$ for electrons and $(\sigma_E/E) \cdot \sqrt{E} = 37.4\%$ for hadrons. The linearity of the signal in shown in figures 4.12 and 4.13.

Energy	$(\sigma_E/E) \cdot \sqrt{E}$
1.0 GeV	20.31%
2.0 GeV	19.39%
3.0 GeV	20.05%
5.0 GeV	20.26%
7.0 GeV	21.14%
10.0 GeV	20.64%

Table 4.1 : Table of energy resolutions ($(\sigma_E/E) \cdot \sqrt{E}$) for electrons at six energies between 1 and 10 GeV.

Energy	$(\sigma_E/E) \cdot \sqrt{E}$
1.0 GeV	34.21%
2.0 GeV	37.05%
3.0 GeV	37.59%
5.0 GeV	38.79%
7.0 GeV	37.35%
10.0 GeV	36.79%

Table 4.2 : Table of energy resolutions ($(\sigma_E/E) \cdot \sqrt{E}$) for hadrons at six energies between 1 and 10 GeV.

It is worth noting that the hadron data includes a significant fraction of electrons, and the electron data contains hadron events (particularly at 7 and 10 GeV). The electrons in the hadron data tend to improve the apparent resolution, while the

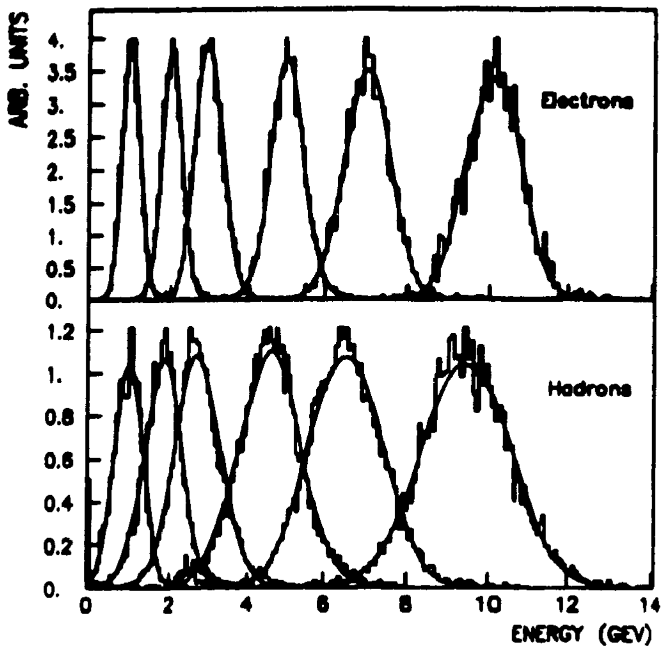

Figure 4.10 : Histograms of the signal for six energies of electrons (top) and hadrons (bottom). The hadron signal is not corrected for shower leakage.

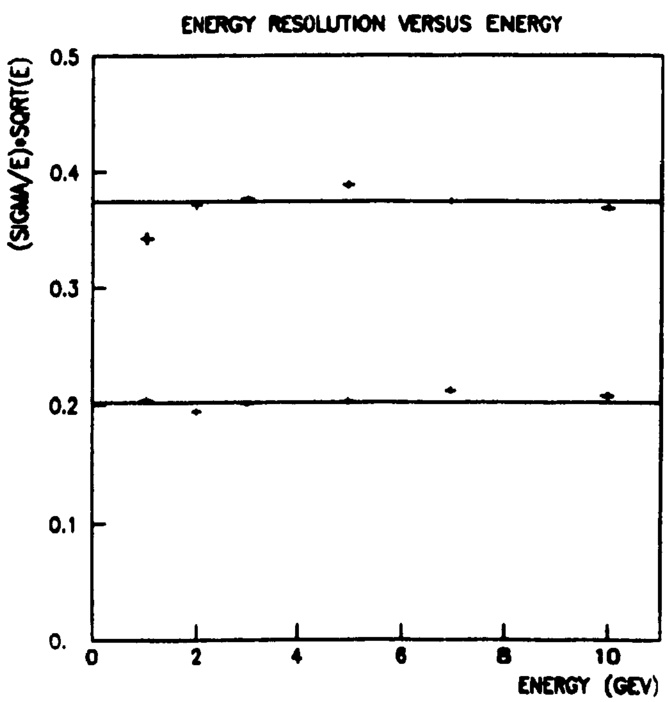

Figure 4.11 : Plot of $(\sigma_E/E)\cdot\sqrt{E}$ as a function of energy, for electrons (around 0.2) and hadrons (around 0.37).

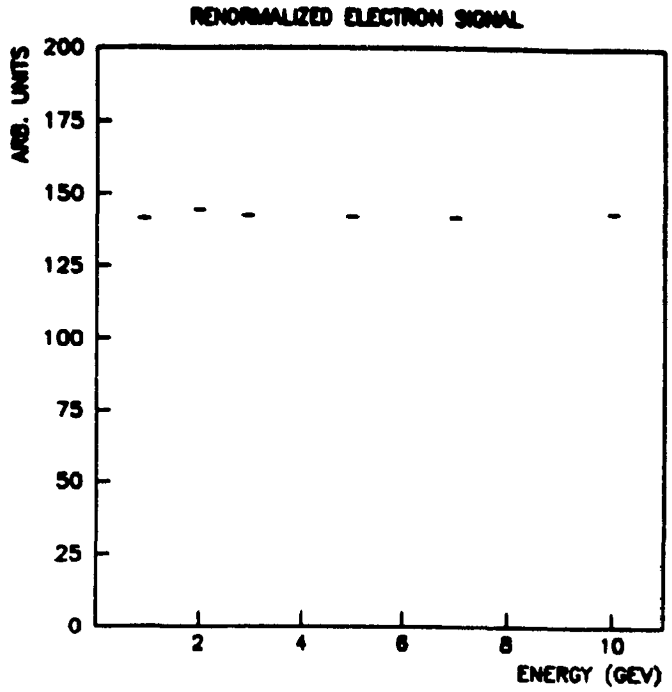

Figure 4.12 : Plot of signal/energy as a function of energy for electrons.

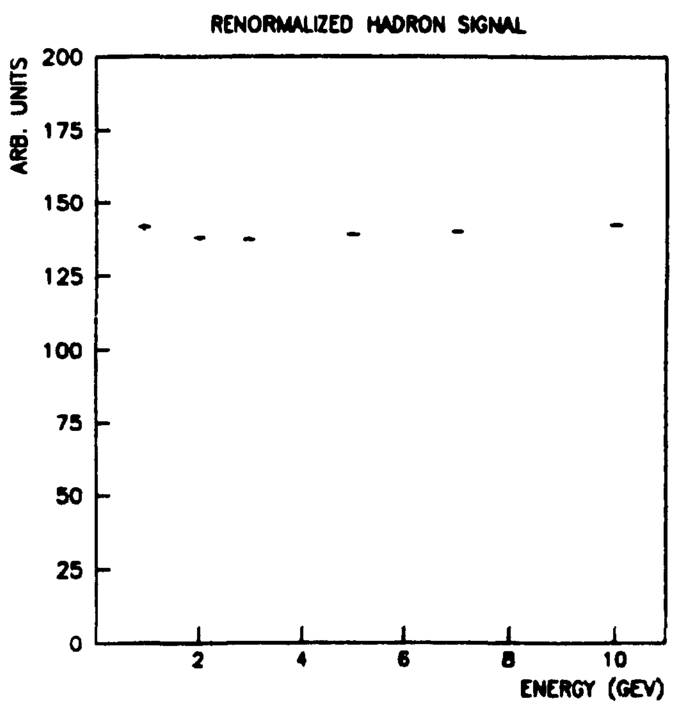

Figure 4.13 : Plot of signal/energy as a function of energy for hadrons.

hadrons in electron data worsen the result, so it is important to be able to remove such impurities from the sample. Figures 4.14 and 4.15 give histograms of the signal from the second Cerenkov counter which was not used in the trigger (see the trigger circuit diagram in figure 3.2). The first histogram shows a sharp peak at the low end (the hadrons), but also a long tail at the high end — electron events. The second histogram contains mostly electrons (the high-signal events), but also a large number of hadrons (the peak at the low end of the histogram). The contamination of the hadron beam comes from not using the Cerenkov counters in the trigger. The contamination of the electron beam at high energies probably arises from not adjusting the Cerenkov counter pressure to compensate for higher velocity hadrons. Fortunately, the unused counter did allow for off-line differentiation of events in this analysis, giving more accurate results.

4.3.1 *e/h Ratio*

As was discussed in chapter 1, we want to have the ratio of electron signal to hadron signal (e/h) as close to one as possible to achieve the best hadron energy resolution. Unfortunately there are a few complications involved in comparing electron and hadron signal which arise from the difference in shower shape and size.

The principal problem comes from the fact that some appreciable fraction of hadron energy will leak out the sides of the prototype calorimeter even when the hadron beam is at the middle. In our case, the beam entered the calorimeter in the centre of the second tower of the second module — that is, 30 cm from three sides of the calorimeter, and 50 cm from the fourth side. This leads to an energy leakage of the order of 5% (ignoring leakage out the back of the calorimeter).

To get a good estimate, we can make use of a transverse energy parameterisation

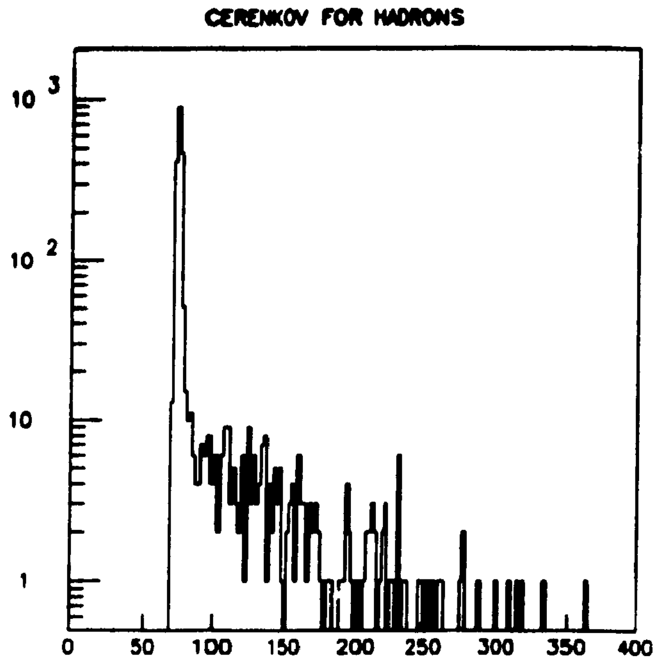

Figure 4.14 : Histogram of *he 1 GeV hadron signal from the Cerenkov counter not used in the trigger. Note the long, high-signal tail indicating the presence of electrons.

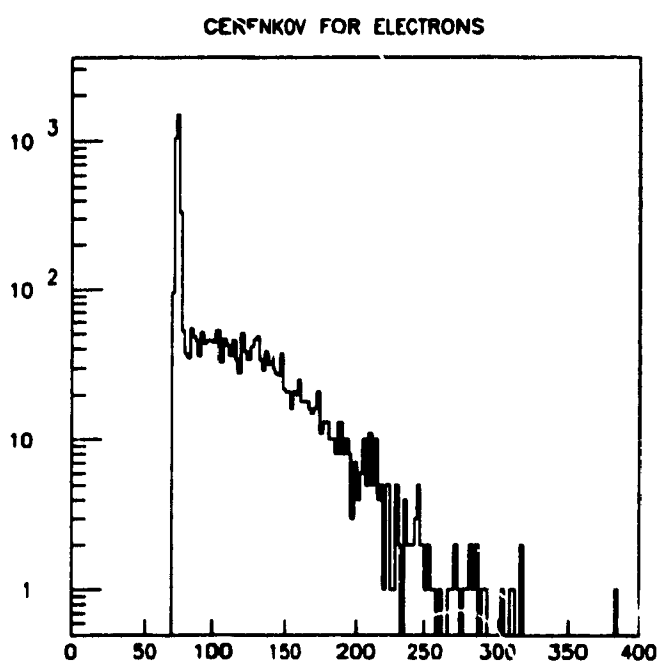

Figure 4.15 : Histogram of the 10 GeV electron signal from the Cerenkov counter not used in the trigger. Note the low-signal peak indicating the presence of hadrons.

given in [7]

$$\frac{dE}{dy} = a_1 e^{-|y|/b_1} + a_2 e^{-|y|/b_2}$$

For a 30 GeV antiproton in the iron/scintillator calorimeter of the IHEP-IISN-LAPP group, these parameters have values $a_1/a_2 \simeq 2$, $b_1 \simeq 2.2$ cm and $b_2 \simeq 7$ cm. By looking at the signal in each tower of the calorimeter, we can get some transverse energy deposition information to which we can make a fit. Unfortunately, we do not have the segmentation required to see the negative exponential of mean length 2.2 cm, so we must fix this parameter and a_1/a_2. However, this portion is essentially contained in one tower (furthermore, variations in these parameters do not give large changes in the final result). When doing a fit, it is important to remember two things. The first is the fact that the signal from each tower is an integration of the dE/dr curve over some region. The second is that noise contributions are not negligible when we remove our threshold cuts. An estimation of the noise in each tower can be obtained from muon runs by looking in an unaffected region of the calorimeter.

Table 4.3 and figure 4.16 give the estimates of leakage out of the calorimeter, which vary from about 2% at 1 GeV to 6% at 5 GeV and greater.

Energy	Leakage
1.0 GeV	$(2.05 \pm 0.31)\%$
2.0 GeV	$(4.47 \pm 0.22)\%$
3.0 GeV	$(5.50 \pm 0.15)\%$
5.0 GeV	$(5.94 \pm 0.12)\%$
7.0 GeV	$(5.91 \pm 0.11)\%$
10.0 GeV	$(5.70 \pm 0.09)\%$

Table 4.3 : Percentage leakage out of calorimeter for hadron showers at six energies between 1 and 10 GeV.

A further problem in comparing electron and hadron signals involves the use of thresholds. These cuts can remove some significant signal (along with the noise

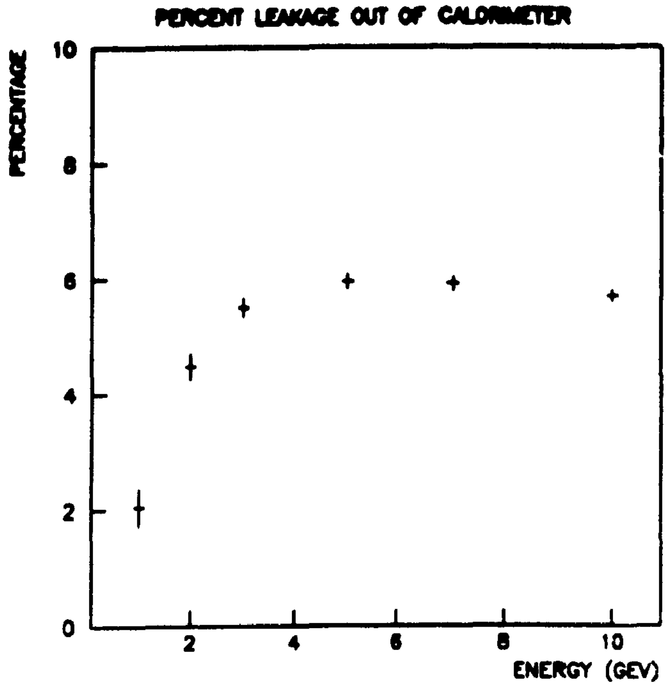

Figure 4.16 : Plot of mean leakage out of calorimeter for hadron showers as a function of energy.

that they are meant to remove). This is much more significant for hadrons than for electrons since energy is spread out to many more sections. A Monte Carlo simulation that uses a fixed transverse energy distribution and a variable longitudinal one (taking in to account fluctuations from shower to shower) suggests that the effect of these cuts may be significant, but the results are not reliable enough to provide appropriate numbers. To avoid such energy losses in the real data, cuts were removed for both electron and hadron measurements. This means that noise is added in, but is a constant since all towers will contribute in both cases. It turns out that the change in e/h is only slight.

The final results for e/h are given in table 4.4 and figure 4.17. The curve in the figure is a simple parameterisation $a_1 \ln(E/a_2) + a_3$ (where a_1, a_2 and a_3 are parameters) intended only to guide the eye. This curve is quite similar in shape to one given in reference [6] that shows how e/h drops rapidly below 2 GeV (see figure

Energy	e/h
1.0 GeV	1.013 ± 0.006
2.0 GeV	1.038 ± 0.004
3.0 GeV	1.032 ± 0.003
5.0 GeV	1.018 ± 0.002
7.0 GeV	1.007 ± 0.002
10.0 GeV	1.002 ± 0.002

Table 4.4 : Electron to hadron signal ratios at six energies between 1 and 10 GeV. The leakage of hadron showers out of the calorimeter is accounted for.

4.18). It seems that the high-energy approach to the ideal value of one is very good.

4.3.2 *Position Resolution*

For the moment we look only at the statistical errors in position measurements — we defer to the next section a glimpse of the systematic errors for 5 GeV particles. Figures 4.19 and 4.20 give the resolution in the horizontal dimension as a function of energy for electrons and for hadrons. For both we see an improvement with increasing energy and at 10 GeV the error is down to ~ 2 cm (with hadrons giving only a slightly worse resolution than electrons).

Figures 4.21 and 4.22 give the statistical errors in vertical position measurement (which comes simply from a weighted mean of the positions of tower centres). For electrons this resolution is ~ 1 cm, whereas for hadrons it is nearer 2 or 3 cm. Both cases show only a gradual improvement with energy.

4.4 Looking for Imperfections — Scans Across Towers

4.4.1 *The Gap Problem and the Spacer Problem*

As mentioned earlier, particles that enter into the WLS in the gap between modules cause an exaggerated signal in the phototube on one side of the tower. To eliminate this, our analysis looks only at the other phototube (making a correction for light

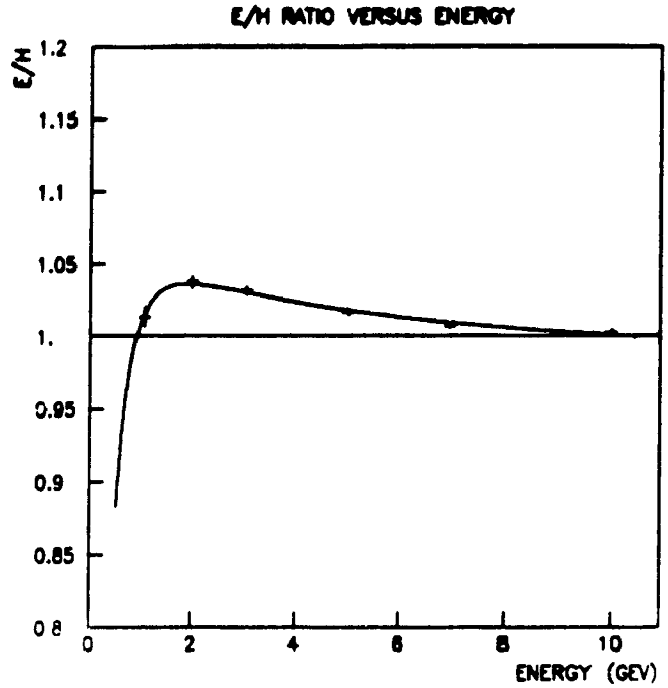

Figure 4.17 : Plot of e/h (corrected for hadron shower leakage) as a function of energy. The curve is a $a_1 \ln(E/a_2) + a_3$ parameterisation, intended only to guide the eye.

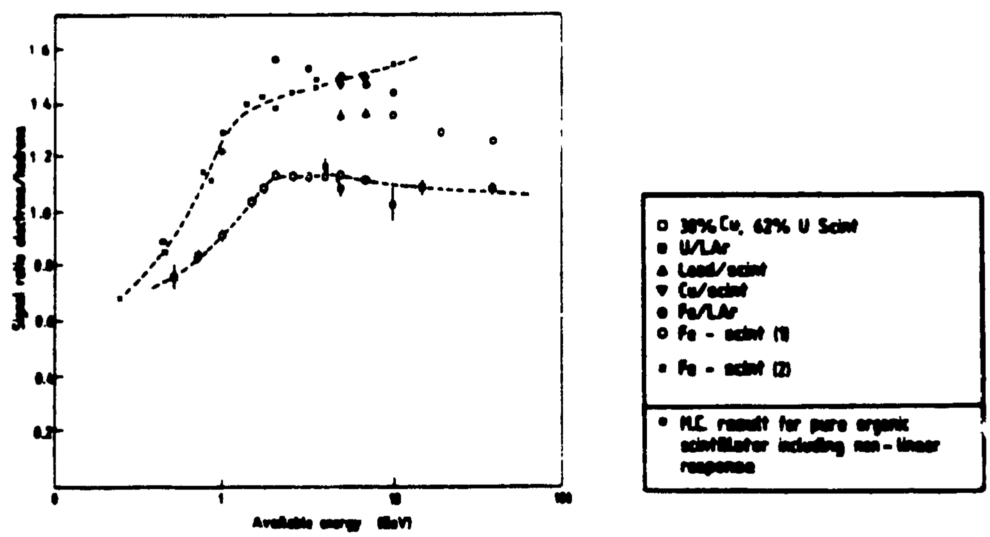

Figure 4.18 : The e/h ratio as a function of energy for various calorimeter configurations [6].

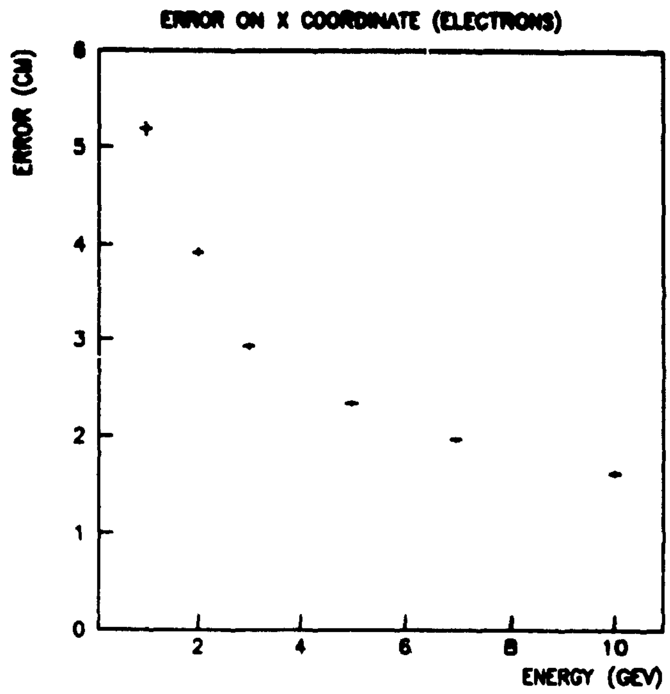

Figure 4.19 : Horizontal position resolution as a function of energy for electrons.

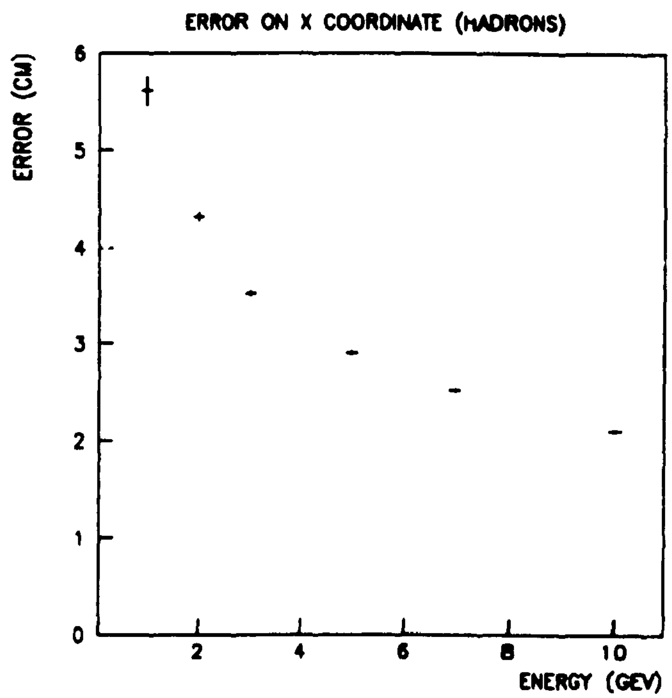

Figure 4.20 : Horizontal position resolution as a function of energy for hadrons.

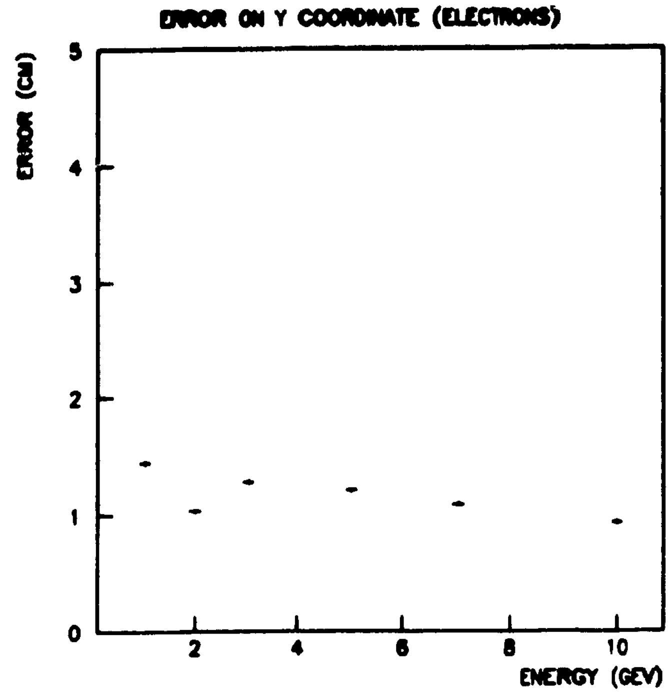

Figure 4.21 : Vertical position resolution as a function of energy for electrons.

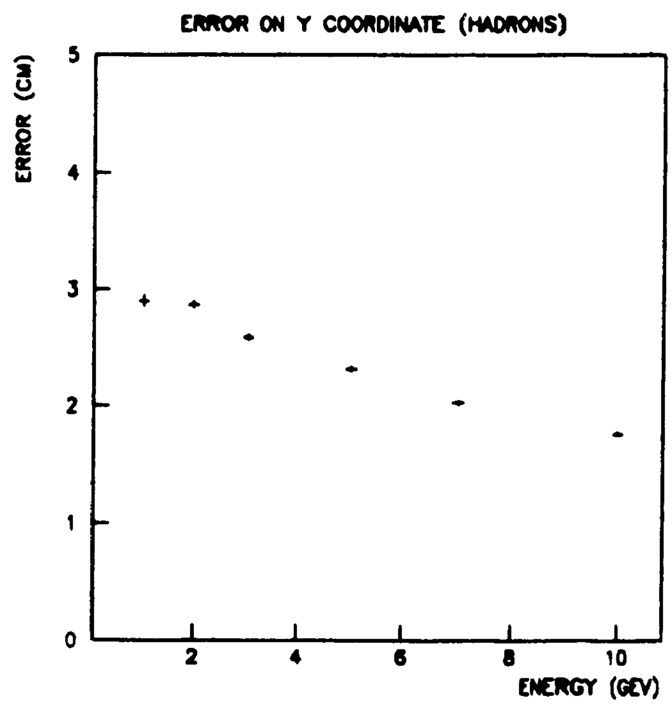

Figure 4.22 : Vertical position resolution as a function of energy for hadrons.

attenuation). Unfortunately, we do not see some of the energy — that which is lost in the WLS — so we still get some change in signal (though less than without special treatment).

Figures 4.23 and 4.24 illustrate this problem. The first gives the total signal measured as a function of position of the 5 GeV electron beam, the second gives the width of the signal distribution, again as a function of horizontal position. In both plots we see a sudden change in the region of $x = 33.6$ cm, the location of the WLS (between modules). The signal drops by $\sim 17\%$ (compared with an increase of 53% when all tubes are included), and the resolution goes from approximately 8.6% to 23.5%.

With 5 GeV hadrons, this problem is not as marked. We see this in figures 4.25 and 4.26, where no obvious change in total signal is apparent at $x = 33.6$ cm or $x = 53.6$ cm. However, the width of the signal distribution jumps from $\sim 16\%$ to $\sim 25\%$.

There is another non-uniformity in the calorimeter, and that is the presence of 5 mm $\times$ 6 mm tungsten-carbide spacers that keep the DU plates carefully separated and prevent them from crushing the scintillator. These hard and very dense objects have an effect on electromagnetic showering particularly, as we can see in figures 4.27 and 4.28. The loss of signal due to WLS is added to the loss from spacers and we get a total drop of $\sim 30\%$. And again, the signal resolution goes to over 20%. This effect is noticeable over a region of about 4 cm, and since spacers occur once every 20 cm, they affect about 4% of the total area of the calorimeter.

4.4.2 *Systematic and Statistical Errors in Position Measurement at 5 GeV*

In the previous section, we looked at the statistical errors in position measurements as a function of energy. However, the non-uniformities in the calorimeter lead to

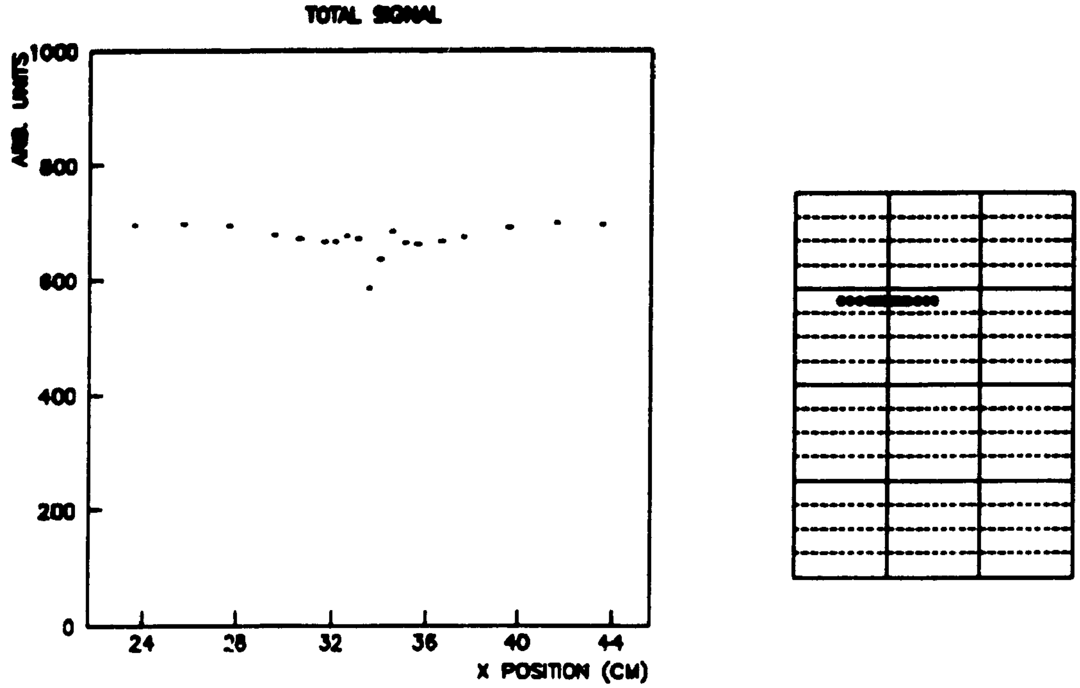

Figure 4.23 : Signal in the calorimeter as a function of the horizontal position of a 5 GeV electron beam. The sketch at the side shows the location of the scan on the face of the prototype. Note the drop in signal at $x = 33.6$ cm — the location of the WLS gap between modules.

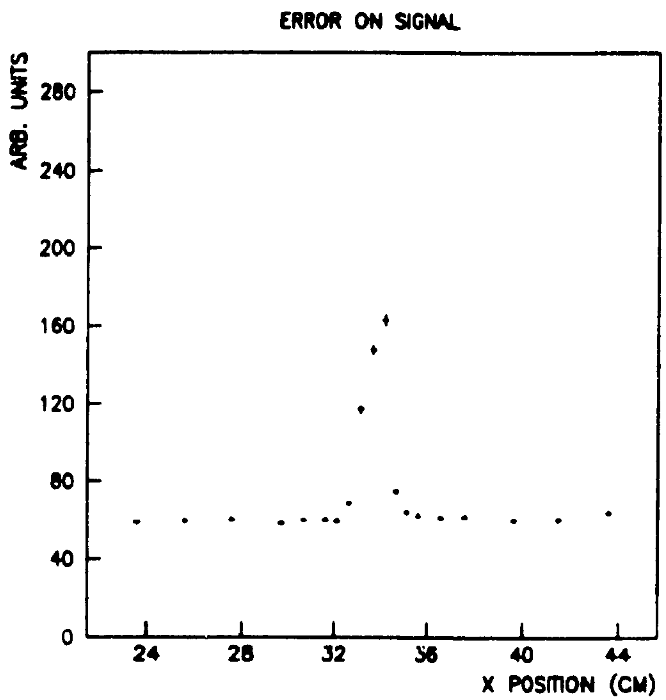

Figure 4.24 : Standard deviation of the signal distribution as a function of the horizontal position of a 5 GeV electron beam. Note the large increase at $x = 33.6$ cm (the gap between modules).

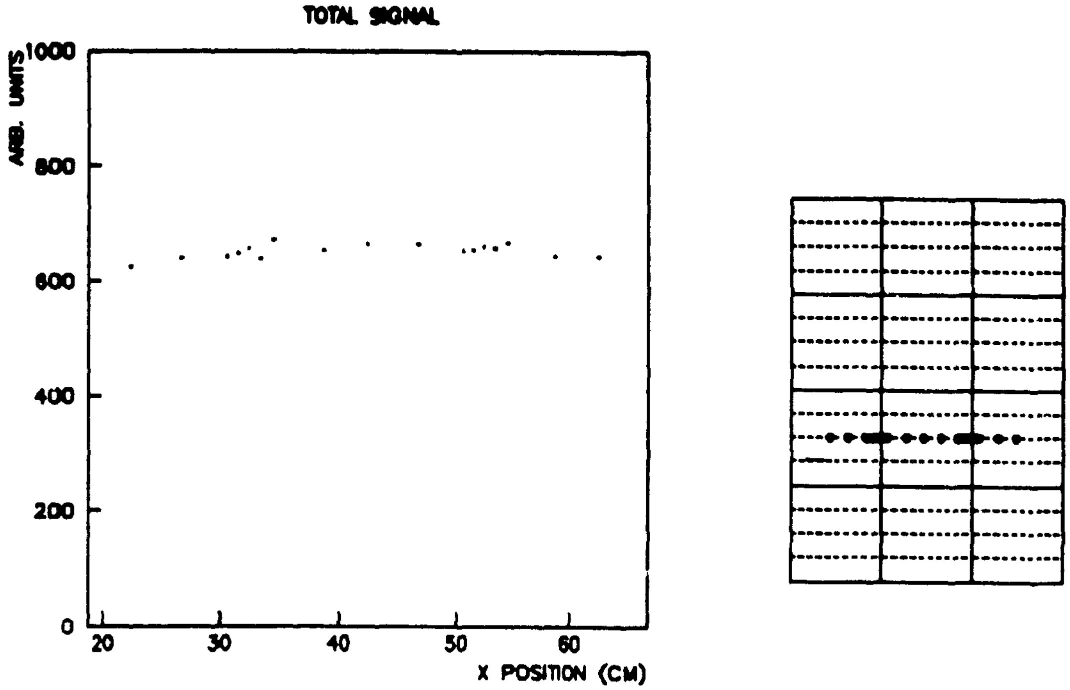

Figure 4.25 : Signal in the calorimeter as a function of the horizontal position of a 5 GeV hadron beam. The sketch at the side shows the location of the scan on the face of the prototype.

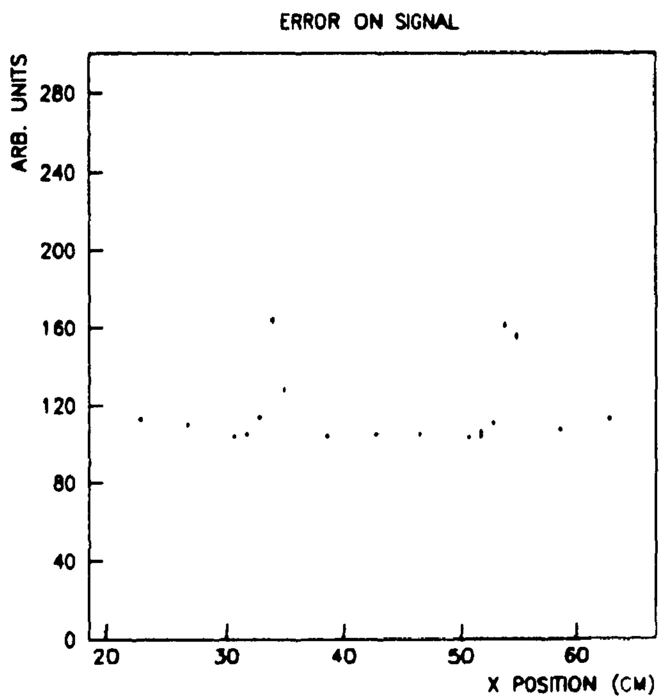

Figure 4.26 : Standard deviation of the signal distribution as a function of the horizontal position of a 5 GeV hadron beam. Note the increases at $x = 33.6$ cm and $x = 53.6$ cm (gaps between modules).

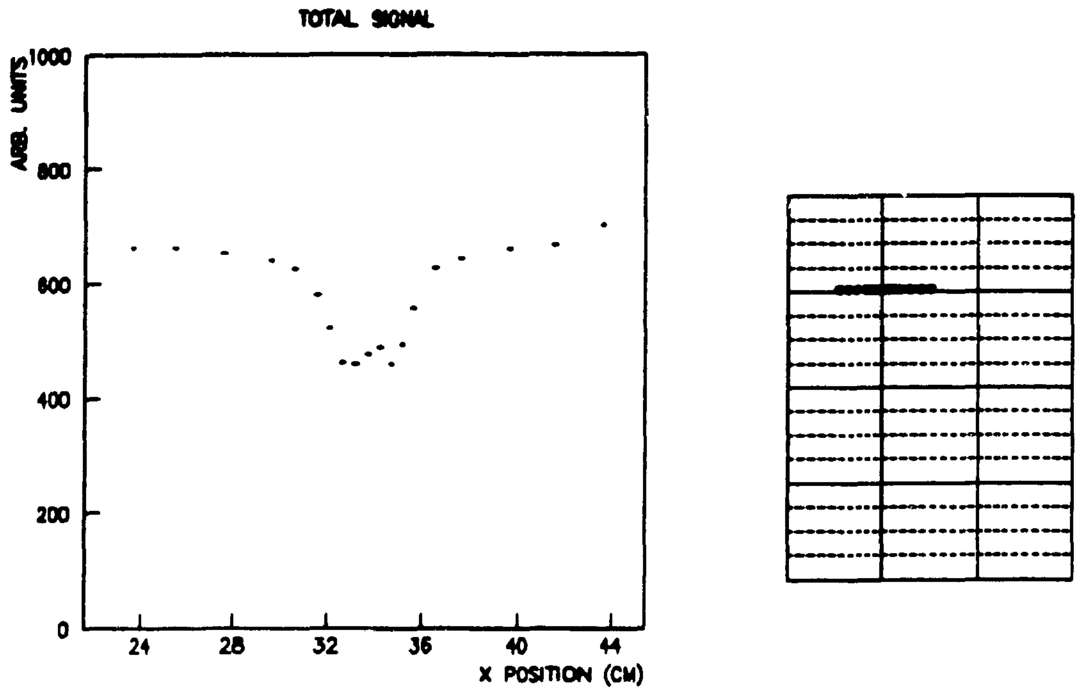

Figure 4.27 : Signal in the calorimeter as a function of the horizontal position of a 5 GeV electron beam scanning over a spacer. The sketch at the side shows the location of the scan on the face of the prototype. Note the loss of sigr.al in the region of x = 33.6 cm — the location of the spacer (and of the WLS gap between modules).

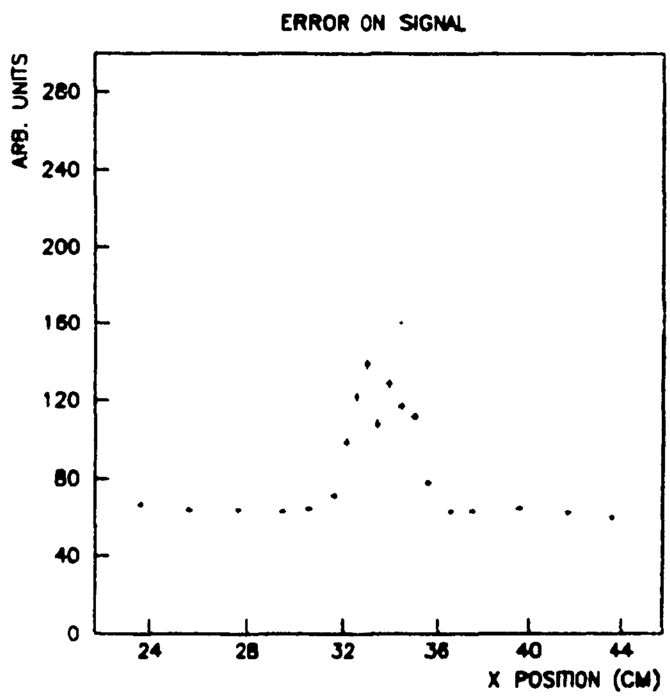

Figure 4.28 : Standard deviation of the signal distribution as a function of the horizontal position of a 5 GeV electron beam. Note the increase in the region of $x = 33.6$ cm (the location of a spacer and of the gap between modules).

variations in these errors for different points on the calorimeter, as well as systematic errors for the approach used here (it should be noted that these "systematic" errors could be eliminated by a more sophisticated analysis). To understand these errors, we look at the position measurements resulting from scans across the face of the calorimeter with data taken at known positions (the same data-sets as used in the last subsection).

Figures 4.29 and 4.30 illustrate the quality of horizontal position measurements as one scans over two modules with an electron beam We see from the first plot an essentially linear measurement, with the largest systematic error occurring near the WLS gap, of a magnitude of about 1 cm. Note that the statistical error given in the second plot decreases to about 1 cm (from just over 2 cm) at this same point because one gets position information from the signal distribution (it is generally spread over two or more sections) as well as from light attenuation in the scintillator. Peculiar things happen in the region of a spacer: in figures 4.31 and 4.32 we see large systematic errors (at most about 5 cm) out to about 4 cm from the WLS gap, as well as strangely behaved statistical errors.

The vertical coordinate measurement is not so linear (see figures 4.33 and 4.34), with systematic errors of order 1 cm occurring as we move from one EMC strip to the next. The resolution also jumps from ~ 0.35 cm to ~ 1.25 cm.

When hadrons are used, the horizontal measurement is quite linear, with small jumps in the resolution as one crosses the WLS gaps (see figures 4.35 and 4.36). Results for the vertical coordinate are given in figures 4.37 and 4.38, and are also quite good. This is because hadron showers are much larger than electron showers and give much more position information through transverse signal distribution. The problem at WLS gaps is reduced because less energy is deposited in the WLS.

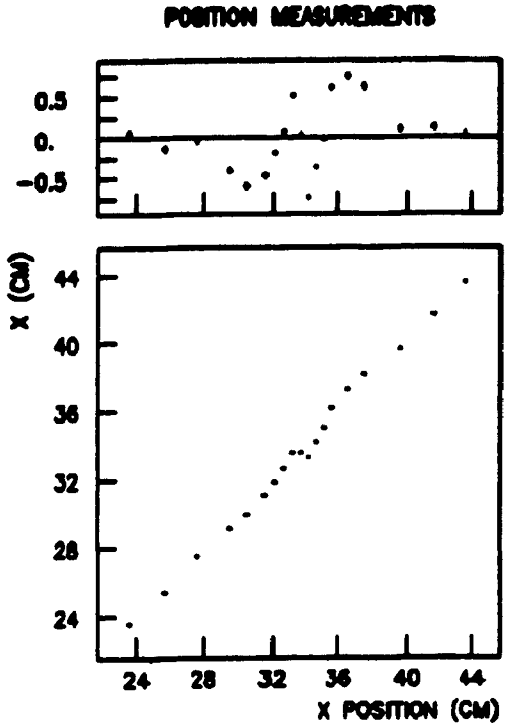

Figure 4.29 : Horizontal position measurement (bottom) and difference from nominal (top) as a function of the actual beam position (for 5 GeV electrons). Note the deviations from linearity near the WLS gap.

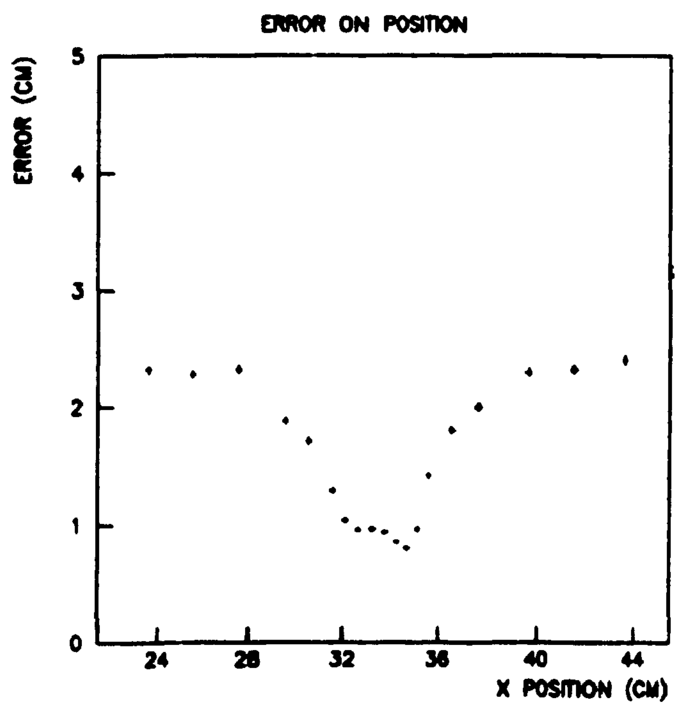

Figure 4.30 : Statistical error in horizontal position measurement as a function of the actual beam position (for 5 GeV electrons). Note the drop near the WLS gap.

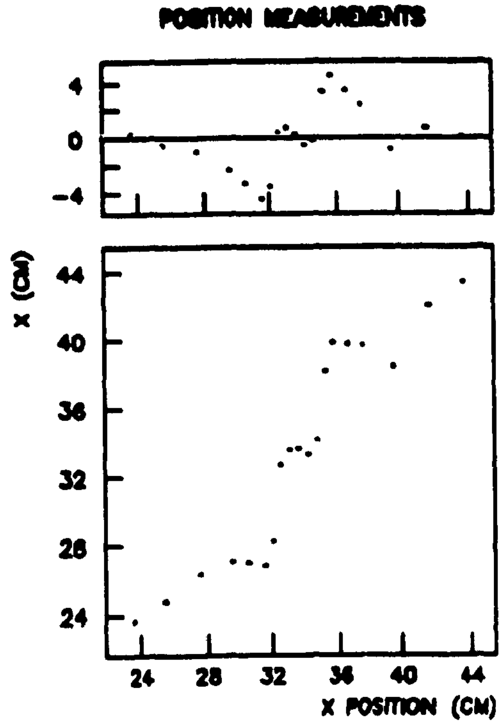

Figure 4.31 : Horizontal position measurement (bottom) and difference from nominal (top) as a function of the actual beam position (for 5 GeV electrons). Note the peculiar behaviour arising from the presence of a spacer.

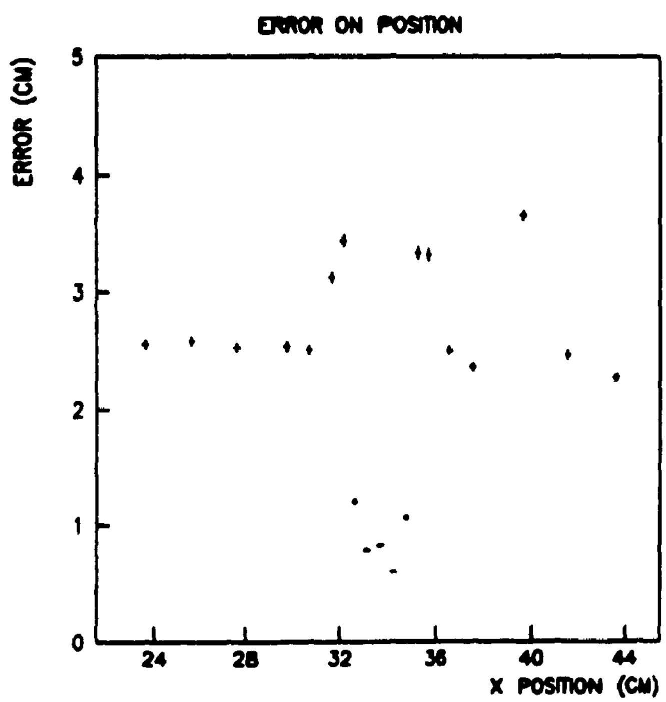

Figure 4.32 : Statistical error in horizontal position measurement as a function of the actual beam position (for 5 GeV electrons). Note the behaviour in the region of the spacer.

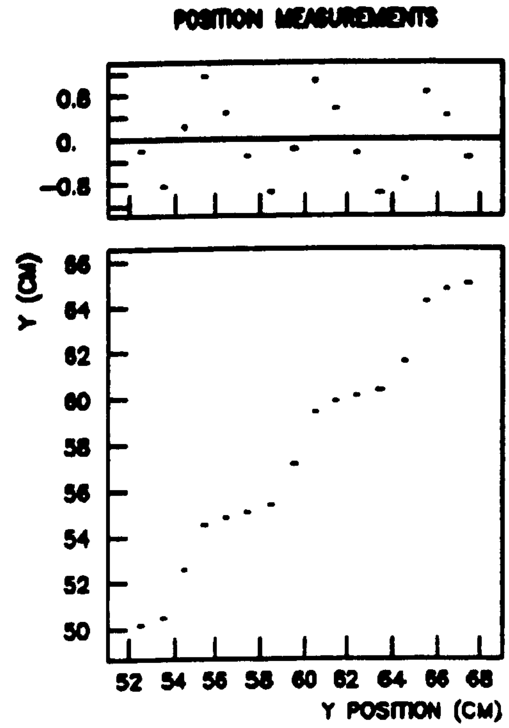

Figure 4.33 : Vertical position measurement (bottom) and difference from nominal (top) as a function of the actual beam position (for 5 GeV electrons).

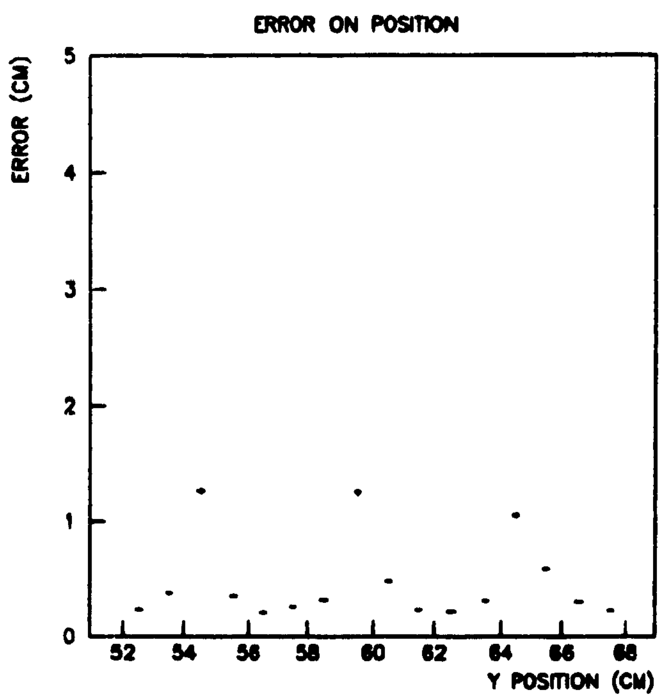

Figure 4.34 : Statistical error in vertical position measurement as a function of the actual beam position (for 5 GeV electrons).

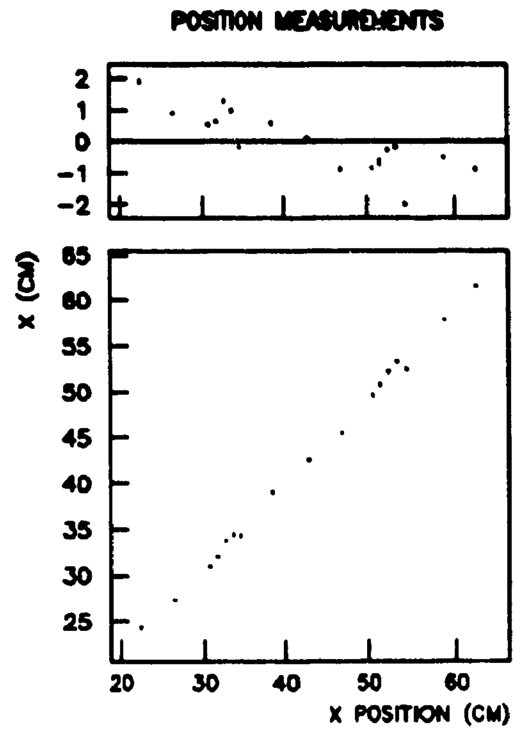

Figure 4.35 : Horizontal position measurement (bottom) and difference from nominal (top) as a function of the actual beam position (for 5 GeV hadrons).

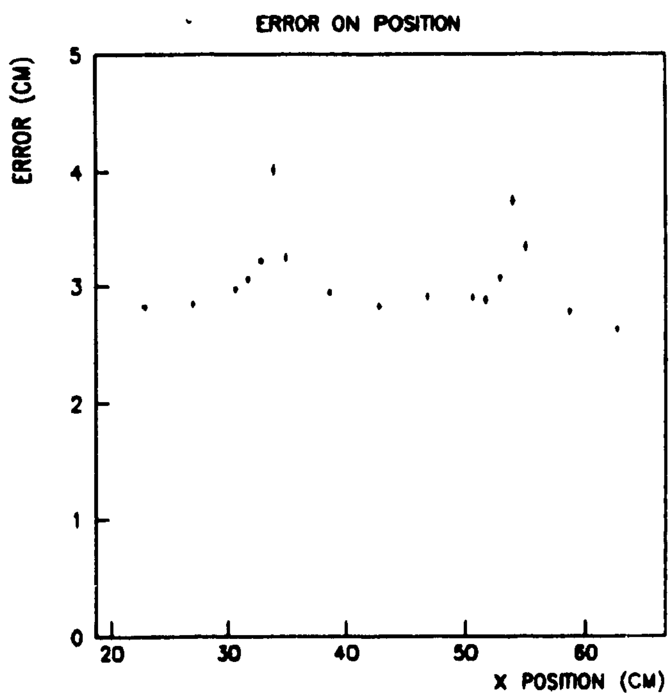

Figure 4.36 : Statistical error in horizontal position measurement as a function of the actual beam position (for 5 GeV hadrons).

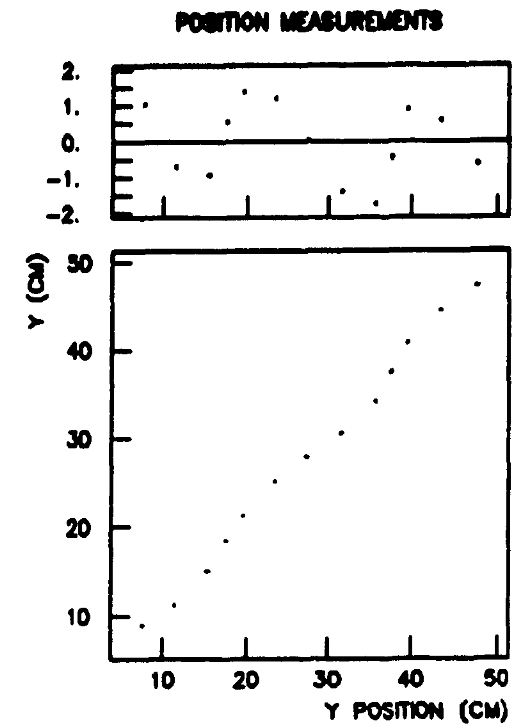

Figure 4.37 : Vertical position measurement (bottom) and difference from nominal (top) as a function of the actual beam position (for 5 GeV hadrons).

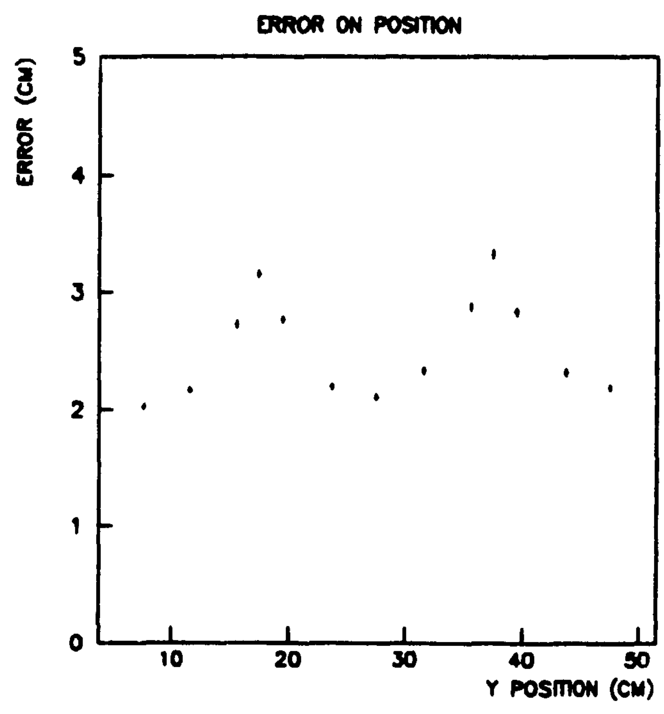

Figure 4.38 : Statistical error in vertical position measurement as a function of the actual beam position (for 5 GeV hadrons).

4.5 Conclusion

We have seen that the principal calorimeter requirements of an electromagnetic energy resolution equal to $15\%/\sqrt{E}$ and a hadron energy resolution equal to $35\%/\sqrt{E}$ have nearly been achieved in the prototype calorimeter through an electromagnetic resolution of $20\%/\sqrt{E}$ and a hadron resolution of $37\%/\sqrt{E}$. It is unlikely that these deviations from the original requirements will have a significant effect on the quality of physics done.

The electron to hadron signal ratio (e/h) has been successfully tuned to be very close to the ideal of 1.0 (1.0024 at 10 GeV) through the appropriate choice of scintillator, DU and stainless steel cladding thicknesses. Of course the real test for both energy resolution and e/h comes in the high-energy tests with particles of energies ranging up to 100 GeV.

Position resolutions of 2 cm and less for single particles have been achieved — this will aid in the combining of calorimeter information with tracking detector information.

The real problems uncovered by these tests are the presence of spacers and the effect of showering in the wavelength-shifter (WLS). The use of tungsten-carbide spacers which have a high atomic number (compare Z for tungsten $= 74$ with Z for iron $= 26$) gives a large reduction in electromagnetic signal and a big increase in error over $\sim 4\%$ of the calorimeter. The WLS, on the other hand, gives an increased signal coming from Cerenkov light. To eliminate this, various solutions, including the use of wavelength selective optical filters to absorb the ultra-violet Cerenkov light and placing lead between modules, are being tested. Slight modifications in design may arise from these problems, but in general the success of the prototype confirms the design for the final calorimeter.

References

[1] Feller, William, *An Introduction to Probability Theory and Its Applications*, Vol. 1, John Wiley & Sons, Inc. (New York), 1957.

[2] Anders, Bernd, Ulf Behrens and Hanno Brückmann, *On the Calculation of the Energy Loss of Muons in Sampling Calorimeters*, December 1987, DESY preprint 87–163.

[3] *Review of Particle Properties*, April 1986 edition.

[4] Hayakawa, S., *Cosmic Ray Physics: Nuclear and Astrophysical Aspects*, Wiley (New York), 1969.

[5] Leroy, C., *Calorimetry in High Energy Physics*, Lecture notes, McGill University, 1987.

[6] Fabjan, C.W., *Calorimetry in High-Energy Physics*, April 1985, CERN preprint EP/85-54.

[7] Amaldi, Ugo, *Fluctuations in Calorimetry Measurements*, Physica Scripta, Vol. 23, pp. 409–424.

Afterword

Although the results of these tests are good, they are not entirely convincing, since the energy range is very limited. Further tests have been carried out at the CERN SPS X5 beam using electrons with energies in the range 10 to 75 GeV and hadrons with energies in the range 10 to 100 GeV. The analysis of this data has been done by Eduardo Ros, confirming the results presented in this thesis. The resolution for both hadrons and electrons goes as $1/\sqrt{E}$, and the e/h ratio goes asymptotically to 1.00 with increasing energy.

A hadron resolution of $\sigma/E = 35\%/\sqrt{E}$ has been achieved by removing events that have excessive energy in HAC2 (those that probably leak out the back of the calorimeter). In the final detector, there will be a backing calorimeter to improve the measurement for such events, so their exclusion from the data is reasonable. An electron resolution of $\sigma/E = 18\%/\sqrt{E}$ was found. Furthermore, problems at the WLS gap were greatly reduced by the use of 2 mm of lead between modules and green light-guides (filtering out the ultra-violet Cerenkov light).